CHARACTERIZATION AND MODELING OF LIGHT ACTIVATED SHAPE MEMORY POLYMER

by

Richard Vincent Beblo

Bachelor of Science in Mechanical Engineering, Bucknell University, 2003

Master of Science in Mechanical Engineering, University of Pittsburgh, 2007

Submitted to the Graduate Faculty of

Swanson School of Engineering in partial fulfillment

of the requirements for the degree of

Doctor of Philosophy in Mechanical Engineering

University of Pittsburgh

2010

UNIVERSITY OF PITTSBURGH

SWANSON SCHOOL OF ENGINEERING

This dissertation was presented

by

Richard V. Beblo

It was defended on

December 11, 2009

and approved by

Dr. William W. Clark, PhD, Associate Professor
Department of Mechanical Engineering and Materials Science

Dr. John P. Leonard, PhD, Assistant Professor
Department of Mechanical Engineering and Materials Science

Dr. William S. Slaughter, PhD, Associate Professor
Department of Mechanical Engineering and Materials Science

Dr. Tat H. Tong, PhD
Cornerstone Research Group, Inc.

Dissertation Director: Dr. Lisa Mauck Weiland, PhD, Assistant Professor
Department of Mechanical Engineering and Materials Science

CHARACTERIZATION AND MODELING OF LIGHT ACTIVATED SHAPE MEMORY POLYMER

Richard V. Beblo, PhD

University of Pittsburgh, 2010

Shape memory polymers have recently become the focus of research for their unique ability to switch between two modulus states, allowing them to both recover from large amounts of strain as well as support complex loads. Part of this research involves engineering new formulas specifically designed for applications where traditional thermally activated SMPs are not ideal by tailoring the activation method used to transition the polymer. One such class of polymers is those that utilize optical energy at specific wavelengths to create and cleave crosslinks. It is the development of this new class of light activated shape memory polymers (LASMP) that is the focus of the presented work.

Experimental methods are newly created for this novel class of active materials. Several candidate LASMP formulas are then subjected to this set of experiments characterizing their mechanical and optical properties. Experimentally observed variations among the formulae include virgin state modulus, percent change in modulus with stimulus, and in some instances inelastic response.

To expedite the development of LASMP, a first principles multi-scale model based on the polymer's molecular structure is presented and used to predict the stress response of the candidate formulas. Rotational isomeric state (RIS) theory is used to build a molecular model of a phantom polymer chain. Assessment of the resulting conformation is then made via the Johnson family of statistical distributions and Boltzmann statistical thermodynamics. The ability

of the presented model to predict material properties based on the molecular structure of the polymer reduces the time and resources required to test new candidate formulas of LASMP as well as aiding in the ability to tailor the polymer to specific application requirements.

While the first principles model works well to identify promising formulas, it lacks precision. The stress contribution from the constraints on the polymer chain's junctions and neighboring chain entanglements is then added to that of the phantom network allowing Young's modulus to be calculated from the predicted stress response of the polymer. Simple extension, equi-biaxial, and shear strain states are modeled and associated predicted material properties presented. The added precision of this phenomenological extension will aid device design.

TABLE OF CONTENTS

LIST OF TABLES

LIST OF FIGURES

PREFACE

There are many people who have helped and influenced me throughout my life and career and to whom I am greatly indebted. First, my parents, who have challenged and supported me in all I have done. I have had the good fortune of inheriting both their work ethic and morals which comprise the foundation for my achievements thus far in life. My wife, Diana, who has also been very supportive and accommodating in my ambitions, both in life and academia, and for always being there to turn to. Dr. Lisa Weiland, my academic advisor, who's strong work ethic, honest advice, and continuous jovial attitude simultaneously inspired greatness in my work while providing a great learning environment; and for believing in me and giving me the opportunity to explore the possibilities of my potential. All of my friends and family from various stages and places in my life for their support and encouragement. And last but not least my thesis committee and all of my teachers, professors, and colleagues throughout my career at Reynolds High School, Bucknell University, the University of Melbourne, the University of Pittsburgh, HRL Laboratories, and Cornerstone Research Group, Inc. for always seeing my potential and supporting and guiding me in my quest to reach it.

I am indebted to all of you in ways that can never be repaid. May the worst days of your future be better than the best days of your past and good luck in all you do.

1.0 INTRODUCTION

1.1 SHAPE MEMORY POLYMERS – CURRENT STATE OF THE ART

1.1.1 Shape Memory Polymer Introduction

Shape memory polymers (SMP) were first introduced in 1984 in Japan [1] and have since become the focus of many ambitious research initiatives. They are divided into three major types based on the stimulus used to bring about a change or desired response of the polymer. The most common is the thermally or heat activated type [2-27], followed by the electrically activated type [28-30], and finally the light activated type [31-42]. Each type is further divided into two categories based on material response and then again into groups with respect to the chemical makeup of the polymer. The first main category of each type of SMP is comprised of those polymers that start in an initial stress free state, exert a force on their surroundings when stimulated, and then return to their initial state when the stimulus is removed, without the use of external forces. Such polymers are typically presented as actuators or artificial muscle [28-30,43]. Heat activated polymers belonging to this category include those based on siloxanes, polyethers, and Smectic-C [2-27]. Electrically activated polymers of the "shape change" group include Nafion®, Flemion®, and PVDF. Light activated shape memory polymers of this group are typically constructed of triphenylmethane or azobenzene [43-45,28-30]. The second main

category is comprised of those polymers that, rather than switching between two strain states based on a stimulus, switch between two moduli when activated and require external forces to deviate from their initial state. This category of shape memory polymer is most generally presented as a candidate material for morphing or reconfigurable structures. It is this second category that is of interest here. To the author's knowledge, there does not exist electrically activated SMPs currently available belonging to this second category. Heat activated SMPs and light activated SMPs are typically variations of styrene, urethane, or epoxy [46,47], and coumarin, cinnamates, or stilbenes respectively [31-42,47,48]. Since polymers in this second category are the focus of this thesis, electrically activated polymers will be given no further treatment. The two main categories of each type of SMP are then further divided into groups based on their chemical makeup. Some of these groups are presented below in Figure 1.1.1-1.

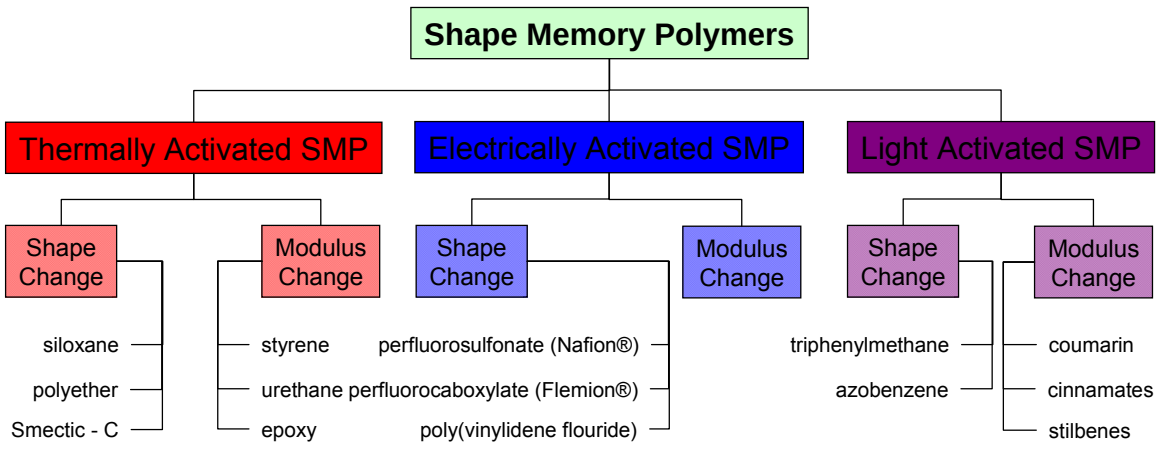

Figure 1.1.1-1: Shape memory polymer categorization chart

Modulus changing SMPs are the group that has been proposed for adaptive structures, are the focus of the presented work, and will be the only group of polymer discussed further. As such, all subsequent language referring to SMPs will refer to the modulus changing group unless

otherwise noted. SMPs have the ability to switch between low and high moduli while retaining a memorized shape, making them desirable for designs requiring adaptable structural components. They do this by switching between a rubbery or elastic state and a glassy or stiff state using a stimulus. Pictured below in Figure 1.1.1-2 is a typical graph of the modulus dependence on thermal stimulus of a heat activated SMP. Below the glass transition temperature, T_g, the polymer is in the glassy state and has a relatively high modulus and is thus capable of supporting load. Above T_g, the polymer is in the elastic state and behaves similar to an elastomer, capable of sustaining extremely high strains but unable to support large loads.

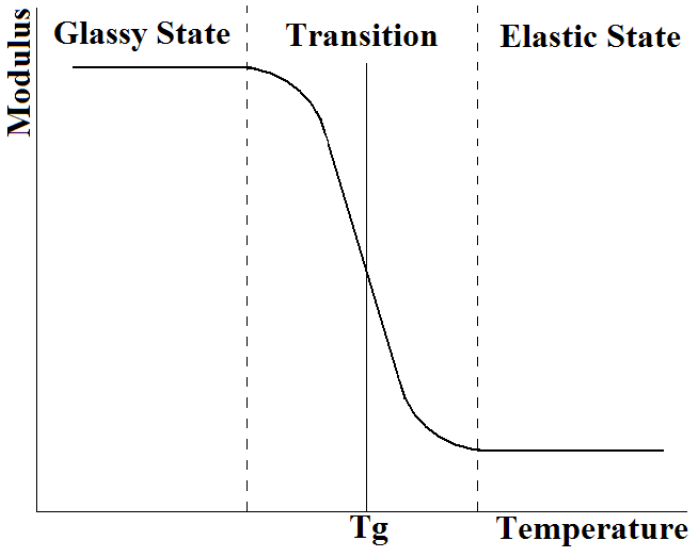

Figure 1.1.1-2: Representative SMP temperature dependence

A typical SMP cycle consists of a sample beginning at a temperature below T_g, the temperature is then increased above T_g, the sample deformed into a new shape, then cooled below T_g where the new shape is fixed. Stored energy in the polymer by way of strain during deformation provides a restorative force when again heated above T_g in the elastic state, allowing the polymer to return to its memorized shape given the absence of external forces. This shape

memory cycle is shown below in Figure 1.1.1-3. The amount of strain that the sample can sustain without permanent damage is considered the strain limit of the polymer, which differs between each formulation. Shape fixity is related to the amount of relaxation that the polymer undergoes during cooling after being strained while strain recovery refers to the amount of induced strain recovered when no forces are acting on the polymer above T_g. Other typical characteristics of interest is the amount of energy required to transition, which for thermally activated SMPs is presented as the heat of crystallization, as well as more common material characteristics such as density, molecular weight, heat capacity, electrical resistance, etc. The unique combination of the above characteristics of SMP make it an ideal candidate for particular applications. While the most common thermally activated SMP is well suited for many uses, certain applications require a unique set of material qualities. Applications such as morphing aircraft and satellite systems where heat signatures, operational temperature ranges, and on board power limitations are not ideally suited for a thermally activated material; a new, different type of SMP is required, such as light activated SMP (LASMP). While development of LASMP is clearly desirable, the bulk of research to date has focused on thermally activated SMP. It is therefore prudent to become versed in thermal SMP as a means to efficiently direct LASMP evolution. The following literature review therefore begins with an in-depth treatment of the state of the art in thermal SMP and is followed by review of current research efforts for LASMP.

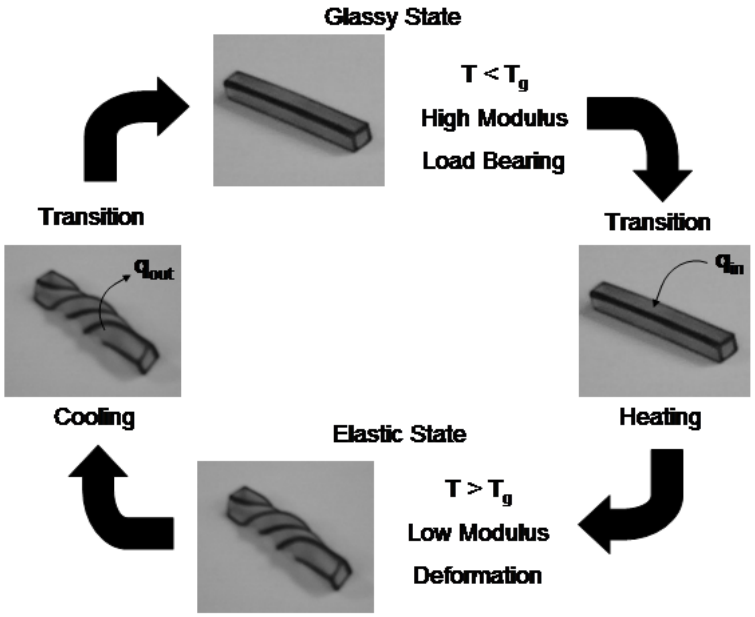

Figure 1.1.1-3: Heat activated shape memory polymer cycle

1.1.2 Thermally Activated SMP

The first realized shape memory polymers were based on polynorborene, trans-isopolyprene, and styrene-butadiene copolymer systems. Due to their relatively complicated synthesis and poor mechanical properties, focus quickly switched to segmented polyurethane thermoplastic SMPs. These multiblock copolymers consist of alternating sequences of hard and soft segments. The distribution of soft segments, typically 1000 to 10,000 in molecular weight, and hard segments, typically built from diisocyanates and extenders, give shape memory polymer its unique characteristics. The hard segments accumulate and form permanent physical crosslink points by polar interactions, hydrogen bonding, and or crystallization while the soft segments form the reversible phase and provide the molecular motion required for deformation and the restorative aspects of SMPs. Above the glass transition temperature, T_g, of the polymer; the soft segments are relatively elastic and allow the polymer to accommodate large deformations as high as 400%

strain. Below T_g, the soft segments become hard and are locked in place, fixing the current shape of the polymer. The glass transition temperature of such polyurethane block copolymer systems can easily be tailored as much as plus or minus 50 degrees Celsius from room temperature by altering the ratio of hard and soft segments and can be processed through extrusion, injection, blow molding, and solution coating, making them extremely versatile [17,18].

1.1.2.1 Constitutive Modeling of Thermally Activated SMP

Currently there are two basic methodologies for creating constitutive models for describing heat activated shape memory polymers. The first is a piece wise method that breaks up the response of the polymer into four distinct sections, see Figure 1.1.1-2. Below the transition temperature, small strain approximations and constant temperature, hence constant modulus, are utilized to create visco-elastic models. During transition when heat is applied, time dependent temperature equations are derived describing the modulus of the polymer, which is assumed isotropic. During straining above the transition temperature, the modulus is again assumed constant and the model takes the form of purely elastic equations, such as those used to describe elastomers. Finally, during transition while cooling, the constitutive equations are similar to those during heating but differ only in the modeling of the chemical structure of the polymer. While this method results in accurate 3-D predictions of material response within each segment, lifetime simulations become more complicated with four separate equations. Another limitation of this methodology is that some polymers are capable of large strains below the transition temperature, which cannot be modeled by this method having assumed small strains in that region of the response.

The second methodology, in an attempt to derive a single thermo-visco-plastic constitutive equation for shape memory polymers over their entire operating range, assumes the polymer to be isotropic in all conditions. Since other assumptions such as constant temperature or small strains are not required, such 1-D models have proven useful for several applications. The resulting equation of this method accurately predicts the material's behavior under any environment in the direction chosen making lifetime simulations much simpler. While this method is valuable for applications such as simple unidirectional sensors and actuators, designs requiring complex loading cannot use this approach due to the polymer's anisotropic nature at large strains.

1.1.2.1.1 Review of Recent Constitutive Models

In January of 2002, Häusler et al. introduced a model predicting the transverse isotropy effect exhibited by many materials at large deformations. In the elastic region, the elasticity law, kinetic hardening rule, and yield function are considered to be transversely isotropic as well as the evolving plastic deformation constitutive properties. Assuming the virgin material to be isotropic, the yield function, Equation 1.1.2.1.1-1, kinematic hardening rule, Equation 1.1.2.1.1-2, elasticity law, Equation 1.1.2.1.1-3, and plastic spins, Equation 1.1.2.1.1-4, comprise the proposed 3-D visco-plastic model [49].

$$f = \left\{ \begin{array}{c} \nu_1 tr\left(\underline{\sigma}^2\right) + \nu_2 tr\left(\underline{\sigma}_s \mathbf{M}^{(y)} \underline{\sigma}_y\right) + \nu_3 \left[tr\left(\mathbf{M}^{(y)} \underline{\sigma}_s\right)\right]^2 + \\ \nu_4 tr\left(\underline{\sigma}_A^2\right) + \nu_5 tr\left(\underline{\sigma}_A \mathbf{M}^{(y)} \underline{\sigma}_A\right) + \nu_6 tr\left(\underline{\sigma}_A \mathbf{M}^{(y)} \underline{\sigma}_s\right) \end{array} \right\}^{1/2} - k_0 \qquad (1.1.2.1.1\text{-}1)$$

$$\Psi_p = \overline{\overline{\Psi}}_p\left(\hat{\mathbf{Y}}, \Delta\right) = \hat{\Psi}_p\left(\hat{\mathbf{Y}}, \hat{\mathbf{M}}^{(k)}\right) = \frac{1}{2\varsigma_R} \hat{\mathbf{Y}} \bullet \hat{\mathbf{C}}^{(k)}\left[\hat{\mathbf{Y}}\right] \qquad (1.1.2.1.1\text{-}2)$$

$$\mathbf{S} = \hat{\mathbf{C}}^{(e)}[\mathbf{A}_e] \tag{1.1.2.1.1-3}$$

$$\begin{aligned}\overset{\Delta}{\mathbf{M}} = \mathbf{DM} + \mathbf{MD} - \left\{\mathbf{W} - \left(\mathbf{V}_e^{-1}\mathbf{L}\mathbf{V}_e\right)_A - \left(\dot{\mathbf{V}}_e\,\mathbf{V}_e^{-1}\right)_A + \Omega\right\}\mathbf{M} + \\ \mathbf{M}\left\{\mathbf{W} - \left(\mathbf{V}_e^{-1}\mathbf{L}\mathbf{V}_e\right)_A - \left(\dot{\mathbf{V}}_e\,\mathbf{V}_e^{-1}\right)_A + \Omega\right\}\end{aligned} \tag{1.1.2.1.1-4}$$

Where v_1-v_6 are material parameters, σ is the Eulerian counterpart of the plastic spin, $\boldsymbol{M}$ is a structural tensor, Δ is the spin associated with the kinematic hardening rule, $\boldsymbol{C}$ is the Right Couchy-Green tensor, $\boldsymbol{S}$ is stress, $\boldsymbol{A}_e$ is the Almansi strain tensor, $\boldsymbol{D}$ is the deformation rate tensor, $\boldsymbol{W}$ is work, $\boldsymbol{V}_e$ is the Left Cauchy-Green tensor, $\boldsymbol{L}$ is the velocity gradient, and Ω is the associated plastic spin with respect to the intermediate configuration. The resulting set of constitutive equations includes 26 material constants, many of which admittedly have unknown real relations. With arbitrarily chosen values, the qualitative response of the model is indicative of many materials. By varying the unknown quantities, the model accurately predicts the transverse isotropy found experimentally at large deformations [49]. The pertinent information provided by the proposed model is the method in which the equations are derived. By assuming transverse isotropy initially, the derivations of the equations are simplified with little loss of generality. Since shape memory polymers can be considered orthotropic at large strains, starting with equations tailored to model such behavior is intuitive [49]. However, the form of the initial yield, kinematic hardening, elasticity law, and spin functions are typical for those of metals, making direct applications to shape memory polymers somewhat impractical, although possible

through manipulation of the several parameters. The model also does not take into account thermal effects, rendering the model incapable of predictions in the transition region.

In 2001, Tobushi et al. developed a one dimensional model for shape memory polymers. The proposed model, comprised of Equations 1.1.2.1.1-5 through 1.1.2.1.1-7, is a nonlinear extension of a previous linear model. The linear model was based on linear visco-elastic theory with the addition of a slip element accounting for internal friction, allowing large strain calculations [50].

$$\dot{\varepsilon} = \frac{\dot{\sigma}}{E} + m\left(\frac{\sigma - \sigma_y}{k}\right)^{m-1}\frac{\dot{\sigma}}{k} + \frac{\sigma}{\mu} + \frac{1}{b}\left(\frac{\sigma}{\sigma_c} - 1\right)^{n} - \frac{\varepsilon - \varepsilon_s}{\lambda} + \alpha\dot{T} \qquad (1.1.2.1.1\text{-}5)$$

$$\varepsilon_s = S\left(\varepsilon_c + \varepsilon_p\right) \qquad (1.1.2.1.1\text{-}6)$$

$$E = E_g \exp\left[a\left(\frac{T_g}{T} - 1\right)\right] \qquad (1.1.2.1.1\text{-}7)$$

Where $\boldsymbol{\varepsilon}$ is strain, σ is stress, E is Young's modulus, m and k are material parameters, μ is the modulus of viscosity, λ is the retardation time, α is the coefficient of thermal expansion, T is temperature, S is a proportional coefficient, T_g is the glass transition temperature of the polymer, E_g is the value of E at $T = T_g$, $\boldsymbol{\varepsilon}_s$ is irrecoverable strain, $\boldsymbol{\varepsilon}_c$ is creep strain, and $\boldsymbol{\varepsilon}_p$ is plastic strain. The non-linearities arise from the addition of the terms containing m, k, and b in Equation 1.1.2.1.1-5. While this model results in accurate 1-D predictions, the lack of transverse directions greatly limits its uses. Because the model is incapable of predicting transverse

anisotropies, it is only useful in applications such as 1-D actuators or sensors. The major strength however, is that it provides a single constitutive equation relating temperature, strain, strain rate, and stress of the material providing easy calculations and lifetime simulations. Such simulations resulted in the ability to correctly predict irrecoverable strain, Equation 1.1.2.1.1-6, over many cycles in different stress states [50].

In 2006, Diani, Liu, and Gall proposed a thermo-visco-elastic constitutive model for shape memory polymers. Their model is based on the assumption that changes in the stress state of the polymer above T_g are due primarily to changes in entropy while changes below T_g are derived by changes in the internal energy of the polymer. They assumed that the polymer is of constant volume and at constant temperature while in its rubbery state above the glass transition temperature and that chain motion can be neglected in the polymer's glassy state. Diani et al. also considered all strains to be elastic, assuming that no plasticity through chain slippage occurs. These assumptions lead to the following Zener model pictured in Figure 1.1.2.1.1-1 [51].

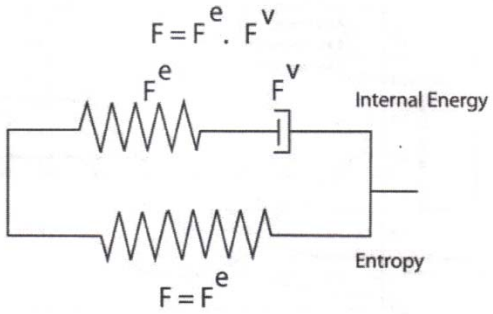

Figure 1.1.2.1.1-1: Model rheological scheme

Taking Young's modulus to be linearly dependent on temperature and the polymer to be an isotropic heavily cross-linked epoxy network, the thermo-visco-elastic model is described by the following equation [51]:

$$\frac{1}{2}\left(\mathbf{S}-2\frac{\partial T\eta}{\partial \mathbf{C}}-2\mathbf{F}^{v}\frac{\partial U}{\partial \mathbf{C}}\mathbf{F}^{v-T}\right):\mathbf{C}+2\frac{\partial U}{\partial \mathbf{C}^{e}}:\left(C^{e}\mathbf{L}^{v}\right)-\frac{\mathbf{q}_{0}}{T}grad\left(T\right)\geq 0 \qquad (1.1.2.1.1\text{-}8)$$

which can be decomposed into the following:

Stress – Strain Relation: $$\mathbf{S}=2\frac{\partial T\eta}{\partial \mathbf{C}}+2\mathbf{F}^{v}\frac{\partial U}{\partial \mathbf{C}}\mathbf{F}^{v-T} \qquad (1.1.2.1.1\text{-}9)$$

Mechanical Dissipation: $$2\frac{\partial U}{\partial \mathbf{C}^{e}}:\left(\mathbf{C}^{e}\mathbf{L}^{v}\right)\geq 0 \qquad (1.1.2.1.1\text{-}10)$$

Thermal Dissipation: $$-\frac{\mathbf{q}_{0}}{T}grad\left(T\right)\geq 0 \qquad (1.1.2.1.1\text{-}11)$$

Where $\boldsymbol{S}$ is the second Piola-Kirchoff stress tensor, T is temperature, $\boldsymbol{C}$ is the right Cauchy-Green tensor, $\boldsymbol{F}^{v}$ is the viscous part of the deformation gradient, U is the internal energy of the polymer and a function of F_v, $\boldsymbol{L}^{v}$ is the velocity gradient corresponding to F_v, q_o is the outward heat flux from the Clausius-Duhem inequality, and η is entropy. The model predicts the thermomechanical response of the polymer well, having a difference of only 0.5% between the experimental and calculated permanent strain after unloading following a thermal cycle. However the authors admit that more accurate evolution equations would improve the accuracy of the model [51]. While the model is useful for several applications, the initial assumptions limit the model's ability to accurately estimate the stress strain behavior of shape memory polymers under certain conditions. The incorrect assumption that chain motion can be neglected below T_g significantly effects the predictions of the model. Including polymer chain slippage would result in higher internal energies of the polymer below T_g, producing higher stress state

predictions. Since the model is elastic, it cannot predict the plastic strain coupled with chain slippage. The model also assumes the polymer to be isotropic resulting in Equation 1.1.2.1.1-10 becoming [51]:

$$\left(\mathbf{C}^e \bullet \frac{\partial U}{\partial \mathbf{C}^e}\right) : \mathbf{D}^v \geq 0 \qquad (1.1.2.1.1\text{-}12)$$

In contrast, it has been shown that at high strains, the material properties of shape memory polymers become anisotropic differing by as much as 63% [52], limiting the application of the proposed model.

Also in 2006, Barot and Rao proposed dividing the material response into four distinct segments; being the glassy state, melting, rubbery state, and crystallization. The glassy state is modeled by traditional elastic methods assuming small strains and constant temperature. The rubbery state is modeled as a hyperelastic incompressible material described by Equation 1.1.2.1.1-13, based on changes in entropy [53].

$$\mathbf{T} = -p\mathbf{I} + 2\rho\mathbf{F}_{K_o}\frac{\partial \psi_a}{\partial \mathbf{C}_{K_o}}\mathbf{F}_{K_o}^T \qquad (1.1.2.1.1\text{-}13)$$

Where $\boldsymbol{T}$ is the Cauchy stress, p is the Lagrangian multiplier, $\boldsymbol{F}_{Ko}$ is the deformation gradient, ψ is the Helmholtz potential, and $\boldsymbol{C}_{Ko}$ is the Right Cauchy stress tensor. The crystallization phase, which is the focus of the work, is modeled as a constrained mixture. The proposed model assumes the crystals are formed under a stress free state which deviates from practical application. It has been shown that if under stress, the forming crystals will have an orientation

resulting in anisotropic bulk material properties. To better model this effect, evolution equations for K_a and K_c would have to be prescribed. To account for the anisotropies of the polymer, the Helmholtz potential function is of the form of an anisotropic solid. To accommodate lifetime simulations, the stored energy between two phases of the polymer is considered to be additive. Finally, assuming the polymer to be orthotropic, the resulting non-dimensional form of the constitutive equation is given by [53]:

$$\mathbf{T} = -p\mathbf{I} + (1-\alpha(t))\mu_a \mathbf{B}_{K_a} + \int_{t_1}^{t_2} \mu_1 \mathbf{B}_{K_{c(\tau)}} \frac{\partial \alpha}{\partial \tau} \partial\tau + \int_{t_1}^{t_2} \left[\mathbf{F}_{K_{c(\tau)}} \left\{ \mu_2 (J_1 - 1) \mathbf{n}_{K_{c(\tau)}} \otimes \mathbf{n}_{K_{c(\tau)}} + \mu_3 (K_1 - 1) \mathbf{m}_{K_{c(\tau)}} \otimes \mathbf{m}_{K_{c(\tau)}} \right\} \right] \frac{\partial \alpha}{\partial \tau} \partial\tau \quad \text{(1.1.2.1.1-14)}$$

Where $\boldsymbol{T}$ is the Cauchy stress, p is the Lagrange multiplier, $\boldsymbol{I}$ is the identity, μ_a, μ_1, μ_2, and μ_3 are non-dimensional material moduli, $\boldsymbol{B}_{Ka}$ is the Left Cauchy stress tensor, τ is the time of crystallization, $\boldsymbol{n}$ and $\boldsymbol{m}$ are unit vectors in the direction of orthotropy, J_1 and K_1 are invariants, and $\boldsymbol{F}_{Kc}$ is a mapping between the time of formation τ and the current time t. To assess the validity of the model, the equations are simplified to simulate uni-axial strain and circular shear conditions. The material parameter constants are heuristically determined to match published experimental data, resulting in very little error between the predicted and experimental stress states [53]. While the proposed constitutive relations fit experimental data well, there are still a few inherent discrepancies in their derivations. The model does not take into account any rate effects associated with the polymer, ignoring any visco-elastic or visco-plastic effects. In addition, while it is stated in the derivation that prediction of anisotropic material properties is accounted for, the evaluation of the validity of the model does not include this. Further, the

model for the polymer below the glass transition temperature assumes small strain, thus the model is incapable of predicting the experimentally known plastic strain region of the response [52]. Finally, the model being divided into separate segments makes lifetime simulations more complicated than is desirable. Because of this, the effect seen experimentally of the polymer's ability to deform plastically being a function of the current strain state with respect to a virgin material is difficult to simulate.

1.1.2.1.2 Summary of Recent Constitutive Models

Each of the proposed constitutive relations has been derived for a particular purpose and fits the available experimental data well. Each, however, also has inherent flaws that limit the potential uses of the model.

Rate Effects: While the models presented by Tobushi and Diani contain rate effects, seen in Equations 1.1.2.1.1-5 and 1.1.2.1.1-8, Häusler's and Barot's models do not. Without rate effects, environments involving high frequency cyclic loading or vibrations, such as near electric motors or jet engines cannot accurately be modeled and thus should be avoided. While assuming small strain rates is not an unreasonable assumption, it does limit the range of applications the model can be applied. Isothermal assumptions also create error in the models presented by Häusler and Barot, leaving room for improvement.

Thermal Effects: With the goal of developing a single constitutive equation that is valid for all environments and stress states, the inclusion of thermal effects must be considered. There are a few ways to include temperature in the model, for example Tobushi introduces a phenomenological fit for the evolution of material parameters with respect to temperature, such as Equation 1.1.2.1.1-7. Diani's model embeds the effects of temperature in a thermal dissipation term attached at the end of the constitutive equation, Equations 1.1.2.1.1-8 and

1.1.2.1.1-11). Finally, Barot's approach of dividing the response into segments simplifies the overall set of equations by allowing the temperature to be assumed constant above and below Tg. During melting and crystallization, the thermal effects are imbedded in the internal variables of μ_a, μ_1, μ_2, and μ_3.

Plasticity: Traditionally, plasticity has been avoided when modeling shape memory polymers. The material's ability to recover nearly 100% of the applied strain through heating with the rubbery state of the polymer capable of strains over 200%, has caused many engineers to assume that an application requiring large strains would be designed such that those strains would be applied during the rubbery state of the polymer, eliminating the need to account for plastic deformation since the polymer is elastically linear to failure, such is the model proposed by Diani. New research however suggests that plasticity is an issue with shape memory polymers and should be included in modeling [52]. Tobushi accounted for large plastic strains by the addition of a slip element in the model while Barot separated the response into segments, deriving the pertinent equations from traditional plasticity theory.

1.1.2.2 Experimental Characterization of Thermally Activated SMP

Over the past decades as SMP has become increasingly utilized, the body of research, especially mechanical characterization, has dramatically increased. Although numerically not directly applicable to light activated shape memory polymers; material response results of several heat activated SMPs are indicative of those expected to be found with LASMPs, particularly when the backbone monomers are similar as is the case with the polystyrene based SMP Veriflex® and the current presented study of LASMP, also styrene based.

1.1.2.2.1 Thermally Activated Styrene SMPs

Published in 2007, Gross and Weiland conducted 3 point bend tests on Veriflex® finding the flexural moduli to be 700 and 6.48 MPa and flexural strengths 38 and 0.8 MPa in the glassy and elastic states respectively. Also reported were the yield stresses of the polymer at 20 and 0.61 MPa and creep moduli of 710±110 MPa and 440±240 Pa in the cold and hot states respectively. Their research provided the remaining material parameters needed to complete a 1-D constitutive model for Veriflex®, such as that presented in Equations 1.1.2.1.1-5 through 7, furthering the polymer's incorporation into current design initiatives [11,54].

Polystyrene based SMPs have also been the focus of orientation studies by Aida et al. [21] and Beblo and Weiland [52,55]; with expected results as compared with other polymers [9]. Aida utilized SAXS methods to prove that the polymer chains become oriented under strain, thus resulting in an anisotropic material. Beblo and Weiland conducted tensile tests in the axial and transverse directions with respect to differing amounts of pre-applied strain. The study concluded that for Veriflex®, the Young's modulus of the material decreases by as much as 86% in the transverse direction at 70% strain in the axial direction, decreasing from an isotropic value of 1140 to 160 MPa when below the transition temperature in the glassy state. The yield stress was also seen to decrease by 30% in similar conditions. Another significant finding was that the failure strain of the polymer in the glassy state is dramatically increased when the polymer is appropriately strained in the elastic state prior to testing. Samples which typically failed between 5 and 31% strain in their isotropic state, were capable of sustaining additional strains up to 82% in the glassy state when conditioned with 40% strain prior to testing in the elastic state. This increase in toughness could be used as a preventative measure in certain applications where undesired strain is less catastrophic than crack propagation. It is proposed that these changes in

material properties under strain result from the partial alignment of the polymer chains under high strain [52,55].

Tandon et al. have also recently published work quantifying Veriflex's® change in material properties when exposed to lubricating oil, water, and UV light. The study found that surface microcracks formed when submersed in oil for as little as 8 hours, presumably leading to premature failure. The polymer was also seen to turn milky white when exposed to water for extended periods of time, 4 days, leading to a slight decrease in strength, 1.4 to 1.36 GPa. All adverse effects due to water absorption, however, were found to be reversible with heating and evaporation. The adverse effects of UV light, however, are irreversible and resulted in the polymer becoming extremely brittle. Tandon et al. also report the sensitivity of the polymer to viscous effects during testing, stating a change in the measured Young's modulus with differing strain rates [56].

1.1.2.2.2 Thermally Activated Polyurethane SMPs

Less directly applicable to the LASMP of this thesis than tests conducted on polystyrene based SMPs, but valuable in predicting material trends, are those studies performed on other heat activated SMPs, such as the more common polyurethane based formulas. Several studies have been performed measuring the glass transition temperature of different formulas [13,20,22,24,57] and the change in modulus with respect to temperature [13,20,22]. The elastic limit of the material, typically around 10% strain, as well as the observed stress plateau between 10% and 60% strain have been observed in several polyurethane polymers [13,15] as well as polystyrene polymers [52,55]. Strain recovery and shape fixity in polyurethane SMPs have been shown to be as high as 99.5% and 97.5% respectively after several hours and cycles [15,20,25,58].

Thin film nanoindentation, bulge, and point deflection tests on polyurethane thin film SMP have been conducted with comparable results to traditional mechanical tests, opening the possibility of direct applications using known parameters in thin film applications [3].

The creep response of several polymer formulas have been studied [25,27] as well as the effect of varying the ratio of hard and soft segments on the tensile modulus, heat of crystallization, shape fixity, and shape recovery of polyurethane based SMPs [22].

Moisture, like in polystyrene SMPs, has been shown to decrease the Young's modulus after submersion in water for a period of time. The glass transition temperature has also been shown to decrease by as much as 35 C [10,59,60].

Not directly studied in styrene based SMPs, secondary shapes have been shown to form in polyurethane SMP foams by holding the sample in a deformed shape above T_g for extended periods [23]. Other forms of SMP having been studied include the T_g, strain recovery, creep, and heating and cooling rates of epoxy based systems [24,57] as well as many others [6,16,26].

1.1.2.2.3 Thermally Activated SMP Composites

Alongside studies of neat polymers are investigations of various SMP composites. Cho et al. dispersed carbon nanotubes in a polyurethane SMP resulting in improved mechanical properties and causing the composite to become conductive, which could then be thermally activated by applying a voltage [61]. A similar study with polyurethane SMP using glass fibers by Schmidt et al. also resulted in increased tensile strength and resistance to crack propagation. The study also estimated the optimum fiber weight fraction to be between 10 and 20%, resulting in a best fit balance between improved material strength and residual strain during cycling [62]. Studies with chopped fiberglass and woven fabric reinforcements have also been reported with similar results [13].

Novel heating schemes have been proposed using dispersed nanoparticles allowing the finished product to be inductively heated; negating the need for embedded resistive heating elements requiring wired connections. Inductive heating schemes using nanoparticles such as zinc ferromagnetic particles, superparamagnetic magnetite (Fe_3O_4), and SiC have been proposed [12,24,57,62,63]. Zinc ferromagnetic particles have been shown to sufficiently heat a device with as little as 10% by volume of particles [63], with magnetite showing similar results at 40 weight percent [62]. Epoxy based SMPs have been successfully stimulated using SiC particles at 20 weight percent with the added effect of approximately doubling the strength of the polymer [12,24,57].

1.1.2.3 Applications of Thermally Activated SMP

Although there are several proposed and implemented applications of heat activated shape memory polymers including customizable utensils for the physically disabled and fiber reinforced deployable structures for space applications [64], most proposed devices are either biomedical or militaristic in nature. Morphing aircraft and deformable wing structures have been under investigation recently with the desire to produce multi-mission and more fuel efficient aircraft [65,66]. In the biomedical field, several designs utilizing SMP in stents, aiding in minimally invasive surgery, have been proposed [26,67-69]. Stents made of tert-butyl acrylate monomer with diethyleneglycol diacrylate crosslinker have been proposed for their biocompatibility [26]. Stents impregnated with drugs designed to leach out over time, reducing the chance of rejection and or supplying needed medication have also been tested [67]. SMP foam filled stents have been proposed for use in cerebral vasculature aneurysms utilizing laser heating [68,69]. Other biomedical applications include using the shape memory effect of SMP for sutures. The proposed research showed that in rats, loose sutures could be tightened through

heating, aiding in minimally invasive techniques [5,70]. Thrombectomy devices have been proposed for removing blood clots using SMP wires with memorized spiral shapes [68,71]. Similar thrombectomy devices have also been proposed using inductive heating as the actuation method with nickel zinc ferromagnetic particle doped SMP [63]. With shape memory polymers moving increasingly into mainstream design, ever more devices are being proposed and implemented, with each type of SMP taking their own place based on their unique characteristics.

1.1.3 Light Activated SMP

Effects due to the irradiation of polymers have been under investigation since the 1950s [72,73]. The first formulations marketed as polymers with the ability to generate a force when exposed to light were introduced in the late 1980s and early 1990s [39,74]. These polymer gels containing N-isopropylacrylamide and the light sensitive chromophore trisodium salt of copper chlorophyllin were reported to have reduced in diameter by as much as 40% when cylindrical rods were exposed to 488 nm light. Since then several monomers have been shown to be affected by irradiation and much research has been completed characterizing their response [75].

1.1.3.1 Crosslink Chemistry

Of the two categories of shape memory polymers belonging to the light activated type, by far the most common and most studied are those polymers that undergo a shape change when exposed to an optical stimulus. Polymer systems based on Poly[oxy(methylsilylene)] as well as azobenzene have been shown to reversibly strain under an optical stimulus [32,33,35,38]. The trans-cis transformation of azobenzene is pictured below, as published by Jiang [75], where

contraction occurs under 330-380 nm light and extension occurs under wavelengths greater than 420 nm.

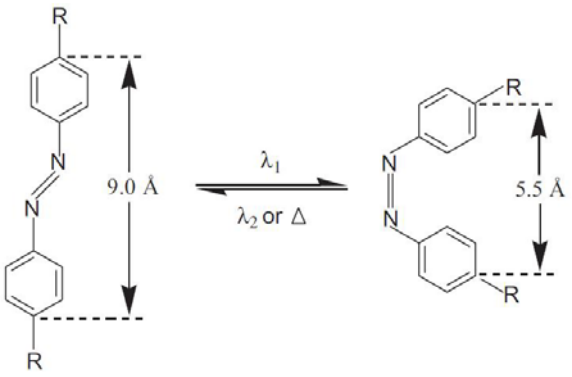

Figure 1.1.3.1-1: Trans-cis transformation of azobenzene when exposed to UV irradiation

The second category of light activated polymer, whose primary response to UV exposure is the formation or scission of crosslinks, thereby increasing or decreasing the strength of the polymer, is both less common and the focus of the presented work. Light sensitive molecular switches, commonly consisting of cinnamic acid (CA), cinnamy-liden acetic acid (CAA), or coumarin moieties, form covalent bonds with each other upon irradiation [47]. Such systems are based on the reversible photo-dimerization brought on by cycloaddition induced by UV irradiation and the corresponding cleaving of crosslinks of cyclobutane derivatives [37,42,48].

The two strategies used to incorporate the photoactive species into the polymer include grafting the photosensitive moieties onto a permanent elastomer network and interpenetrating the network with oligomeric molecules having several photosensitive moieties. As examples, the crosslinked and uncrosslinked chemical structures of coumarin ($C_9H_6O_2$) are shown below in Figure 1.1.3.1-2 as published by Jiang et al. [48]. Also shown below in Figure 1.1.3.1-3 is the photodimerization crosslinking reaction of cinnamic acid [75].

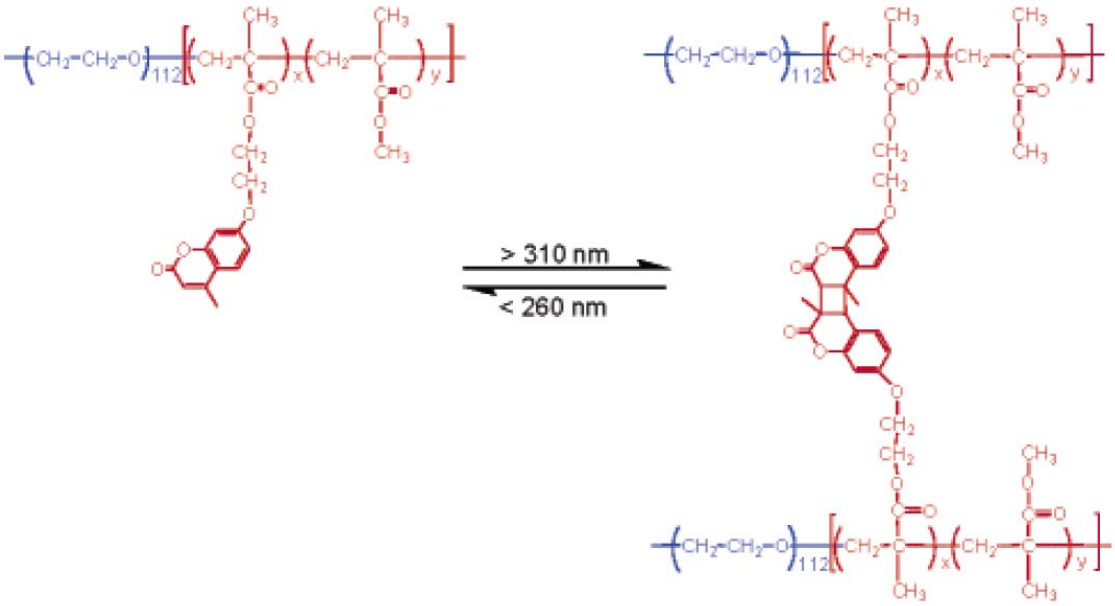

Figure 1.1.3.1-2: UV induced crosslinking reaction of coumarin

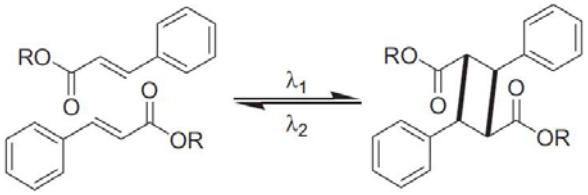

Figure 1.1.3.1-3: UV induced crosslinking reaction of cinnamic acid

1.1.3.2 UV Degradation

The degradation of polymer materials due to exposure to ultraviolet radiation has been studied for some time and is influenced by many factors. Degradation and yellowing of materials has been shown to be dependent on temperature, the presence and concentration of oxygen, radiation dose, radiation dose rate, polymer composition, as well as other environmental and chemical factors. The type and degree of degradation due to UV exposure differs between polymers and can be a combination of simple discoloration, changes in molecular weight, crosslink scission or changes in structure, resulting in changes in mechanical and optical

properties such as absorbance, transmittance, and tensile strength [76-79]. Changes in structure such as the scission of the C-CH_2 bond in polyisobutylene from radiation, causing a change in molecular weight [77], as well as up to a 60% decrease in the tensile strength of polyethylene and ethylene-propylene copolymer have been shown [78]. Table 1.1.3.2-1 below lists a selection of polymers and the ranges of radiation known to cause degradation [76].

Table 1.1.3.2-1: Degradation of select polymer systems [76]

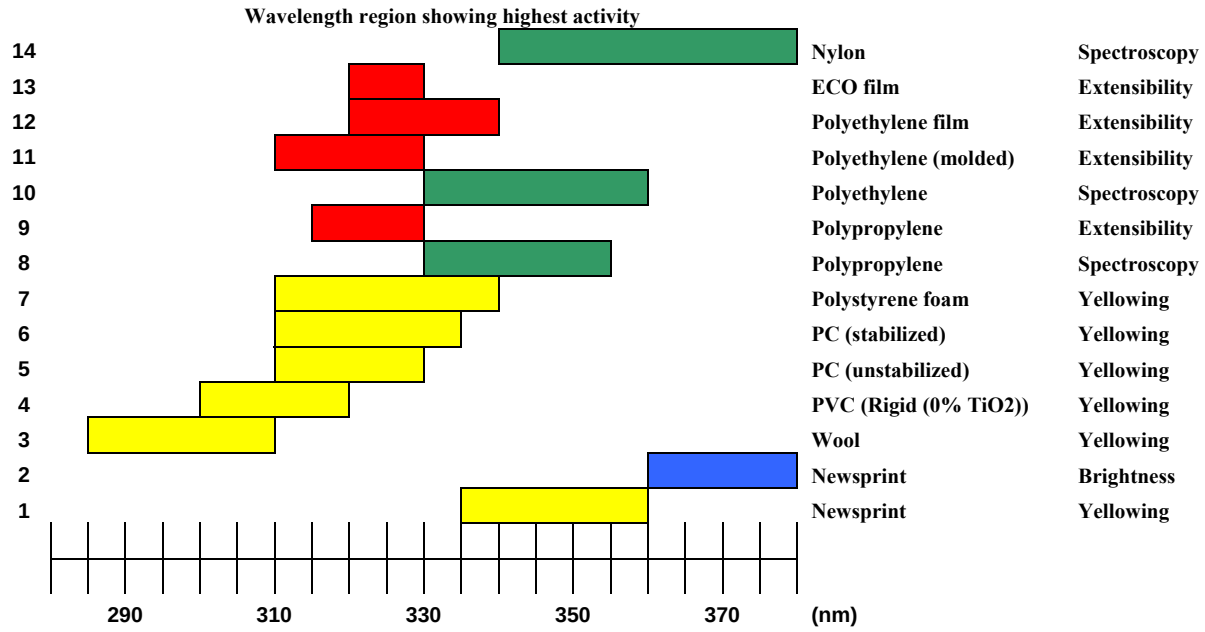

While it is a well known phenomenon that exposure to UV radiation has the ability to degrade polymers and such degradation would affect the life cycle of LASMP in practical applications, such a study is beyond the scope of this thesis. It is however worth noting that, although the exact polymer system is proprietary, steps can be taken to minimize degradation. From the work of Seguchi et al., it is known that increasing the dose rate increases the amount of degradation described by Equation 1.1.3.2-1 [78].

$$\frac{Deg}{r} = kI^{-1/3} \tag{1.1.3.2-1}$$

Where *Deg* represents the magnitude of degradation, *r* is the dose of radiation, *I* is the dose rate of radiation, and *k* is a material constant. From Equation 1.1.3.2-1, the degree of degradation during testing can be minimized by lowering the dose rate.

1.1.3.3 Modeling of LASMP

While there are several mathematical models describing the cure kinetics of photo-cured polymers, invoking for example Arrhenius type equations such as Equations 1.1.3.3-1, which can be adapted to predict the crosslinking that occurs during a finite time leading to the ability to estimate Young's modulus [34]; to the authors knowledge there is a complete lack of constitutive models developed specifically for light activated polymers, taking into account optical stimulation predicting the stress response of the polymer.

$$\frac{X}{X_m} = \frac{kt^n}{1+kt^n}$$
$$k = k_0 e^{-E/RT} \tag{1.1.3.3-1}$$

In Equations 1.1.3.3-1 above, *X* is the extent of cure at time *t*, X_m is the maximum level of curing the polymer is capable of, *k* is a constant, *n* is a material constant, k_0 is a constant dependent on the molecular weight of the polymer, *E* is the activation energy, *R* is the gas constnat, and *T* is absolute temperature. The models that have been derived for use with heat activated shape memory polymers discussed in the previous section, however, may be able to be adapted for

light activated shape memory polymers. For example replacing the quantities $\alpha \dot{T}$ in Equation 1.1.2.1.1-5 and $a\left(\frac{T_g}{T}-1\right)$ in Equation 1.1.2.1.1-7 with activation time dependent functions, such as Equations 1.1.3.3-1, may be sufficiently accurate and flexible for many design and modeling efforts.

1.1.3.4 Experimental Characterization of LASMP

In 2001, Finkelmann et al. published a study on Poly[oxy(methylsilylene)] (PHMS) and its ability to strain as much as 20% when exposed to UV light for 60 minutes. The report also detailed the less often reported temperature dependence of the polymer. The observed maximum attainable strain was seen to decrease from 20% to as low as 16% as temperature decreased from 313 K to 298 K [32]. The most common light activated polymer system belonging to the "shape change" category, however, are those based on azobenzene.

Azobenzene liquid crystal elastomer films have been shown to permanently bend under UV light of 360 nm and unbend under 450 nm [33,35,38]. Polymers based on this system have been reported to experience strains up to 20% with as little as 130 seconds of exposure and can be directionally curled using polarized light [35,38].

Polymers categorized as having a change in modulus as a result of UV irradiation, such as CA and CAA polymer systems, have been shown to crosslink when exposed to light above 260 nm and cleave under light below 260 nm, effectively switching between modulus states with 1.5 hours of exposure time [37,41,47]. By novel application of strain and optical stimulus, various shapes such as cork screws and spirals can also be obtained [37,75]. Studies conducted on coumarin based polymers have shown that the polymer crosslinks when irradiated at

wavelengths near 310 nm and cleaves near 260 nm [48]. Since most light activated shape memory polymers are still in the development stages with molecular formulas and synthesizing techniques varying greatly among practitioners, there is little detailed or numerical published mechanical characterization data available.

1.1.3.5 Applications of LASMP

Although light activated shape memory polymers are still in their infancy, there are a significant number of application opportunities. LASMP's unique characteristic of being able to switch between two strain or modulus states regardless of the temperature makes them attractive in the biomedical field. Several applications have been proposed including smart implants [47,75] or sutures [70] that can be activated without fear of damaging nearby tissue, as is a concern with heat activated shape memory polymers. The non-contact activation feature of the polymer has been proposed as a way to activate LASMP micelles used for targeted drug delivery in cancer and other patients [48]. The polymer has also been proposed for use in high speed actuators for microscale and nanoscale robots, pumps, and optical tweezers [35,38] as well as other light responsive sensors and actuators [75]. Finally, light activated polymers are a candidate material for morphing structures such as aircraft and satellite systems, taking advantage of their ability to permanently change in modulus without the need for continued energy input to overcome environmental losses as well as their relative independence of temperature effects. With a myriad of possible applications, the research initiative developing and characterizing these polymers is just beginning.

2.0 EXPERIMENTAL CHARACTERIZATION

The main focus of the work is to establish a proven experimental technique for accurately measuring the stimulus dependent mechanical properties of light activated shape memory polymer. Because LASMP is a new class of polymer, coherent experimental characterization techniques have not yet been established, thus the first phase of the experimental aspect of the research is to both establish a set of reliable methods for determining the properties of LASMP as well as supply poof of concept data that the chosen polymer monomers and synthesis yield expected results. The experimental results are also used to both calibrate and validate the model presented.

The second phase of experimental work will focus more heavily on refining the polymer formula. It is the goal of the phase II effort to obtain a formula or family of formulas with sufficiently acceptable characteristics to be used in first generation light activated shape memory polymer devices such as adaptable optics.

2.1 EXPERIMENTAL SETUP AND TECHNIQUE

2.1.1 Optical Equipment, Setup, and Characterization

2.1.1.1 Optical Stimulus Equipment and Setup

The optical setup for material characterization of the polymer includes two lasers, a filter, a convex lens, and several mirrors, Figure 2.1.1.1-1. The laser responsible for transitioning the polymer from the soft to the hard state is an Omnichrome Series 56 Ni-Cd class IIIb 150 mW laser outputting at 325 and 442 nm wavelengths at 19.0 and 55.0 mW of optical power respectively. Exiting the aperture of the laser, the beam is directed 13 cm through a 25 mm short pass fused silica filter (NT47-285) manufactured by Edmund Optics that transmits wavelengths from 250 to 385 nm and rejects those from 420 to 485 nm, resulting in a slightly less powerful beam of 325 nm light due to the transmission efficiency of the filter.

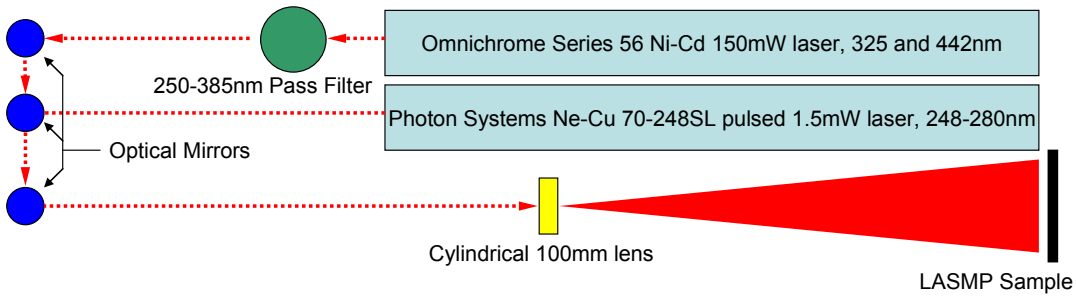

Figure 2.1.1.1-1: Laser pathway

From the filter the beam travels approximately 245 cm, redirected by 2 Newport model 10D20AL.2 broadband optical mirrors, to a fused silica Newport plano-convex uncoated cylindrical lens (CSX100) with a focal length of 100 mm, which spreads the beam to an

experimentally usable size approximately 35 mm in height and 7 mm in width, Figures 2.1.1.2-2 and 3. The properties of the beam will be discussed in much more detail in Section 2.1.1.2. Finally, the diffused beam reaches the sample 62.5 cm from the cylindrical lens.

For transitioning the sample from the hard to the soft state, a Photon Systems Ne-Cu 70-248SL class IIIb pulsed laser is used, outputting from 248 to 280 nm at less than 1.5 mW. For testing, this laser is configured to pulse at 20 Hz at 40 μs each. The exiting light from the Ne-Cu laser travels approximately 208 cm to the cylindrical lens, also directed by 2 optical mirrors.

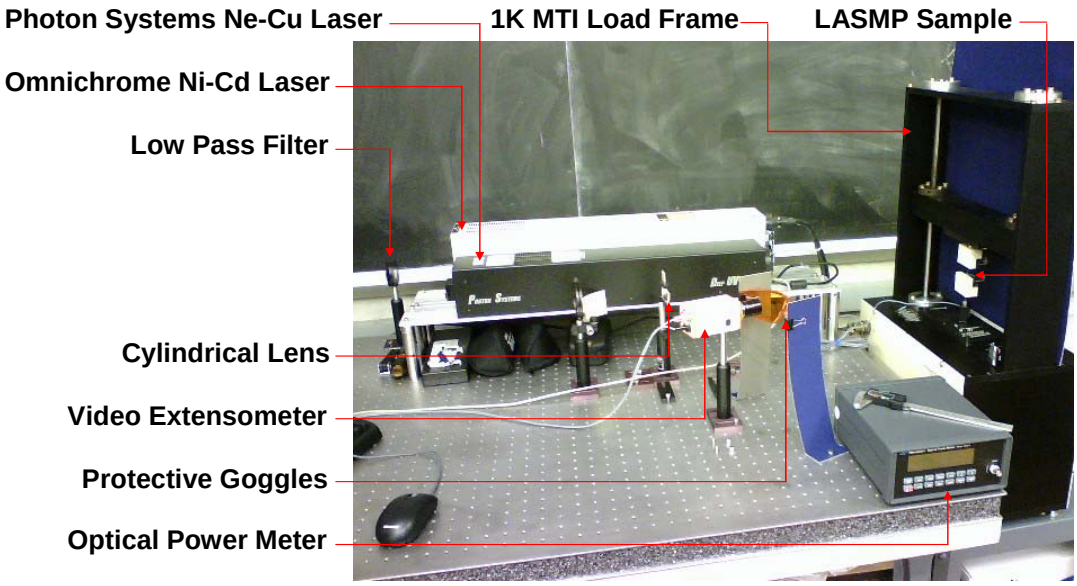

Figure 2.1.1.1-2: Experimental setup used for LASMP material characterization

2.1.1.2 Stimulus Characterization – Spatial Variations

Spatial and temporal characterization of the 325 nm wavelength beam is accomplished via a Newport model 1830-C Optical Power Meter with a 20 mm diameter Newport model 818-UV optical sensor. To measure the total power of the beam the sensor is covered with 1.2 mm thick posterboard with a pinhole approximately 0.58 mm in diameter in the center and simply

placed in the beam path. For sample transmission measurements the sensor is placed behind the sample of interest.

Characterization of the 248 nm wavelength laser is not available because the optical power meter available is not suitable for measuring light from a pulsed laser.

In addition to fluctuating over time, the optical 325 nm wavelength stimulus described above is also non-uniform in space. While it is generally accepted that most lasers will exhibit beams that have a spatial intensity distribution that is Gaussian in nature, it is not always the case [80]. Therefore, it is appropriate to characterize the spatial light distribution in advance of LASMP stimulus characterization. A contour map of the optical power delivered to the sample considered in this work is created by (1) covering the power meter with opaque material with a pinhole, (2) attaching the meter to a sliding 90° optical mounting bracket that is fixed to the crosshead of the load frame, Figure 2.1.1.2-1, and (3) mapping the laser power incident on the sample over a 1 mm square grid. The data is then conditioned in Matlab® using the griddata(cubic) function to produce contour and surface plots of the optical power seen by the sample, pictured as Figure 2.1.1.2-2 and 3 respectively. Figure 2.1.1.2-2 also illustrates how this information is to be used to properly place the sample within the diffused light in order to impose a stimulus that is as uniform as possible.

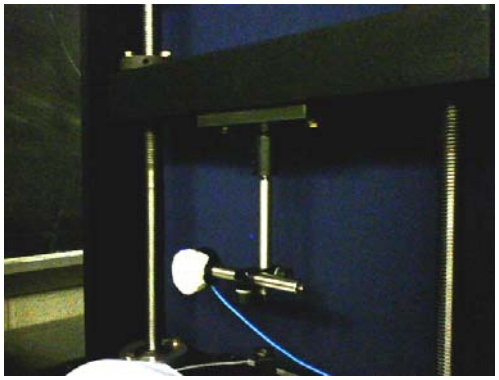

Figure 2.1.1.2-1: Optical power sensor attached to load frame cross-head with sliding bracket

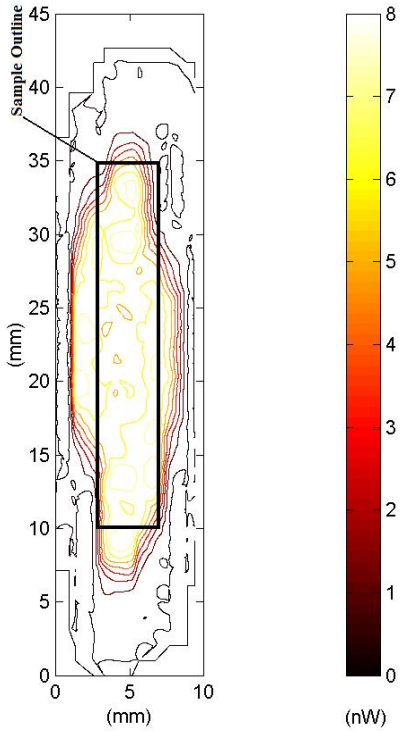

Figure 2.1.1.2-2: Contour plot of optical power as seen by the sample

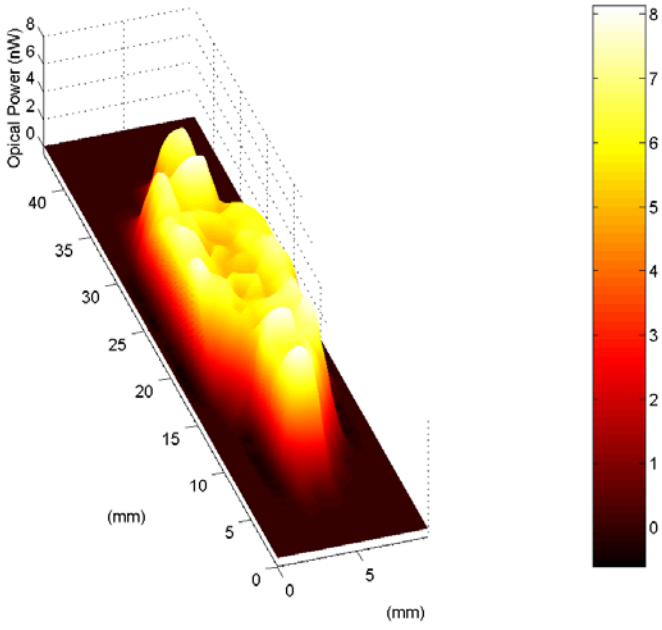

Figure 2.1.1.2-3: Surface plot of optical power as seen by the sample

To determine where within the laser dot the sample lies during testing, a strip of 35 mm film is positioned behind the sample in the load frame and exposed to the 325 nm laser. By examining the resulting shadow of the sample on the film, pictured in Figure 2.1.1.2-4, the position of the sample can be precisely located within the laser dot. For the case performed here, this comparison leads to the sample encompassing the space outlined from 3.0 to 7.0 mm horizontally and 7.5 to 37.5 mm vertically in the contour plot of Figure 2.1.1.2-2. Accounting for the gage length measured by the video extensometer, which will be discussed further later, the vertical space of the sample responsible for mechanical measurement is reduced to the bounds of 10 to 35 mm as illustrated (Figure 2.1.1.2-2).

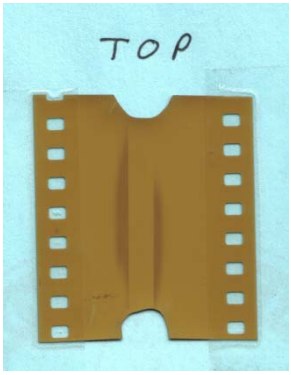

Figure 2.1.1.2-4: Film depicting laser shadow of a sample during testing

As seen in Figure 2.1.1.2-2 and taking into account the area occupied by the sample as described above, although the laser dot is irregular, the area used to transition the sample is relatively uniform in strength. While variations are apparent, the majority of the sample is relatively evenly stimulated. Only 8.8 mm^2 of the sample is exposed to intensities less than 5.0 nW, which corresponds to 9.0% of the total area, with the average and median optical power

intensity being 5.62 and 5.83 nW respectively. From Figure 2.1.1.2-4 and the data represented in Figure 2.1.1.2-2, the power incident on the sample, and thus power required for transition, can be calculated. Of the available 9.2 μW of optical power emitted by the laser, 7.7 μW is incident on the sample and responsible for transition.

2.1.1.3 Stimulus Characterization – Temporal Variations

By placing an optical power meter at a fixed point in the path of the 325 nm wavelength laser beam and measuring the intensity of the light over a length of time, fluctuations in the power output of the laser can be measured. The laser utilized for this particular study exhibits sinusoidal optical power output with a period of 1200 s (~20 min) and has a difference of approximately 6.76% between the maximum and minimum power output. Since the polymer considered in the first phase of experimental characterization requires 60 minutes or more to fully transition, these fluctuations are noted but are not believed to greatly affect testing. Ultimately however, LASMP development efforts are expected to yield formulations that transition in about 1 second. To account for these fluctuations in incident power when testing polymers having quicker transition times, prior to testing it will be essential to determine the position and direction of the laser on its intensity curve when computing the polymer's power requirements.

Figure 2.1.1.3-1 is a graph depicting power readings over 3.3 hours using the optical power meter described previously with a 0.58 mm diameter pinhole. The sensor is placed behind a 0.9 mm thick sample with readings taken every 30 seconds. The graph shows a fluctuation in the optical power being transmitted through the sample of 6.76%. It also demonstrates the gradient of light intensity transmitted through the sample. At the beginning of the test, almost no light is penetrating through the sample, being diffused or absorbed for transitioning of the bulk of

the material. At the end of the test, more of the light provided to the sample is transmitted. It should also be noted that the optical power meter in the same configuration, not being behind a sample, measures an optical intensity of approximately 354 nW, indicating that 99.94% of the incident light is scattered or absorbed by a 0.9 mm thick sample.

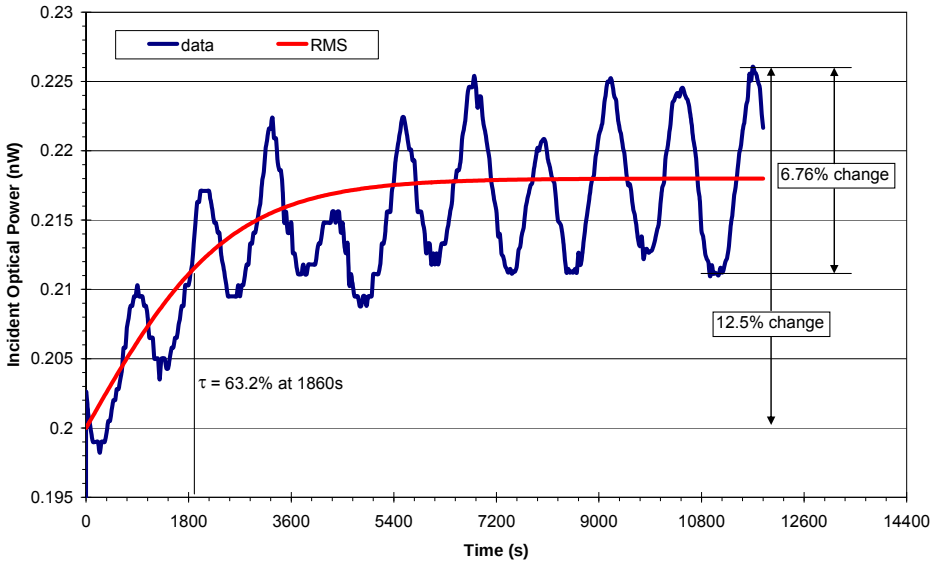

Figure 2.1.1.3-1: Optical power transmitted through a 0.9mm thick LASMP sample

LASMPs are unique in that the absorption of light stimulates transition, however, the polymer must also transmit light through its thickness for bulk transitioning of the polymer. Because of this unique material property, it is pertinent that we measure the absorption of the polymer [81]. Consider the Beer-Lambert-Bouguer law

$$A = \log_{10}\left(\frac{I_o}{I_i}\right) \tag{2.1.1.3-1}$$

$$\alpha = \frac{4\pi k}{\lambda} \tag{2.1.1.3-2}$$

$$A = \alpha l c \tag{2.1.1.3-3}$$

where A is absorbance, I_o is the intensity of the incident light, I_i is the intensity of the light exiting the material, α is the absorption coefficient, k is the extinction coefficient, λ is the wavelength of the light, c is the concentration of the absorbing species in the material, and l is the distance light travels through the material. To measure the absorption of the polymer, the optical power meter is positioned behind a sample in the grips of the load frame and measurements taken at incremental strains. The thickness of the sample at each measurement is estimated using Poisson's ratio, known from previous tests. Figure 2.1.1.3-2 shows the results of such a test and, as can be seen, the absorption of the polymer is nearly linear with sample thickness, supporting the use of the Beer-Lambert-Bouguer law, Equations 2.1.1.3-1 through 3.

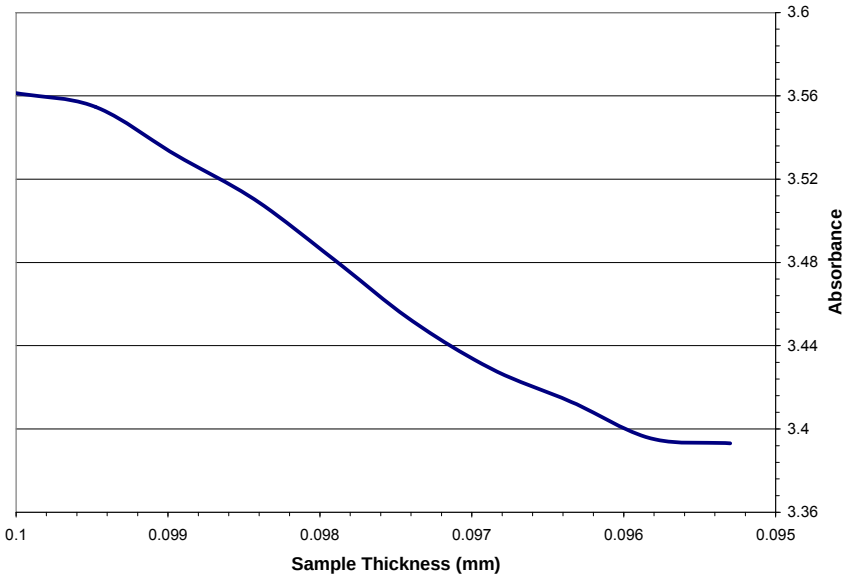

Figure 2.1.1.3-2: Absorbance of LASMP based on sample thickness

As LASMP transitions from a soft state to a hard state, the absorbance of the polymer, and the polymer's absorption coefficient, change. The result is that to fully characterize the absorbance of the polymer, measurements must be taken at several different exposure times resulting in an equation for the absorbance of the polymer dependent on the thickness of the polymer, l, the concentration of the absorbing species, c, and the absorption coefficient, α, which is in turn dependent on laser exposure time. The paradox is that for LASMP to perform well a high concentration of absorbing species is needed while Beer's Law is known to become less accurate at high absorbing species concentrations. Further, Beer's Law is also known to become less accurate for materials with high scattering, which is also a trait of LASMP [81]. A possible solution is to simply make the absorption coefficient also dependent on material thickness. However this strategy makes the equation phenomenological and thus cannot be extrapolated to thicknesses untested.

2.1.2 Mechanical Equipment and Setup

The mechanical equipment used for material characterization includes a small tabletop load frame with tensile grips and a video extensometer, Figure 2.1.1.1-2. The load frame is an MTI-1K tabletop screw driven load frame with a 2.5lb Transducer Techniques load cell, model MDB-2.5, accurate to 7.5E-4lb (3.3mN). A Messphysik ME46-NG video extensometer is used to track both axial and transverse strain of the sample using a Mintron model MTV-13W1C digital camera with a 50mm Tamron lens, Figure 2.1.1.1-2. The accuracy of the video extensometer depends on the angle and tilt of the camera, quality of sample markings, lighting, and the camera field of view, but is estimated to be less than 1.5 μm based on the manufacturer's

manual for the setup shown. The tensile grips are pictured in Figure 2.1.3-1 and are typical, hand tightened steel grips. The grip faces were sand blasted to provide improved grip on the specimens.

Because it is desirable to establish the property change of LASMP as a function of time, *in situ* characterization is required. The transition time for the first phase LASMP formulas is approximately one hour. For this state of development a brief tensile test, approximately 2 minutes in duration, is periodically performed with the grips returning to their "pre-test" position after completion of each cycle. As compared to the one hour transition time, it is reasonable to assume the test is instantaneous relative to the amount of time required for full transition. In such an instance the load frame can simply be programmed to perform a low cycle fatigue test with the proper dwell between cycles applied with the laser remaining on for the duration of the test. Tensile tests were conducted at 0.25 mm/min, representing a strain rate of approximately 1% strain per minute with each cycle stopped below the yield stress of the polymer. Young's modulus of the polymer is then calculated as the initial slope of each individual stress strain curve.

In anticipation of future LASMP formulas with much faster response times, custom software has been created by MTI per University of Pittsburgh specifications. This control strategy effectively converts the small tabletop load frame into a DMA that waits for user input before completing each cycle. Typical DMA and other commercial experimental devices are not adequate for LASMP testing because of the type and number of systems that need access to the sample during testing. The software is easily interfaced with other programs, such as Labview®, allowing the interfacing of the lasers, load frame, video extensometer, optical power meter, and other controlling devices such as shutters. This experimental setup effectively allows the laser to

be turned off or shuttered during each cycle of testing resulting in an instantaneous measurement with respect to laser exposure during transition allowing extremely small time spans between data points. Also expected with the introduction of polymers with faster transition times is the need for conditioning the sample before testing. While every effort is made to shield the test samples from ambient radiation between sample creation and characterization, it is not feasible to block *all* ambient radiation. While this is not a significant issue for polymers with large transition times, such as those presented, it must be accounted for in future formulations more sensitive to ambient light. To account for this, future formulations will require an extra step of conditioning for a period of time, such as exposure to 248nm light for several times the time required for transition, to ensure that the polymer is in a known reference state. It will also become required that the optical properties of the material be investigated more thoroughly, such as the polymer's reflectivity and scattering characteristics.

2.1.3 Sample Preparation

Samples of various formulations are typically received as thin film sheets ranging from 25 x 25 mm to 40 x 40 mm with thicknesses between 0.05 to 0.25 mm and are in the elastic state with little to no photo-crosslinks. Preparing the samples for testing involves cutting the samples into strips compliant with ASTM Standard 882 for thin films requiring at least an 8 to 1 width to thickness ratio. Cutting of the samples is performed using a metal ruler as a guide and a razor blade knife. Vertical and horizontal lines are then applied with white paint to the back of the samples for tracking by the video extensometer. The samples, approximately 4mm wide, 0.1 mm thick, and having a gage length of 20 mm are then cleaned with 91% isopropyl alcohol before being centered in the grips of the load frame, shown in Figure 2.1.3-1.

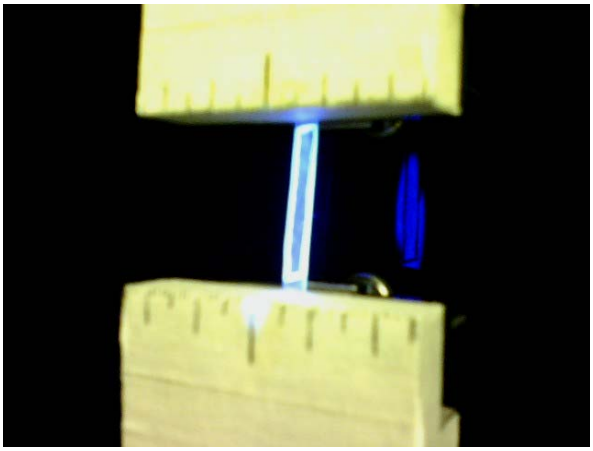

Figure 2.1.3-1: Standard LASMP sample with 325nm laser

An important area of interest when mechanically testing any polymer is the choice of sample type and the interface between the grips and the sample. Dogbone samples are generally preferred because their shape makes it possible to argue that the thinnest segment, or gage length, of the sample dominates the strain response, thereby minimizing grip effects. However, LASMP synthesis constraints result in sample sizes too small to justify the material loss associated with the creation of dogbone samples. Also, it should be noted that when transitioning from the soft to hard states, only the sample that is exposed to light transitions. The result is that the portion of the sample covered by the grips remains soft. When testing a sample in this state, the sample tends to undergo slight necking in the region of the grips. In order to prevent this phenomenon from skewing the data, resulting in an artificially low Young's modulus measurement, a video extensometer is employed. Because the entire sample is subject to a known load and the video extensometer monitors deformation in the central portion of the sample, far from the grips, the property variation at the grips is eliminated from the characterization data.

2.1.4 Equipment Lists

Table 2.1.4-1: Optical Experimental Equipment

Item	Manufacturer and Model	Description
Ni-Cd Class IIIb 105mW Laser	Omnichrome series 56	output 325nm at 19.0mW output 442nm at 55.0mW
Ne-Cu Class IIIb Pulsed Laser	Photon Systems 70-248SL	output 248-280nm at <1.5mW 20Hz, 40μs pulses
Short-pass Fused Silica Filter	Edmund Optics NT-47-285	25mm diameter transmission band 250-385nm rejection band 420-485nm cut-off wavelength 400nm
Broadband Metallic Mirror	Newport 10D20AL.2	Pyrex construction 25.4mm diameter 6.0mm thick 250-600nm wavelength range
Plano-convex Cylindrical Lens	Newport CSX100	MM2-1A aluminum mounts uncoated 50.8 x 25.4mm dimensions 100mm focal length
Optical Power Meter	Newport 1830C	818-UV 20mm sensor

Table 2.1.4-2: Mechanical Experimental Equipment

Item	Manufacturer and Model	Description
Tabletop Load Frame	MTI-1K	screw driven
Load Cell	Transducer Techniques MDB-2.5	2.5lb capacity 3.3mN accuracy
Tensile Grips	custom	steel, hand tightened sand blasted grip surface
Video Extensometer	Messphysik ME46-NC	Mintron MTV-13W1C digital camera Tamron 50mm lens
Digimatic Micrometer	Mitutoyo MDC-1" SB no. 293-831	1.5μm accuracy range 0-1" resolution 0.00005"
Digital Calipers	Marathon CO-031050	0-150mm range 0.01mm accuracy
35mm Color Print Film	Kroger	400 speed
Razor Blade Knife		
91% Isopropyl Alcohol	CVS	

2.2 EXPERIMENTAL RESULTS

2.2.1 Characterization

Since the polymers being tested are new, the degradation of their mechanical properties due to repeated strain cycles is unknown. Thus before material changes due to an optical stimulus can be measured, a reference sample must be tested evaluating the mechanical effects of the testing procedure on the sample. To characterize the fatigue properties of the polymer, a sample is tested per the method above for 60 cycles between strains of 0.05% and 2.5% at a rate of 0.5 mm/min. For example, formula EAS-220-20E decreased from a stiffness of 1.45 MPa to a stiffness of 1.22 MPa over 60 cycles, corresponding to a drop in Young's modulus of 15.9% in the absence of optical stimulation. Since formula EAS-220-20E is seen to increase from 5.17 to 32.0 MPa when exposed to 325nm light, discussed further below, it can be assumed that the increase in stiffness is a result of the polymer's reaction to the radiation and not a result of the mechanical test procedure.

Conversely, the decrease in stiffness due to exposure to 248nm light, seen for example in formula EAS-155-115 shown in Figure 2.2.1-5, can also be attributed to a reaction to incident radiation since the decrease in stiffness is much larger than that measured when the sample is shielded from any stimulus source. Any temperature changes due to the absorption of photons by the polymer, thus altering the sample's material properties, must also be considered. Polymers of similar structure to the LASMP samples tested have specific heats ranging from 103.4 to 215.3 J/mol*K [148]. Using the total optical energy incident on the sample during testing shown in Figure 2.2.1-1, if all of the optical energy is absorbed as heat in the sample and there is no heat loss to the surrounding environment, formula EAS-155-115 will see a rise in

temperature between 3.2 and 6.8 C and formula EAS-155-93 will experience an increase in temperature between 7.1 and 14.7 C. Since only a portion of the optical energy incident on the sample during testing is absorbed as heat, the remaining amount reflected, transmitted, or utilized for crosslinking, with a portion of that heat being diffused to the sample's surroundings, the resulting small temperature changes are not believed to significantly impact the test results.

Experimental characterization includes tests on LASMP sample formulas designated LASMP Sample 1, LASMP Sample 2, AKK-171-60, AKK-171-64, EAS-155-93, EAS-155-115, EAS-155-143, EAS-220-20D, and EAS-220-20E. These designations have been introduced by the manufacturer, CRG Industries. LASMP Samples 1 and 2, AKK-171-60, and AKK-171-64 had marginal performance characteristics and are thus omitted here. The results from samples EAS-155-93, 115, and 143, which are used for model calibration and validation in later sections, as well as samples EAS-220-20D and 20E are presented below.

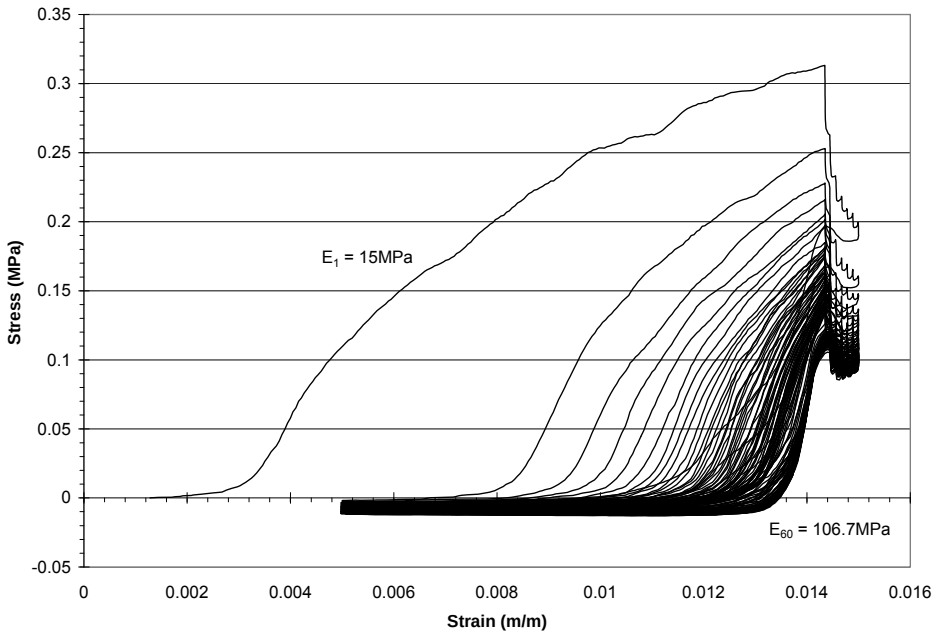

Figure 2.2.1-1: *In situ* test results of formula EAS-155-93

Formula EAS-155-93, Figure 2.2.1-1, was the first formula to achieve a significant modulus change but at the expense of less favorable creep characteristics. The formula was able to transition from a Young's modulus of 15 MPa to that of 106.7 MPa when exposed to the 325nm laser for 1.5 hours, a 610% increase. The rate of change will be discussed later and can be seen in Figure 2.2.1-3. As can be seen from the graph, hysteresis and creep are significant issues. The slow recovery of the polymer is noticeable in the large hysteresis loops in Figure 2.2.1-1, also showing approximately 1.2% of un-recovered strain, 0.8% of which resulting from the first cycle. This un-recovered strain however, as with all of the samples tested, is not believed to be due to plastic deformation but rather the grips of the load frame returning to their initial state faster than the polymer can recover. Given sufficient time, all of the samples tested recovered to their initial dimensions.

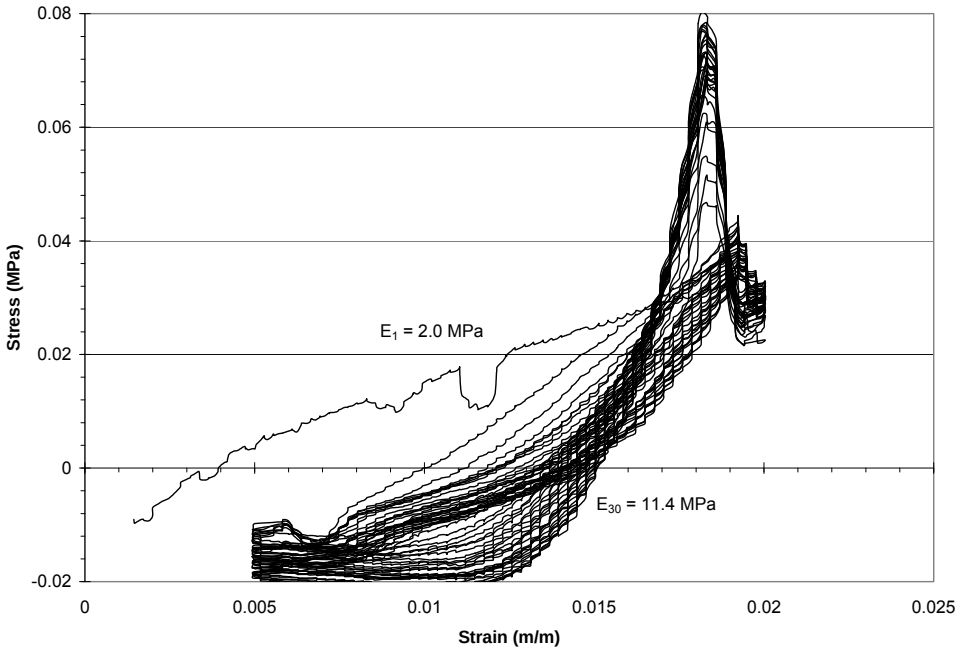

Figure 2.2.1-2: *In situ* test results of formula EAS-155-115

Formula EAS-155-115, Figure 2.2.1-2, showed similar results as formula EAS-155-93 with the exception of the magnitude of Young's modulus. The formula exhibited a modulus increase of 470% from 2.0 MPa to 11.4 MPa when exposed to the 325nm laser for 1.75 hours. Creep is slightly improved, having smaller hysteresis loops and about 1.5% unrecovered strain. Poisson's ratio for this formula was measured to be 0.42 when the polymer is in its hard state and 0.29 when in its soft state. It should be noted in Figure 2.2.1-2, that the measured stress during the test becomes negative. This is a result of both the grips returning to their pre test position faster than the polymer can recover and also an indication of unrecoverable strain. Also evident in the figure are sharp peaks in the stress at the end of each cycle, this is a result of the load frame and is not believed to be a material property.

Figure 2.2.1-3 below displays Young's modulus of formulas EAS-155-93 and EAS-155-115 as a function of stimulation time. As can be seen, both formulas closely follow a logarithmic transition from hard to soft, shown by the solid line in Figure 2.2.1-3. Figure 2.2.1-4 shows the evolution of Young's modulus of the same two samples but with respect to radiation dose (the total accumulated incident radiation energy). The two graphs differ slightly due to the size difference between the two samples and the spatially non-uniform activation energy mapping, Figure 2.1.1.2-2, resulting in different total incident power available for transition.

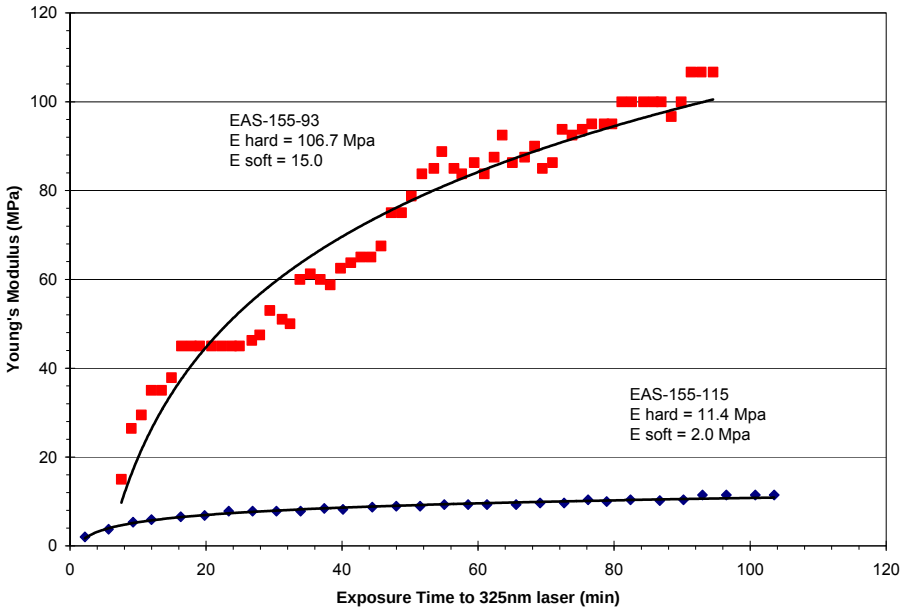

Figure 2.2.1-3: Young's modulus evolution of formulas EAS-155-93 and 115 with respect to exposure time

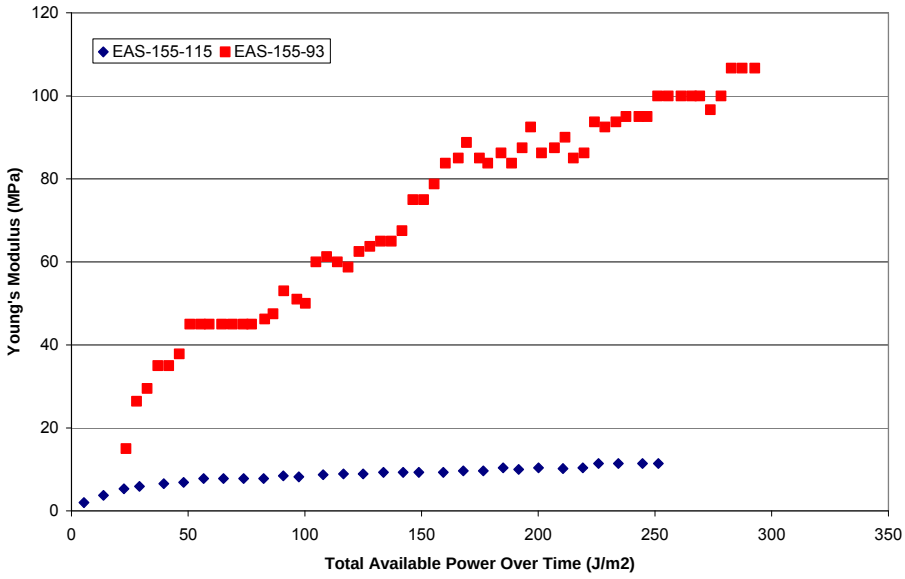

Figure 2.2.1-4: Young's modulus evolution of formulas EAS-155-93 and 115 with respect to available power

Figure 2.2.1-5 is the result of formula EAS-155-115 being exposed to 325nm wavelength light at 4.05mJ/m^2 for 30 minutes to transition from the soft to the hard state; then periodically tested while being exposed to 248 nm wavelength light to transition back to the soft state. The virgin polymer has a Young's modulus of 5.5 MPa before being hardened to 33.3 MPa. After approximately 200 minutes (3.3 hours) of reverse stimulus the polymer reaches a quasi steady state at 20.8 MPa, resulting in 45% recovery. The longer exposure time is due to the characteristics of the laser. The 248nm laser emits pulses at 20Hz that are 40μs in duration as compared to the steady beam of the 325nm laser, resulting in only 800μs of laser exposure per second during the test. Thus 200 minutes of 248nm reverse activation is the equivalent of 9.6 seconds of 325nm activation. Figure 2.2.1-5 does not, however, consider any damage or degradation to the backbone of the polymer as a result of irradiation, which like crosslink scission would also result in decreased stiffness. Although not performed for the shown case, later studies of subsequent polymer formulations have been shown to become stiff again after being softened, indicating that the softening taking place when exposed to 248nm light is at least in part due to crosslink scission.

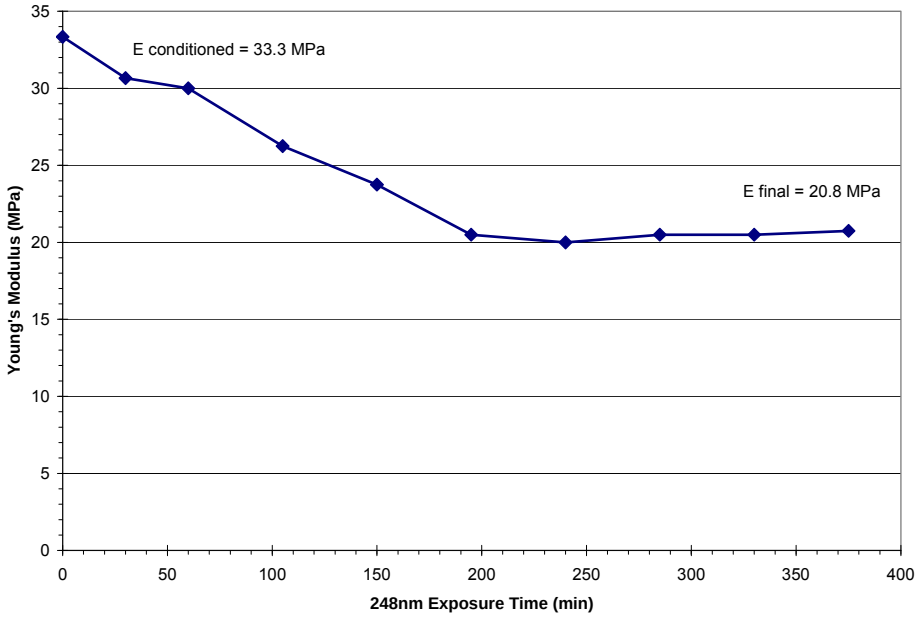

Figure 2.2.1-5: *In situ* softening test results of formula EAS-155-115

The final two formulas tested were EAS-220-20D and 20E. Formula EAS-220-20D exhibited an increase in Young's modulus of 739% over 13 cycles and 2.4 hours of exposure to the 325 nm laser, increasing from an initial value of 3.4 MPa to a final value of 32.5 MPa. The formula did, however, have slightly less desirable creep characteristics as compared to formula EAS-220-20E with approximately 1.1% of irrecoverable strain.

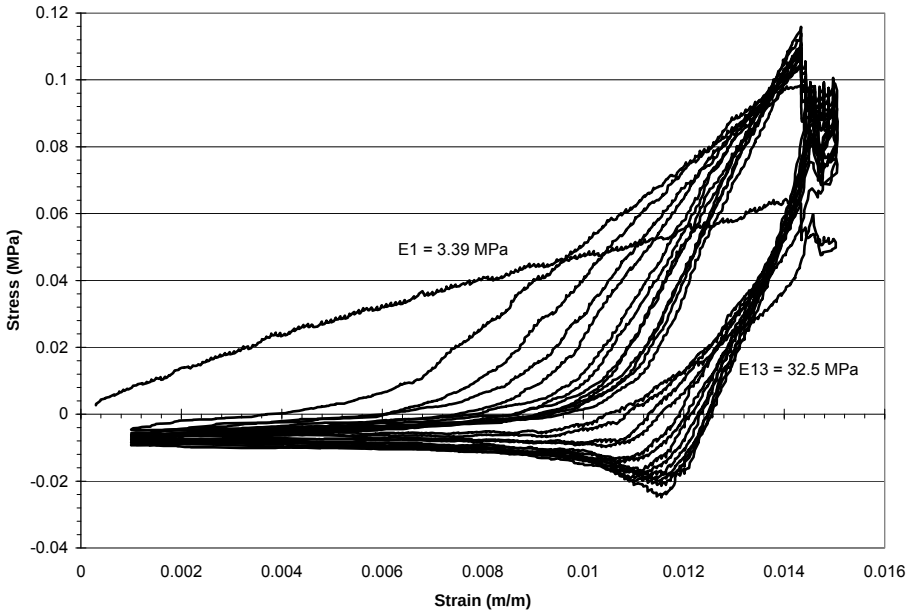

Figure 2.2.1-6: *In situ* test results of formula EAS-220-20D

Formula EAS-220-20E also displayed significant improvements over initial formulas increasing in Young's modulus by 519%. The sample was exposed to 325 nm light for 2.1 hours with an initial modulus of 5.2 MPa transitioning to a final modulus of 32.0 MPa. Despite needing longer to recover from applied strain, indicated by the large hysteresis loops, the polymer had improved creep characteristics, having 0.6% of irrecoverable strain over 13 cycles between 0.05 and 1.0% applied strain.

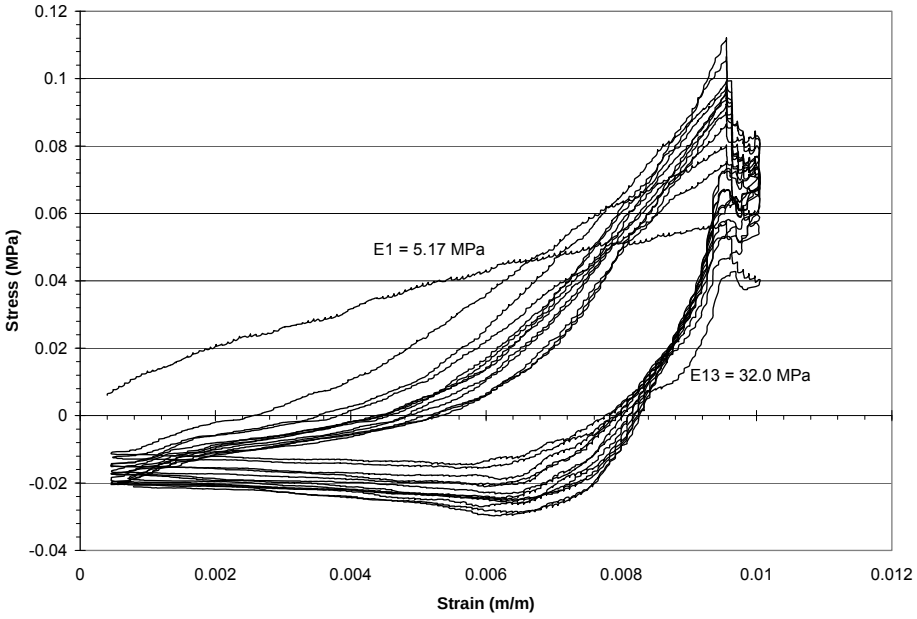

Figure 2.2.1-7: *In situ* test results for formula EAS-220-20E

Pictured below in Figure 2.2.1-8, is a time scale plot of the evolution of the samples' Young's moduli during testing. As can be seen from the graph, and like earlier formulations, both formulas EAS-220-20D and 20E exhibit logarithmic trends with respect to time. Assuming that steady state is reached at 32.0 MPa at about 100 minutes, the resulting time constant (63.2% of steady state) is approximately 63 minutes.

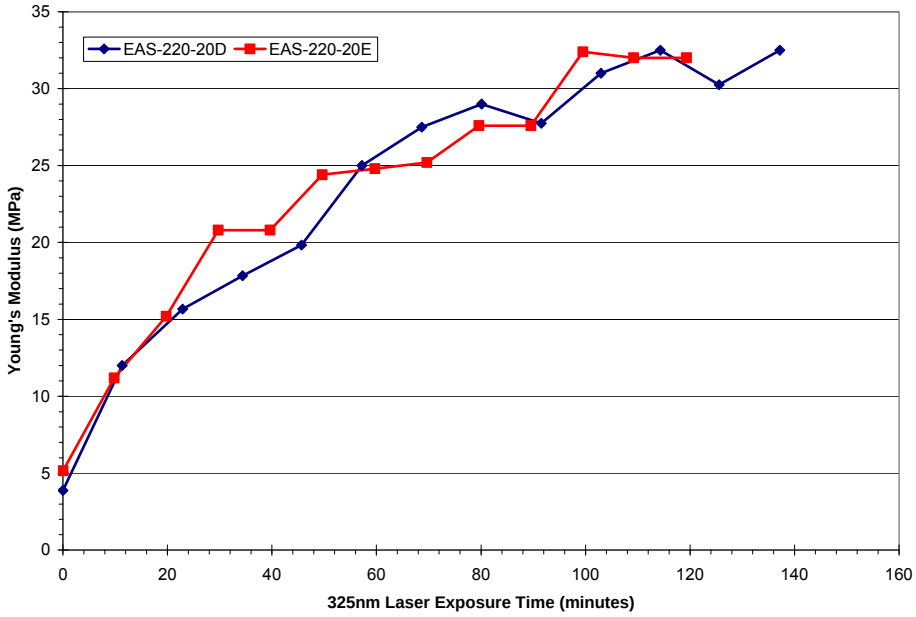

Figure 2.2.1-8: Young's modulus versus time for formulas EAS-220-20D and EAS-220-20E

As described in Section 2.1.1.2, the optical power required for transitioning the polymer can be calculated. Knowing the position of the sample from Figure 2.1.1.2-4 and its dimensions, the fraction of optical radiation and thus the amount of energy incident on any sample can be calculated, shown in Table 2.2.1-1. Using the optical power meter, the 325 nm laser beam has a strength of 9.2 μW at the sample after passing through the filter, cylindrical lens, and mirrors. Applying the fractional amount of optical energy reaching the sample then reduces the amount of energy available for transition for each sample to those listed below in Table 2.2.1-1, averaging approximately 50.5 mW/m^2. This corresponds to between 9.8 and 48.3 mJ of radiation during transition, or between 0.75 and 5.19 J/g. The slightly differing numbers associated with the amount of optical energy available for transition are a result of differences in sample sizes and the non-uniform distribution of incident power. It should also be noted that not all of the light exposed to the sample is utilized, as designed. A portion of the light is transmitted through the

sample, as indicated in Figures 2.1.1.2-5 and 6, as well as reflected from the sample's surface, or scattered.

Table 2.2.1-1: Activation energy incident on sample

Formula	Area mm^2	Incident Fraction	Activation Time minutes	Mass g	Power mW/m^2	mJ	J/g
60	113.2	0.65	118	0.052	52.7	42.3	0.82
64	114.9	0.66	118	0.057	52.5	42.8	0.75
93	105.9	0.59	89	0.012	51.6	29.1	2.47
115	38.7	0.17	105	0.009	40.5	9.8	1.14
143	79.2	0.45	129	0.006	52.0	31.9	5.19
20D	99.7	0.60	146	0.033	55.4	48.3	1.46
20E	119.2	0.63	126	0.040	48.9	44.2	1.11

To test LASMP's material characteristic dependence on the intensity of the incident light, the optical power supplied to the sample is reduced yielding Figure 2.2.1-9. Initially, the two tests are similar, having comparable moduli and slopes. After approximately 10 minutes, however, the sample exposed to lower incident optical intensity reaches steady state at 10.8 MPa while the sample exposed to higher optical power continues to harden.

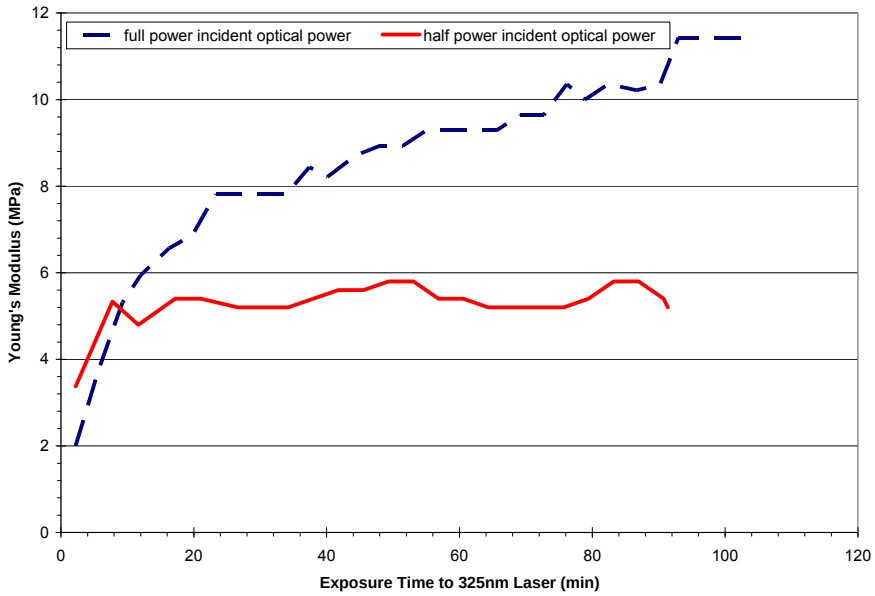

Figure 2.2.1-9: Effect of incident light intensity on material response

As shown in Figure 2.2.1-10 and described in Section 2.1.1.2, the optical power transmitted by the polymer decreases exponentially with thickness. This phenomenon is believed to produce the result seen in Figure 2.2.1-9 of the lower intensity sample reaching quasi-steady state earlier than the sample irradiated at full power.

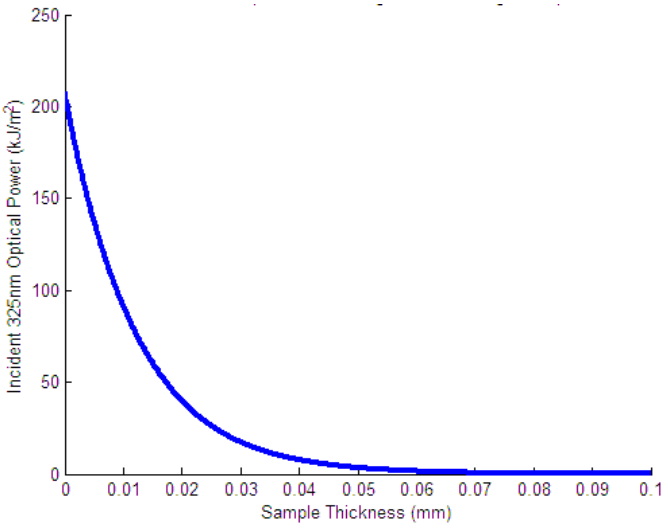

Figure 2.2.1-10: Optical power degradation through sample

3.0 CHEMICAL KINETIC MODEL

It is well known that the transmission of optical power through the thickness of materials follows an exponential decline. Since crosslink formation and scission are directly related to the amount of optical energy available and the through thickness distribution of optical energy is non-uniform, it can be assumed that the through thickness distribution of crosslinking, and thus the modulus of the material, is also non-uniform. This has been shown by Ikeda et al. working with an azobenzene liquid-crystalline gel reporting activation to a depth of only 1μm of a 10μm thick sample [33]. The experimentally derived material parameters presented above in Section 2.2 are an average across the thickness of the sample. Thus, a model is needed to characterize the through thickness distribution of crosslinking and the evolution of Young's modulus of the material as a function of position within the sample. With different thicknesses of samples and varying optical intensities used to transition the samples, a model predicting the theoretical material properties possible with each formulation would allow direct comparison across all formulations and activation techniques. Such predictions are also used to both calibrate and validate the multi-scale model presented in Chapter 4. Section 3.1 below illustrates the derivation of one such model that predicts the time and spatial varying optical intensity, concentration of crosslinks, the evolution of the sample averaged modulus, and the theoretical maximum Young's modulus.

3.1 MODEL DEVELOPMENT

From the Beer-Lambert-Bouguer Law; the optical intensity of light through the thickness of a sample decays exponentially. From data collected to generate Figure 2.1.1.2-6, this decay is found to be,

$$I(x) = I_0 e^{-82x} \tag{3.1-1}$$

where x is the through-thickness position. The chemical kinetics of the system are assumed to be bimolecular in nature; making the reaction causing cross-linking second order, Equation 3.1-2 [82].

$$\frac{\partial P}{\partial t} = k_1 S(S - P) \tag{3.1-2}$$

Here, P is the concentration of cross-linked product, t represents time, k_1 is a constant, and S is the concentration of optically activated species. The degree of cross-linking is assumed to be proportional to the intensity of the light and the concentration of photo-active species at any given point and time, thus,

$$S = k_2 IU \tag{3.1-3}$$

where, k_2 is a constant, U is the concentration of uncross-linked photo active species, and I is the light intensity at the given location, expressed by Equation 3.1-1. In the calculation of S in Equation 3.1-3, it is also assumed that once a photon has interacted with and activated a

functional group giving it the ability to crosslink, that the group remains active and results in the creation of a crosslink regardless of time or spatial constraints. Realistically, an activated group is limited in the amount of time available to crosslink. If a suitable counterpart is not available within a given time, the energy imparted by the photon is either re-radiated or absorbed and diffused as heat in the polymer. It is important to note the distinction between *S*, the concentration of optically activated species, and *U*, the concentration of optically active species. *U* is the amount of material in the sample that, given enough time and optical energy, has the ability to cross-link. *S* is the amount of material in the sample that, at the current time, has sufficient optical energy to cross-link.

The local modulus of the polymer at any given point in the material is assumed to be proportional to the degree of cross-linking. Thus, having an expression for the change in concentration of cross-linked product *P* with respect to time and the change in concentration of optically activated species *S*, Young's modulus of the polymer at any point through the thickness of the sample may be expressed as,

$$E = k_3 P + E_0 \tag{3.1-4}$$

where k_3 is a constant and E_0 is the experimentally determined initial Young's modulus of the sample before laser exposure. Equation 3.1-4 predicts the modulus at any given point and time where the quantities *I*, *P*, *S*, and *E* are dependent on position, *x*. Finally, the maximum attainable value of Young's modulus at any given location, *x*, within the sample is fixed at E_{max} while Young's modulus for the entire sample is found by integrating Equation 3.1-4 over the depth of the sample.

From Equation 3.1-2, we assume that before exposure to the laser the concentration of cross-linked product P is equal to 0. The equation is then evaluated at the time τ, when all possible photo crosslinks have formed, resulting in dP equaling S. We then solve for k_1 as

$$k_1 = \frac{1}{\tau * U_0} \tag{3.1-5}$$

The time τ represents the time constant for the reaction and is found by phenomenologically fitting the initial slope of the predicted time evolution of Young's modulus curve, Figure 3.2-1, to experimental data. From Equation 3.1-3, we again assume sample conditions before light exposure: I at $x = 0$, the front face of the sample, is equal to I_0, U is equal to U_0. We then assume that the amount of optical energy incident on the front surface of the sample is sufficient to activate all of the available uncross-linked photo active material, thus S is also equal to U_0. Then,

$$k_2 = 1/I_0 \tag{3.1-6}$$

Finally, from Equation 3.1-4 we assume that as time approaches infinity, the Young's modulus of the total sample, and at every position x within the sample, should approach $E_{max.}$ Also, all of the photo active species in the material should have undergone cross-linking, resulting in P approaching U_0. Then,

$$k_3 = \frac{E_{\max} - E_0}{U_0} \tag{3.1-7}$$

As can be inferred from Equations 3.1-2 through 3.1-4, k_1 is related to the efficiency at which the polymer mechanically crosslinks given an acceptable environment. An acceptable environment is associated with the amount of optical energy available, the spatial location of cross-linking polymer chains within the sample, as well as other factors. k_2 is representative of the polymer's optical efficiency and the degree to which available light is utilized for cross-linking versus, transmitted, reflected, or absorbed as heat. The constant k_3 is then a measure of the effect cross-linking has on the magnitude of the sample's stiffness. Finally, the value of E_{max} is varied until the resulting curve of the total sample Young's modulus versus time coincides with experimental data. The resulting model includes two phenomenological constants, τ and E_{max}, which are found by fitting the model to experimental data. E_{max} is then the theoretically predicted maximum Young's modulus of the polymer, which also corresponds to the modulus of an individual polymer chain.

Although the model has been shown to be accurate in the presented cases, there are two known variations between model assumptions and the actual physics of transition. First, while the model assumes that 100% photo induced cross linking is possible, there are physical and spatial restraints in the polymer that prevent this. In reality, crosslinks can only be formed when two photo-crosslinkable end segments are both physically close to one another and have sufficient mobility. Such phenomena could be introduced to the model by way of an efficiency parameter multiplying k_1 in Equation 3.1-5. Such an efficiency parameter would require an in-depth study of crosslink formation and would vary between different formulas, and as such is beyond the scope of the presented research and left for future study.

3.2 MODEL RESULTS AND PREDICTIONS

Figure 3.2-1 illustrates the predicted time evolution of the volume averaged stiffness as compared to experiment for formula EAS-155-115; corresponding to a theoretical value of E_{max} of 110 MPa. Hence if cross-linking of every polymer chain within the sample occurs, the resulting volume averaged Young's modulus would be 110 MPa. As mentioned earlier, because it is physically improbable that 100% of the photo-crosslinks form, this estimate of the maximum attainable macroscopic sample averaged Young's modulus is an over estimate. As is displayed in the figure below, the model prediction corresponds well with the experimental data.

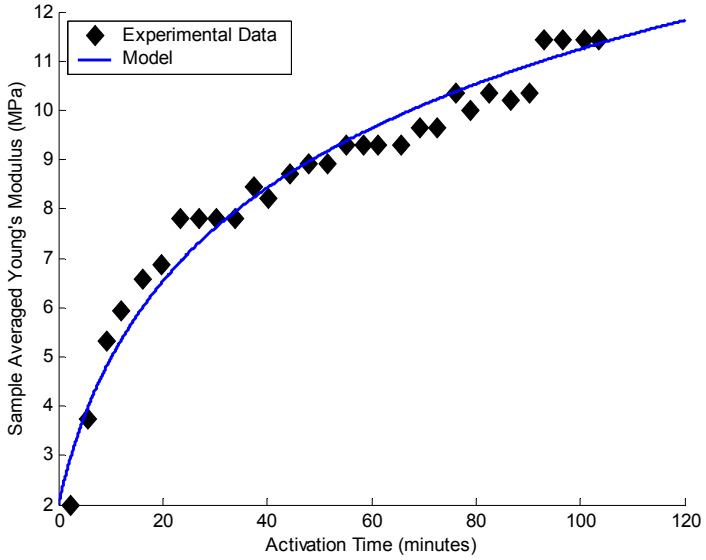

Figure 3.2-1: Model prediction as compared to experimental data for formula EAS-155-115

Having an experimentally calibrated model, it is instructive to analyze the through thickness time evolution of other parameters, such as the concentration of optically activated uncross-linked species, *S*, and the through thickness evolution of Young's modulus, *E*. Pictured

in Figure 3.2-2, before exposure to light, S is equal to 0 throughout the sample. After 1 minute of exposure, the amount of photo activated material forms a shape similar to that of the exponentially decaying transmitted optical power predicted by the Beer-Lambert Law, which is consistent with our assumptions in deriving the equation governing k_1 and k_2. As time progresses, the amount of photo activated species decreases as cross-linking occurs.

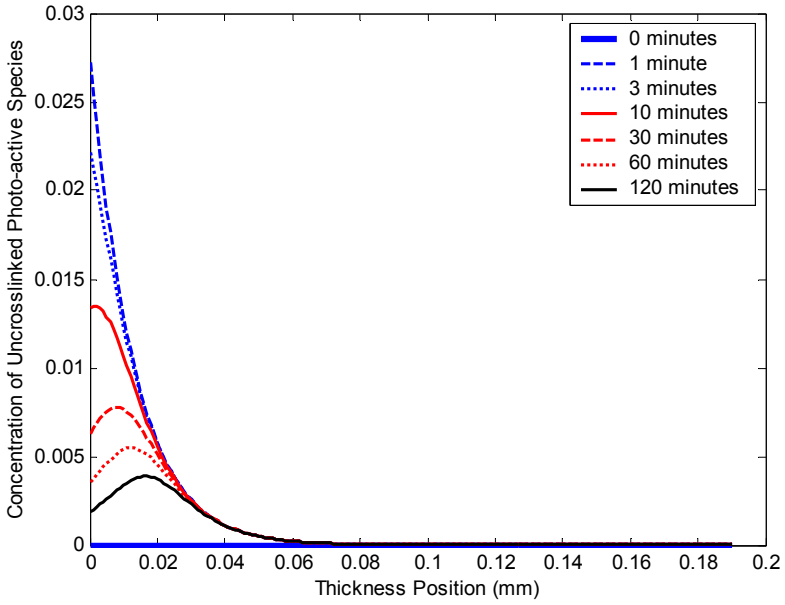

Figure 3.2-2: Predicted through thickness evolution of photo activated uncross-linked species for formula EAS-155-115

Figure 3.2-3 illustrates the through-thickness evolution of Young's modulus for various laser exposure times, as predicted by the presented model. The effect of the polymer's ability to transmit light, as expressed through the Beer-Lambert Law, is clearly evident in the through thickness distribution of Young's modulus. Such an observation leads to the realization that while the cross-linking kinetic characteristics play a significant role in the transition time of

LASMP, equally important is the ability of the polymer to transmit sufficient amounts of light to enable through-thickness cross-linking. For instance inspection of Figures 3.2-2 and 3.2-3 together illustrates that even in the absence of an increased rate of chemical kinetics, increased transmittance alone will result in deeper penetration of light at any given moment in time, and therefore a larger increase in volume averaged stiffness at that moment in time; the result being an increased rate of property change at the macroscopic level. Once the interplay between chemical kinetics and transmittance has been optimized for a given formulation family, creative light delivery strategies, such as optical fiber or particle doping, may be employed to further enhance the rate and depth of property transition in LASMP structural components.

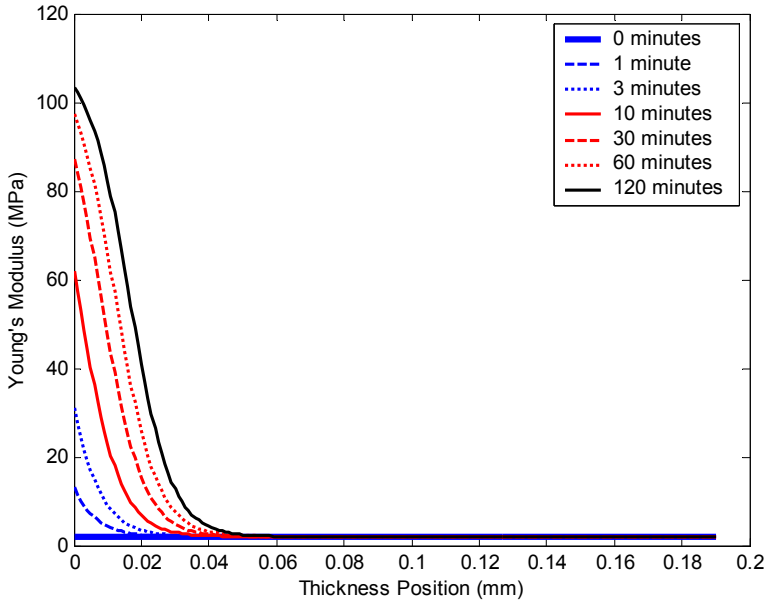

Figure 3.2-3: Predicted evolution of Young's modulus through sample thickness for formula EAS-155-115

Table 3.2-1: Chemical kinetic model parameters for formulas

	U_0 (%)	E_0 (MPa)	E_{max} (MPa)	τ	E_F (MPa)
EAS-155-93	2.4	5.0	850	18	106.7
EAS-155-115	3.0	2.0	110	8	11.4
EAS-155-143	3.3	1.13	NA	NA	NA

Table 3.2-1 above lists the known and phenomenologically fit model parameters for various LASMP formulas. U_0 is the initial concentration of photo active species based on the molecular formula of the polymer, E_0 is the experimentally determined soft state Young's modulus, E_{max} and τ are the phenomenologically determined maximum Young's modulus and time constant respectively, and E_F is the final sample averaged Young's modulus experimentally measured. As can be seen from Table 3.2-1, formula EAS-155-93 has a theoretical modulus much higher than formula EAS-155-115. This is expected since formula 93 also has a much higher experimentally determined modulus. It is interesting to note though, that formula EAS-155-115 has more crosslinkable material than formula EAS-155-93. This should translate into more crosslinks and thus a higher modulus. Other factors influencing crosslink formation such as chain mobility and entanglements, not directly accounted for in the model, could account for the unexpected result.

Figures 3.2-4 through 6 are the model results for formula EAS-155-93. As can be seen from Figure 3.2-4, the time evolution of the concentration of uncrosslinked photo-active species is similar to the distribution shown for formula EAS-155-115 in Figure 3.2-2. For formula 93, activation occurs up to a depth of approximately 0.02mm, which is consistent with formula EAS-155-115. As mentioned previously, the depth of penetration of the sample is consistent across all the tested samples but the thicknesses of each changes, requiring the development of a model such as the one presented effectively removing the geometry of the samples from reported results.

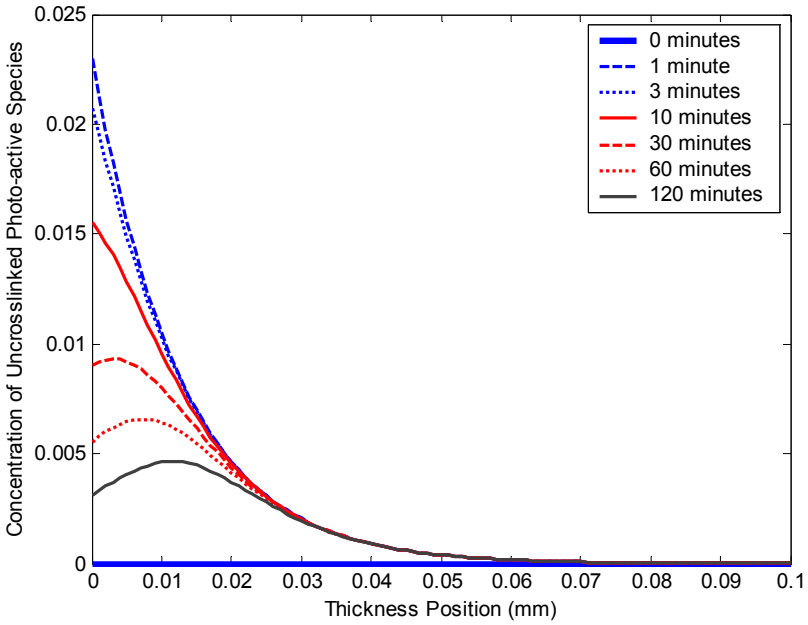

Figure 3.2-4: Predicted through thickness evolution of photo activated uncross-linked species for formula EAS-155-93

Figure 3.2-5, below, pictures the evolution of Young's modulus of formula EAS-155-93 as a function of activation time. Both formulas 115 and 93 show significant crosslink formation and thus increases in stiffness to a depth of 0.02mm (20μm), which is comparable to previous studies by Ikeda et al. achieving a depth of 1μm [33].

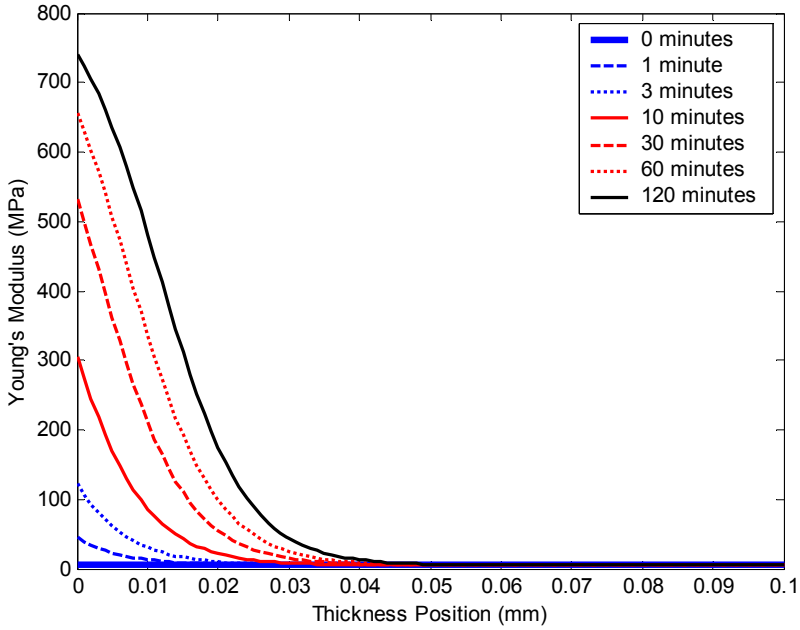

Figure 3.2-5: Predicted evolution of Young's modulus through sample thickness for formula EAS-155-93

In Figure 3.2-6 below, the time evolution of the sample averaged Young's modulus as predicted by the model is shown compared to the experimental values of two samples. An initial modulus of 5.0 MPa is used to model formula 93, and not the experimentally determined soft state modulus of 15.0 MPa, to allow the initial part of the modeled curve to match experimental data. As can be seen, the initial slope of the modeled and experimental data coincide well, as prescribed by E_{max} and τ in Table 3.2-1.

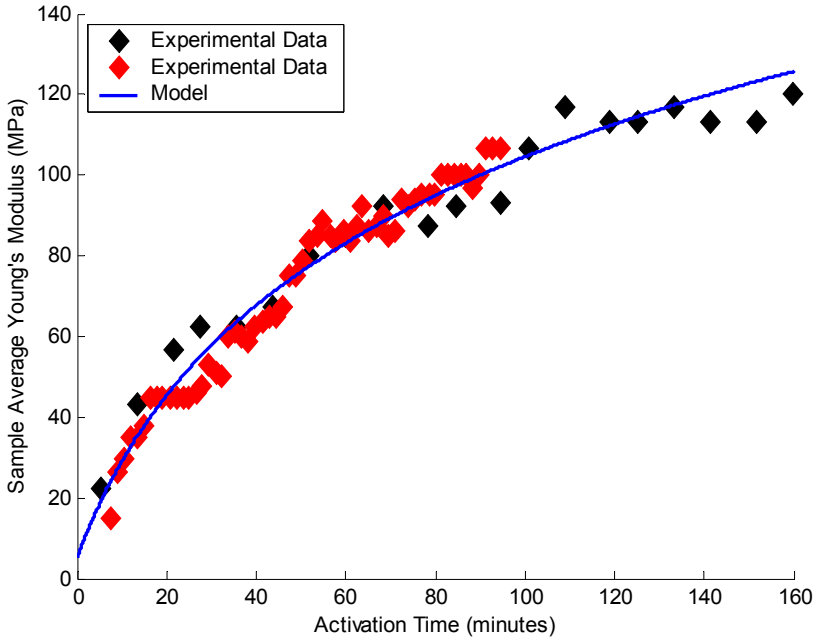

Figure 3.2-6: Model prediction as compared to experimental data for formula EAS-155-93

4.0 ROTATIONAL ISOMERIC STATE MODEL

Synthesis and experimental characterization of novel LASMP formulations require substantial investments in both time and resources. In order to minimize both the cost and lead time of LASMP development a model has been developed for predicting the macroscopic material characteristics of candidate formulas. Thus the model input parameters must be derivable from the molecular formula with minimal if any requirement of empirical parameters, while still generating reasonable predictions of both the soft state and stiff state Young's modulus of candidate formulas. Under these constraints precise predictions are of course an unreasonable expectation. However, the method should prove sufficient for identifying especially promising formulations (or conversely, ruling out ill-fated formulations). For this purpose a model is presented based on rotational isomeric state theory. A single experimental parameter, namely density, is required to assess a broad family of potential formulations; the approach otherwise requires only the proposed molecular formula. In addition to adhering to the aforementioned objectives, the approach has been developed to be modular in nature to expand adaptability to other formulation families.

As schematically illustrated in Figure 4.0-1, the progression of the model begins with the application of rotational isomeric state theory to simulate a model of a single polymer chain. This single chain necessarily includes crosslinked and photo-crosslinkable sites. Employing a Monte Carlo strategy this simulated chain can then be used to create a list of crosslink to crosslink

distances, or *r*-values. Employing Johnson distribution functions, this list of *r*-values is converted to a single probability density function describing the simulated polymer. The probability density function is adapted to the strategies of Boltzmann statistical mechanics per the three chain rule where the change in entropy due to strain of the polymer chain is used to estimate the Young's modulus of the polymer. Each of these steps, described in detail below in Sections 4.1 through 4.5, can be substituted for alternative methods, also described below. This modular system allows the model to be adapted and optimized for many different polymeric materials having drastically different characteristics than LASMP, making the presented model extremely useful for formula development and design across the field of materials and engineering.

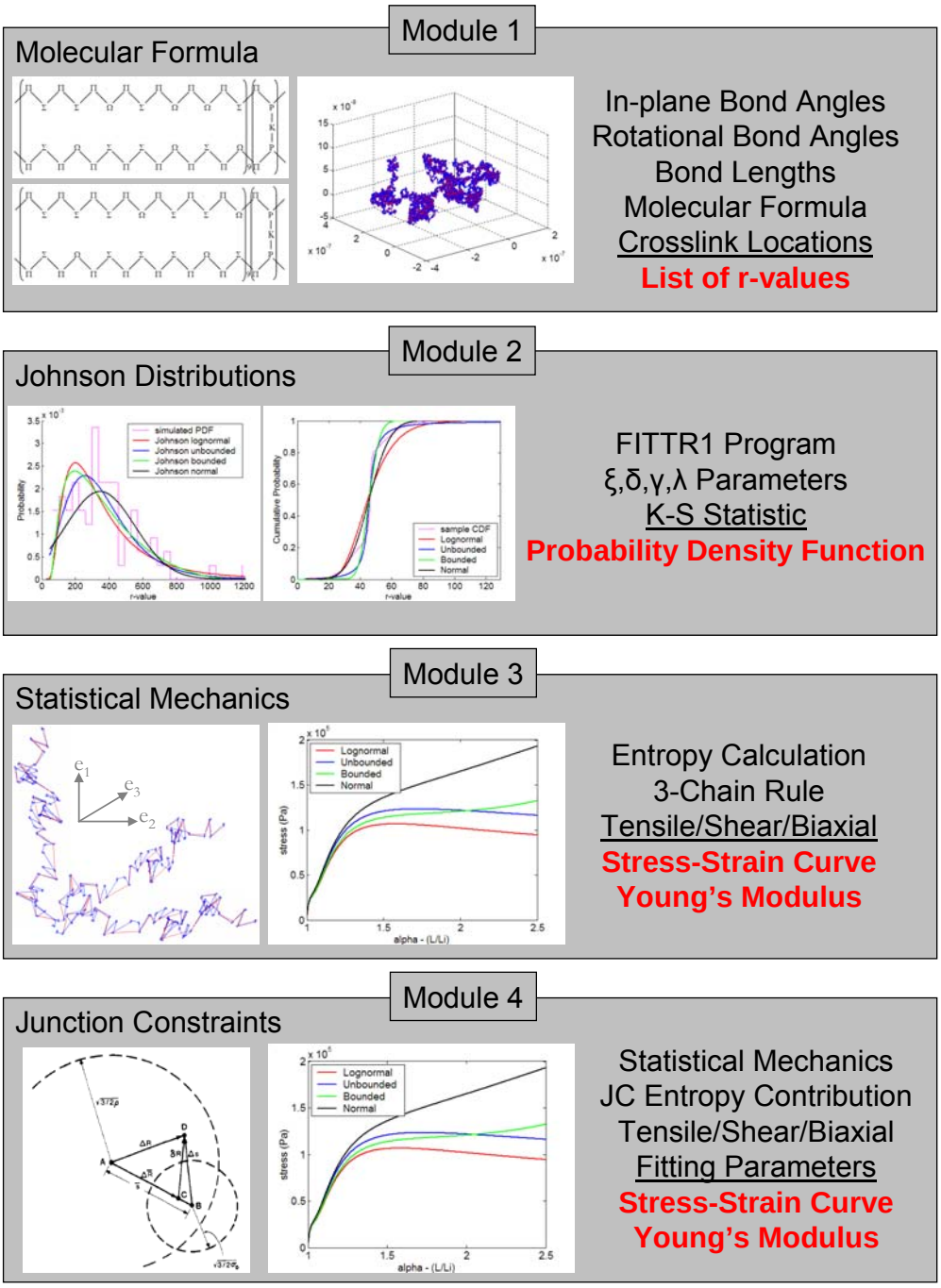

Figure 4.0-1: Schematic of model flow

4.1 ROTATIONAL ISOMERIC STATE THEORY

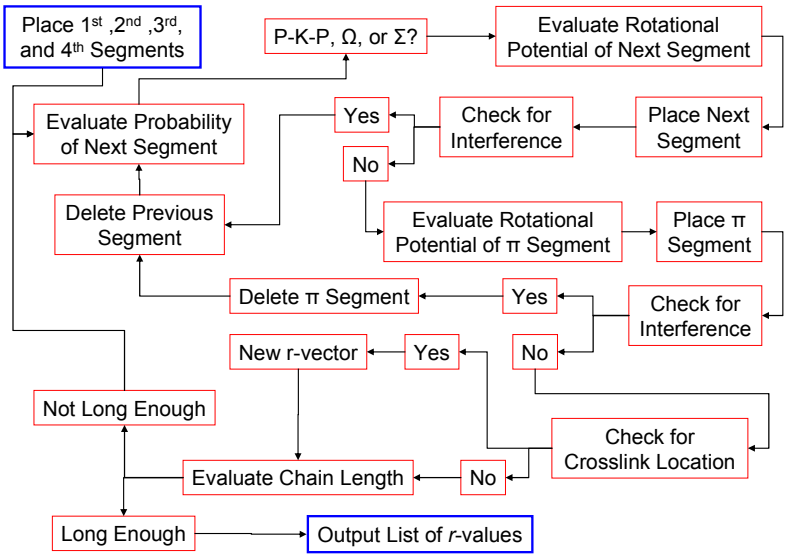

Figure 4.1-1: Module 1, diagram of flow for building a molecular chain

Rotational isomeric state (RIS) theory, developed by Flory in the 1960s and 70s, is used to build a molecular model of the polymer. Many advancements and studies have been conducted regarding RIS including the accurate molecular representations of many polymers including Poly(dimethylsiloxane), Poly(oxyethylene), and Vinyl Polymer Glass [149-151]. Presented is a brief synopsis of the most important aspects of the theory. More detailed discussions of the theory and applications can be found here [83-100,101-106]. RIS theory simply states that if the molecular formula of the polymer is known, such as that pictured below in Figure 4.1-2, the rotational state of any given bond is uniquely dependent on the rotational state of neighboring bonds.

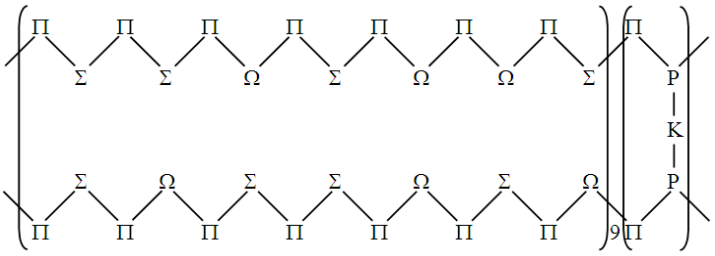

Figure 4.1-2: Example molecular formula

Figure 4.1-2 shows a typical molecular formula of the presented study. Individual atoms and molecules are grouped together into "segments" indicated by Π, Σ, Ω, P, and K. This practice is referred to as graining. It allows all of the pertinent information about the polymer chain to be shared between collaborating agencies without compromising the intellectual property of the polymer's designer. Graining is employed to (1) reduce the computational burden of the approach while also (2) masking the exact formulation details in accordance with manufacturer specifications. Thus the exact position and type of the atoms involved in creating a crosslink are not known within each molecular segment, but as will be demonstrated below this is inconsequential to model development and effectiveness.

While in-plane bond angles are directly calculated based on the molecular structure, θ in Figure 4.1-3, each rotational bond has a discrete number of angles corresponding to low energy configurations, φ in Figure 4.1-3. Bond potential versus rotational angle relationships are compiled using the software package HyperChem®, produced by HyperCube, Inc., an example of which is shown in Figure 4.1-4.

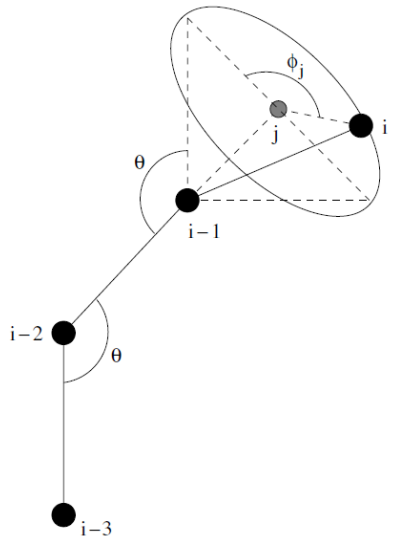

Figure 4.1-3: Bond angles used to build polymer chain [31]

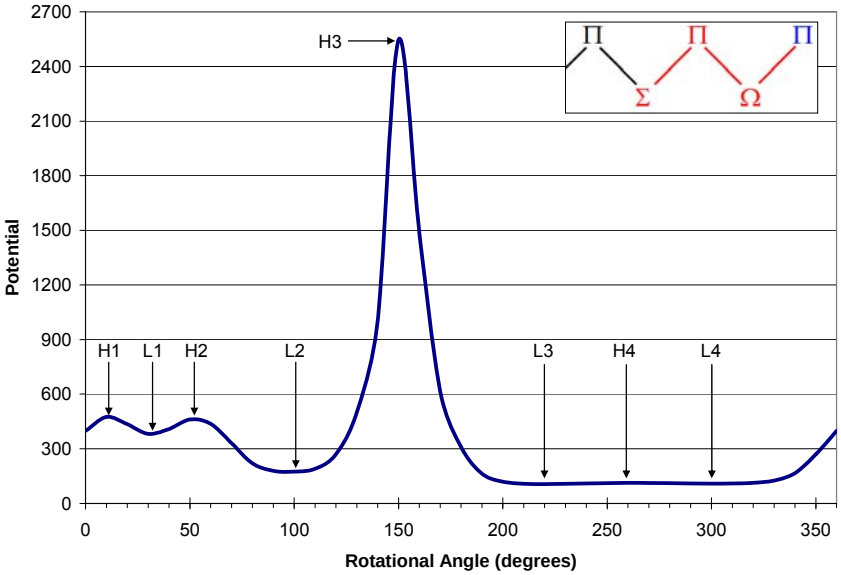

Figure 4.1-4: Example of the torsional potential of a bond

It is known that rotational bond angles can fluctuate by up to 20 degrees from the mathematical minima produced by HyperChem, but because the sign of the offset of such fluctuations are random and thus mutually compensatory, it is sufficient to model all rotational bond angles as if

they were in fact the angle of minimum potential. Not all rotational angles are clearly defined, however, as can be seen in Figure 4.1-4, and require additional arguments. In some cases, the potential is nearly constant over a range of rotational bond angles, such as between the angles of 200 to 325 in Figure 4.1-4. Although there are mathematical minima at 220° and 300° (L3 and L4), the energy barrier associated with the rotation of such bonds is very low. It can be argued; however, that RIS theory still holds for cases where the barriers to rotation are negligible, arguing a similar case as above in that the random offsets, while more common, remain mutually compensatory. It is possible to argue, however, that because the energy barriers for certain angles are not symmetrical that the distribution of resulting fluctuations will be skewed toward the lower barrier. This is acknowledged, however assumed to have little effect on the resulting *r*-value prediction and thus ignored during the presented study.

Once the low energy rotational bond angles have been identified, a statistical weight matrix must be developed to project the probability of occurrence for each angle. To calculate the statistical weights of the rotational angles the peak to peak potential distances are used. When any given molecule or atom is added to the polymer chain, RIS theory postulates that it approaches the chain from a random angle. The bonding molecule then rotates in the direction of decreasing bond potential until at the minimum bond potential angle. The fraction of available angles between two consecutive peaks of the potential curve relative to a full rotation (360 degrees), then, represents the probability of occurrence of the included minimum energy angle.

Since it can be argued that the instantaneous intramolecular environment of a molecule or bond in the liquid state is exactly described by the potentials described above by citing that all motion in the liquid state is random and relatively free, it is reasonable to argue that the potentials also describe those molecules in the cured state, negating any perturbations due to

intermolecular packing, again citing the compensatory argument. Simply stated, any and all effects having influence over the rotational bond angles are ignored since it can be argued that all effects are random and thus offset from a modeling standpoint.

During construction of the chain, lists of inherent (permanent) crosslink locations and possible photo-crosslinkable locations are compiled. Since the molecular structure of the polymer is known, it is also known if each segment placed during construction has the ability to crosslink. For the presented study, the P-K-P chain segment in Figure 4.1-2 represents an inherent crosslink in the polymer while the Ω segments represent photo-crosslinkable locations. These lists of crosslink locations are then used to compile a list of crosslink to crosslink distances, or the straight line distance between two crosslink locations, used by the statistical mechanics portion of the model. Figure 4.1-5 shows a graphical representation of the definition of an *r*-value, where the red locations denote inherent crosslink sites in the polymer and the blue locations denote photo-crosslinkable sites along the polymer chain backbone. For the purpose of the presented model, it is assumed that all photo-crosslinkable sites have crosslinked in the hard state and there are no photo-crosslinked sites in the soft state. Although this is highly unlikely, a more detailed study of the nature of the photo-crosslinks is needed to more accurately characterize this property, which is beyond the scope of the presented work.

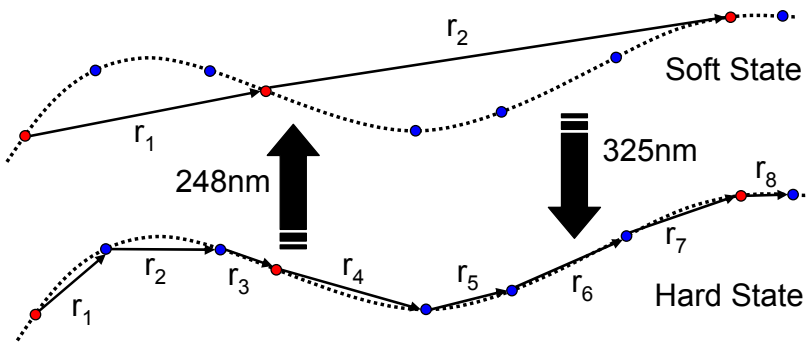

Figure 4.1-5: Schematic of *r*-value definition

The above described RIS model for constructing a single LASMP chain, while having been shown to reflect the qualities of the actual polymer chain, is not without limits. As mentioned previously, the rotational bond angles can fluctuate by as much as 20 degrees. Typically the fluctuations are mutually offsetting, however there are exceptions to this rule arising primarily from environmental factors such as temperature and pressure. For temperatures and pressures far from ambient, the response of the polymer may differ from that predicted by the model. The bonds having wide potential wells approximate those polymers having freely rotating bonds and, under some circumstances, since they are modeled here as fixed can lead to higher than actual stiffness predictions at low strains, causing the predicted stress-strain curve to be offset from those attained experimentally. Despite known inaccuracies, the above detailed RIS method of simulating a single polymer chain effectively produces a relatively accurate representation of the polymer and results in a list of crosslink to crosslink distances, or *r*-values, used subsequently in the presented model.

4.2 JOHNSON DISTRIBUTIONS

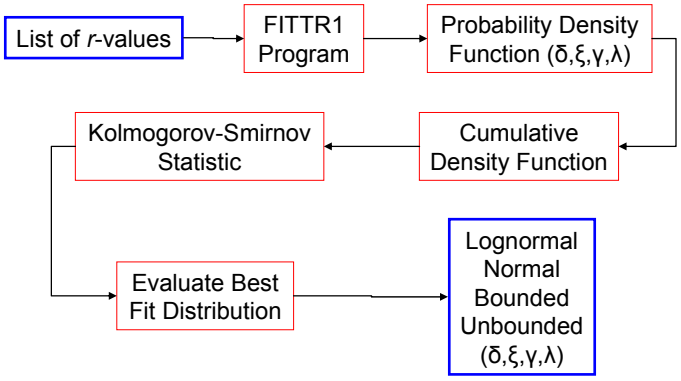

Figure 4.2-1: Module 2, diagram of flow for evaluating best fit probability density function

In calculating the entropy of the modeled polymer chain, discussed in detail later, a probability density function describing the distribution of distances between crosslinks is needed. It is this distribution of *r*-values that differentiates the polymer formulas. When the polymer is in the hard state, the distribution has tighter bounds and the mean is lower than when the polymer is in the soft state. Differences in the PDF then correspond to differences in the calculated change in entropy with respect to strain, discussed subsequently in Section 4.4. For this, Johnson distributions are used, consisting of four families including lognormal, unbounded, bounded, and normal covering a wide variety of distribution profiles. Detailed derivations and examples of implementation of Johnson distributions have previously been published, showing that they are ideally suited for modeling the distribution of *r*-values in material systems with high crosslink density [31,102-104,107,108], such as LASMP. To estimate an unknown density *P(x)*, Johnson transforms the random variable *X* into a standard normal random variable *Z*.

$$Z = \gamma + \delta f\left(\frac{X-\xi}{\lambda}\right) \tag{4.2-1}$$

where γ and δ are shape parameters, λ is a scale parameter, and ξ is a location parameter. The function f is family specific.

$$f(y) = \begin{cases} \ln(y) & \textit{Lognormal} \\ \ln\left(y + \sqrt{y^2+1}\right) & \textit{Unbounded} \\ \ln\left(\dfrac{y}{1-y}\right) & \textit{Bounded} \\ y & \textit{Normal} \end{cases} \tag{4.2-2}$$

Equation 4.2-3 below is then the corresponding probability density function (PDF) and the governing equation for all Johnson distributions.

$$P(x) = \frac{\delta}{\lambda\sqrt{2\pi}} f'\left(\frac{x-\xi}{\lambda}\right) \exp\left[-\frac{1}{2}\left(\gamma + \delta \bullet f\left(\frac{x-\xi}{\lambda}\right)\right)^2\right] \tag{4.2-3}$$

Here, $P(x)$ is the probability distribution of the analyzed data, x is the dependent variable (in our case the distance between crosslinks), δ, λ, ξ, and γ are fitted variables, the function f is family specific defined by Equation 4.2-2, and f' is the first derivative of f

$$f'(y) = \frac{\partial f(y)}{\partial y} = \begin{cases} \dfrac{1}{y} & \textit{Lognormal} \\ \dfrac{1}{\sqrt{y^2+1}} & \textit{Unbounded} \\ \dfrac{1}{y(1-y)} & \textit{Bounded} \\ 1 & \textit{Normal} \end{cases} \tag{4.2-4}$$

The closed support of Equation 4.2-3 is defined as:

$$H = \begin{cases} [\xi, +\infty) & \textit{Lognormal} \\ (-\infty, +\infty) & \textit{Unbounded} \\ [\xi, \xi+\lambda] & \textit{Bounded} \\ (-\infty, +\infty) & \textit{Normal} \end{cases} \tag{4.2-5}$$

Fitting of the distributions to the modeled data is achieved through the software package FITTR1, developed by James Wilson and readily downloadable [107,109]. Utilization of a standardized method, such as FITTR1, removes some of the human error associated with curve fitting and increases success of similar results being obtained by many different researchers. FITTR1, given a list of the *r*-values, is capable of fitting the data to any chosen Johnson distribution using moment matching, percentile matching, ordinary least squares, diagonally weighted least squares, L_1-norm and L_∞-norm estimations, weighted least squares, and L_1-norm (BWS) estimations. An example probability density function created by the FITTR1 program is shown below in Figure 4.2-2.

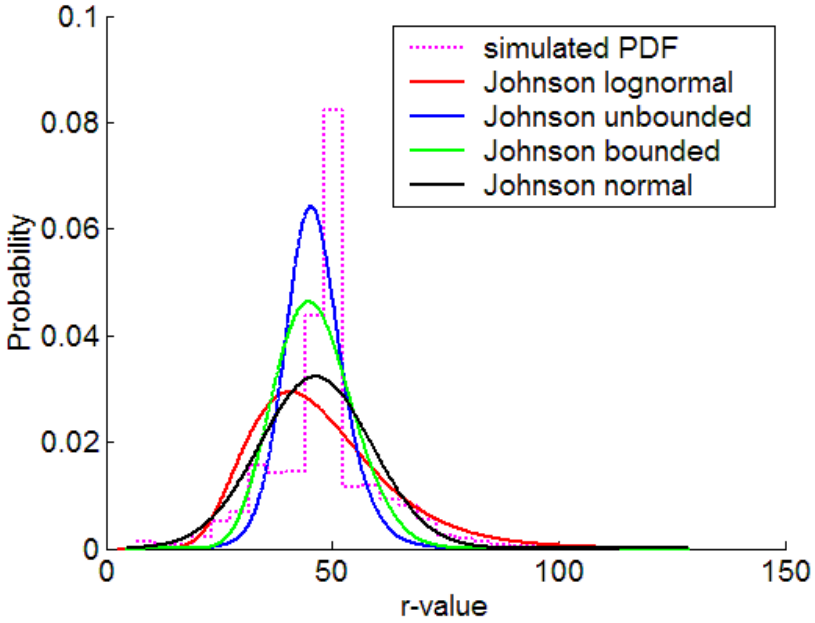

Figure 4.2-2: Example PDF created by FITTR1 program

As with all distributions, however, Johnson distributions and the FITTR1 program have limitations. Johnson distributions are not capable of modeling bimodal data, although not seen in current LASMP formulations, which may be encountered in the future when modeling other polymers. Johnson distributions also have difficulty modeling increasingly narrow distributions, resulting in the distribution approaching an impulse function, which is possible with heavily crosslinked polymer systems.

Alternatives to Johnson distributions include Gaussian, Bezier, and inverse distribution functions. Gaussian distributions [110] are known to have increasingly large errors at large strains, making them less desirable for the current application. Bezier distributions [111], although accurate, are more complex than Johnson distributions resulting in more complex and elaborate computer code for implementation. Similarly Inverse distribution functions [112] are more accurate but also more complex. Although Johnson distributions have limited flexibility due to the discrete number of fitting parameters, they are computationally simple to implement

and have been shown to accurately capture the form of the probability density function describing the distance between crosslinks for polymer systems [31]. Moreover, Johnson distribution parameters are well defined; thus unlike the other fitting methods the Johnson distribution parameters are insensitive to user-defined bins.

The use of distributions in general to model the simulated *r*-values and the subsequent use of Boltzmann statistical mechanics calculating a change in entropy as a function of stretch limits the overall method to quasi-static predictions. Atomic forces such as Van der Waals are neglected, thus modeling any rate dependent material characteristics becomes impossible. An alternative method that includes such functionality is presented in Chapter 8. The current presented method, however, is much less computationally and time intensive, which is the original objective of the project of decreasing the time required to evaluate candidate LASMP formulas.

4.3 KOLMOGOROV-SMIRNOV STATISTIC

Only one PDF for each conformation is required to predict the material response using the statistical mechanics method outlined below in Section 4.4. Since there are many possible PDFs, 4 families each with 8 fitting methods resulting in 32 possible PDFs, a consistent evaluation method is needed. The distribution of *r*-values is represented most accurately by a histogram. Histograms, however, are notoriously inconsistent when visually curve fitting. The size of the bins can have a significant impact on the interpretation of the displayed data. With relatively small bins, unrealistic peaks and valleys may be displayed due mostly to an insufficient number of data points in each bin or as a result of the randomness inherent in the

Monte Carlo simulation method. Conversely, bins that are too large have the opposite effect of masking trends, resulting in an overly smooth representation. To compare the PDFs, the Kolmogorov-Smirnov (KS) statistic is used to reduce the error associated with both human intuition and histogram presentations.

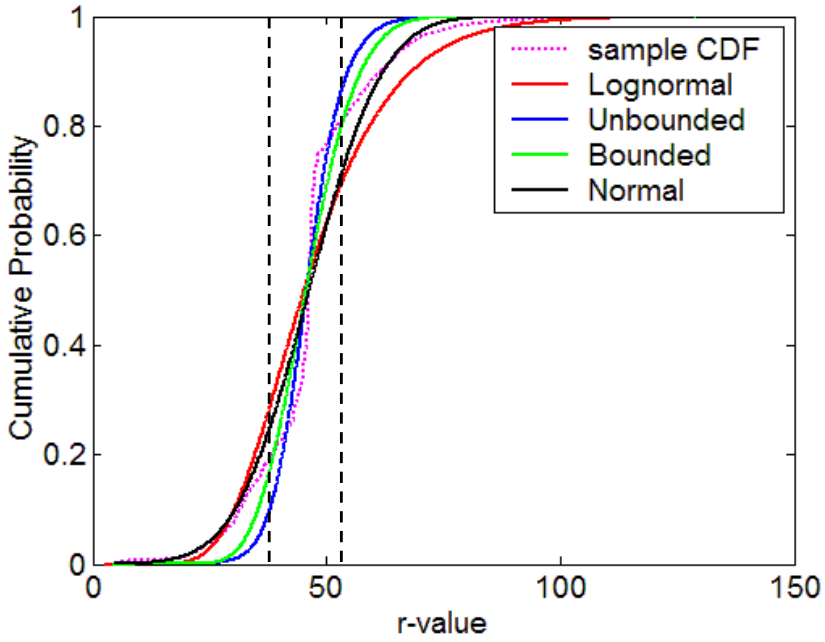

Figure 4.3-1: Example cumulative distribution function in the hard state

The KS statistic is the maximum difference between the simulated cumulative distribution function (CDF) of *r*-values, shown in Figure 4.3-1, and the CDF of the Johnson distribution modeling them [31,113]. CDFs are created by evaluating the number of data points of equal or lesser value for each successive data point, eliminating the use and misleading aspects of the bins used in histograms. The KS statistic can loosely be thought of as the maximum error associated with the corresponding PDF. When the polymer is in the hard state, the *r*-values typically range between 0 and 150Å, while in the soft state they can range from 0 up

to 1200Å resulting in vastly different CDFs. In the hard state, due to the more regularly dispersed crosslinks and thus small range of *r*-values, the PDF can approach a sharp peak causing the CDF to approach a step function. Such a distribution is exceptionally hard to model while maintaining flexibility. This also, however, exemplifies how KS statistics can be used to remove human error from evaluating a distribution. When discussing the goodness of fit, it is pertinent to divide the distribution into three sections, delineated in Figure 4.3-1 by the vertical dashed lines. The lower section is comprised of *r*-values less than 30Å, the middle being those between 30-55Å, and the upper section containing the *r*-values higher than 55Å. The middle section is defined as the part of the curve that is relatively linear. In the hard state, the vertical nature of the middle section is modeled relatively well considering the difficulty in modeling the distribution and the desire to maintain flexibility in the fitting method. The lower and upper sections are modeled slightly less accurately; in this thesis however this is considered acceptable since the bulk of the *r*-values, approximately 80%, are contained in the middle section, see Figure 4.3-1.

When in the soft case, the distribution of *r*-values is more dispersed and thus easier to model. Sections of the CDF in the soft state range from below approximately 50Å, between 50 and 400Å, and above 400Å, see Figure 4.3-2. The middle section typically contains 70% of the *r*-values and is modeled extremely well, unsurprising since Johnson distributions are known to model skewed data. The upper and lower sections in the soft state are also modeled relatively well considering the increasingly smaller sample sizes nearing the limits of the distribution.

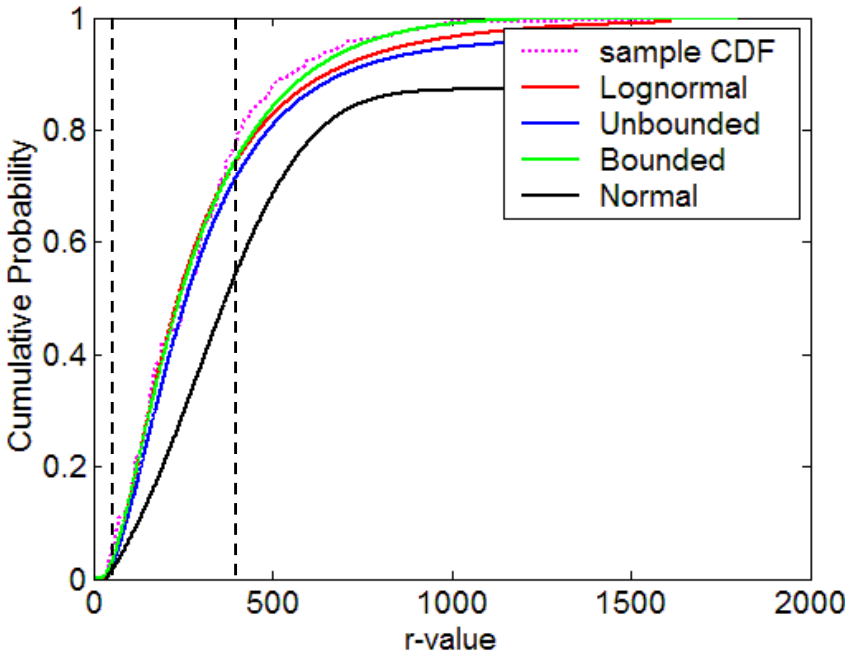

Figure 4.3-2: Example cumulative distribution function in the soft state

Another characteristic of the CDF taken into consideration when choosing the best fit distribution is the upper and lower limits of the graph. Theoretically there is no upper limit to the distance between two crosslinks, although the probability approaches zero. The lower limit, however, is dictated by the molecular formula and is between 5.3 and 12.1Å. The inability to report an exact minimum distance is due to the graining of the molecular formula, discussed previously. As illustrated in Figures 4.3-1 and 4.3-2, the CDFs in both the hard and soft states approach zero before this lower limit, which is consistent with expectations of a real polymer chain. When choosing the preferred distribution and fitting method, the KS statistic as well as a qualitative analysis of the fit of the lower and upper regions of the CDF curve are taken into account.

While the KS statistic provides an accurate way to evaluate the goodness of fit of any distribution while reducing the impact of human error, there are alternatives. The Chi-squared

statistic, also calculated by the FITTR1 program, can also be used to evaluate the goodness of fit, however it is arguably a less accurate method [31,113].

4.4 STATISTICAL MECHANICS

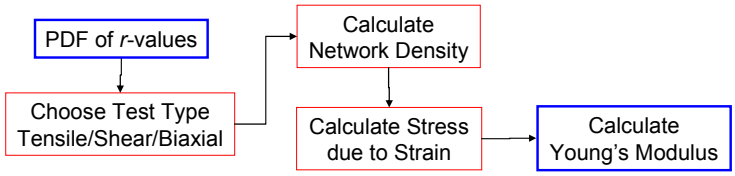

Figure 4.4-1: Module 3, diagram of flow for statistical mechanics model

The entropy of the polymer chain is related to the probability density function of *r*-values by [31,91,93,106,110]

$$S(r) = c + k \ln[P(r)] \tag{4.4-1}$$

where *S* represents entropy, *c* is a constant of integration, *k* is Boltzmann's constant, and *P(r)* is the probability density function produced per the methods of the previous section. If the rotation of any individual bond is considered unrestricted, Helmholz free energy is strictly a function of entropy. Although this assumption of elasticity is increasingly invalid for stiffening (glassy) polymers, relative predictions of several polymer formulations require a single theory be used for all polymer states. Also, as will be shown later, the error associated with this assumption can be mitigated by the flexibility of including the stress response due to junction constraints. The three chain model, which assumes that each represented *r*-value can be decomposed into three

equivalent chains aligned with each of the Cartesian axes, is then used to describe the change in entropy as a function of strain [31,110]

$$\Delta S = \frac{\upsilon}{3}\left[S(r_1) + S(r_2) + S(r_3) - 3S(r_0)\right] \tag{4.4-2}$$

where v is the number density of network chains, r is test specific and is a function of r_0 and α, r_0 is the root-mean-square of the distance between crosslinks (r-values), α is the relative length of the sample (L/L_0) in each of the coordinate directions, L is the current length of the sample, and L_0 is the original length of the sample [31,110]. Inside the square brackets in Equation 4.4-2, the first three terms are associated with the change in entropy with respect to strain in the three coordinate directions and the last term the entropy of the reference state of the polymer. By decomposing Equation 4.4-2 into its respective parts the theory can be used to study the strain induced anisotropic properties of the polymer [55]. The number density of network chains is then given by [110].

$$\nu = \frac{\rho N_A}{M_P} = \frac{\rho R}{k M_P} \tag{4.4-3}$$

where ρ is the density of the polymer, N_A is Avogadro's number, M_P is the molecular weight of the polymer chain, and R is the gas constant. It is this density that is the only macroscopic property needed to study the phantom polymer network. From rubber elasticity, the nominal stress can then be calculated using [31]

$$f^* = -T\left(\frac{\partial \Delta S}{\partial \alpha}\right)_T = -\frac{\upsilon k T r_0}{3}\left[C_1 G'(r_1) + C_2 G'(r_2) + C_3 G'(r_3)\right] \tag{4.4-4}$$

where T is absolute temperature. Equation 4.4-4 assumes that all strain is affine, and is the basis for which deformation is imparted on the system since the PDF, *P(r)* in Equation 4.4-1, describing the list of generated *r*-values is a function of stretch, α, as defined in Table 4.4-1. Visually this can be thought of as stretching the distribution, thus altering its shape and derivative, changing the calculated entropy of the system. The remaining quantities in Equation 4.4-4 are

$$G(r) = \ln\left[P(r)\right] \tag{4.4-5}$$

$$G'(r) = \frac{\partial G(r)}{\partial \alpha} = \frac{f''\left(\frac{r-\xi}{\lambda}\right) - \delta\left[f'\left(\frac{r-\xi}{\lambda}\right)\right]^2\left[\gamma + \delta f\left(\frac{r-\xi}{\lambda}\right)\right]}{\lambda f'\left(\frac{r-\xi}{\lambda}\right)} \tag{4.4-6}$$

$$f''(y) = \frac{\partial^2 f(y)}{\partial y^2} = \begin{cases} \dfrac{-1}{y^2} & \textit{Lognormal} \\ \dfrac{-y}{\left(y^2+1\right)^{3/2}} & \textit{Unbounded} \\ \dfrac{-(1-2y)}{\left[y(1-y)\right]^2} & \textit{Bounded} \\ 0 & \textit{Normal} \end{cases} \tag{4.4-7}$$

The quantities C_1, C_2, C_3, r_1, r_2, and r_3 are test specific. For modeling simple tension, simple shear, and equi-biaxial strain they have the values:

Table 4.4-1: Test specific C and r quantities

	Simple Tension	Simple Shear	Equi-biaxial
C_1	r_0	r_0	$-\frac{2r_0}{\alpha^3}$
C_2	$-\frac{r_0}{2\alpha^{3/2}}$	0	r_0
C_3	$-\frac{r_0}{2\alpha^{3/2}}$	$-\frac{r_0}{\alpha^2}$	r_0
r_1	$r_0\alpha$	$r_0\alpha$	$r_0\alpha^{-2}$
r_2	$r_0\alpha^{-1/2}$	r_0	$r_0\alpha$
r_3	$r_0\alpha^{-1/2}$	$r_0\alpha^{-1}$	$r_0\alpha$

The corresponding modulus is then calculated by [31,97]

$$\left[f^*\right]=\frac{f^*}{\alpha-\alpha^{-2}} \tag{4.4-8}$$

The modulus in Equation 4.4-8 approaches Young's modulus as α approaches 1 and is the basis by which the modeled polymer formulations are compared. While the assumption that the polymer is elastic and subsequent use of Equation 4.4-4 is strictly not true in all cases, the results given by the theory are consistent with experiment, as will be discussed later. The modular nature of the model does, however, allow for the substitution of Equation 4.4-4 by alternative theories, such as those presented below.

While the three chain model of Equation 4.4-2 provides a relatively accurate and easily implemented method for calculating the change in entropy with respect to strain, alternative and arguably more accurate, models have been proposed. For instance the four

chain, or tetrahedral, model developed by Flory and Rehner, also based on Gaussian fluctuations, models a single junction as having four contributing components radiating outward from the central point of interest. One of the major drawbacks of this theory is that it is inherently non-isotropic. To correct this, the inverse Langevin series approximation was introduced, which is similar to the three chain rule but with increased accuracy by including higher order terms when calculating the probability density [106,110]. Also, an eight chain model, developed by Arruda and Boyce [114], having eight components radiating outward from the center point of a cube to the eight corners has been shown to be accurate at high strain as well as alternative strain states such as equi-biaxial and shear strain. Although the model is slightly more accurate than the three chain model, it is significantly more complex, and thus is reserved for applications requiring a higher level of accuracy than the presented effort.

5.0 RIS THEORY MODEL RESULTS

5.1 LASMP MODEL DATA

5.1.1 Formula EAS-155-115 Model Data

The three molecular formulas modeled in the current study are EAS-155-93, EAS-155-115, and EAS-155-143. Since the actual molecular formula is proprietary to Cornerstone Research Group, Inc. (CRG), a grained molecular formula, still capturing the qualities of the polymer is used. This grained structure for formula 115 is shown below in Figure 5.1.1-1.

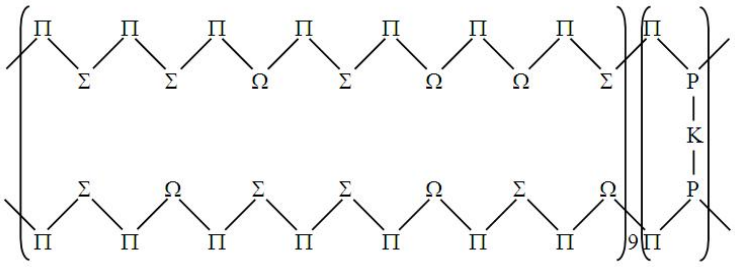

Figure 5.1.1-1: Molecular formula of LASMP formula EAS-155-115

where *Π*, *Ω*, *Σ*, *P*, and *K* represent given repeating groupings of molecules. The critical quantity produced by the RIS model is the distances between inherent crosslink sites along the polymer backbone, represented by the *P-K-P* segments, and the distances between photo crosslinkable

sites, represented by Ω segments in Figure 5.1.1-1. Since every individual atom is not required to obtain the necessary *r*-values, the above grained structure maintains the proprietary properties of the polymer while also allowing accurate modeling with the presented methods. Also supplied by the manufacturer, the bond lengths between each segment are known to be 1.54 Å and the in plane angle 111°. The molecular weights of each segment are listed below in Table 5.1.1-1.

Table 5.1.1-1: Molecular weights of LASMP polymer grained segments

Segment Symbol	Molecular Weight (Daltons)
Π	14.02658
Σ	13.01864
P	174.1785
K	142.1956
Ω	274.2687

The program HyperChem® has been used to produce a graph of potential versus rotational angle, such as those pictured below in Figures 5.1.1-2 through 5.1.1-4, for each possible order of segments. The figures below include the segment order with the red segments being those that have already been placed and a blue segment which is about to be added to the simulated polymer chain.

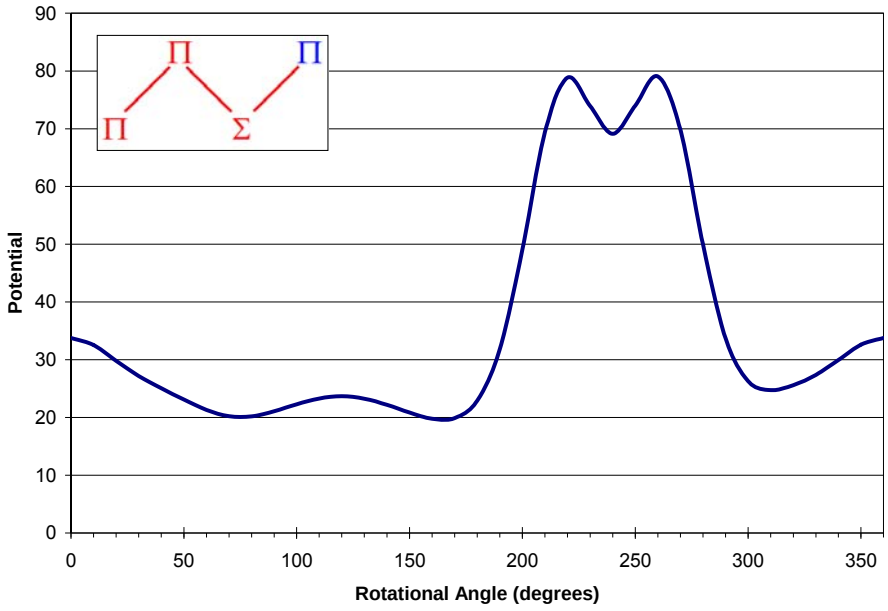

Figure 5.1.1-2: Torsional potential placing a Π segment after a Π-Π-Σ segment sequence

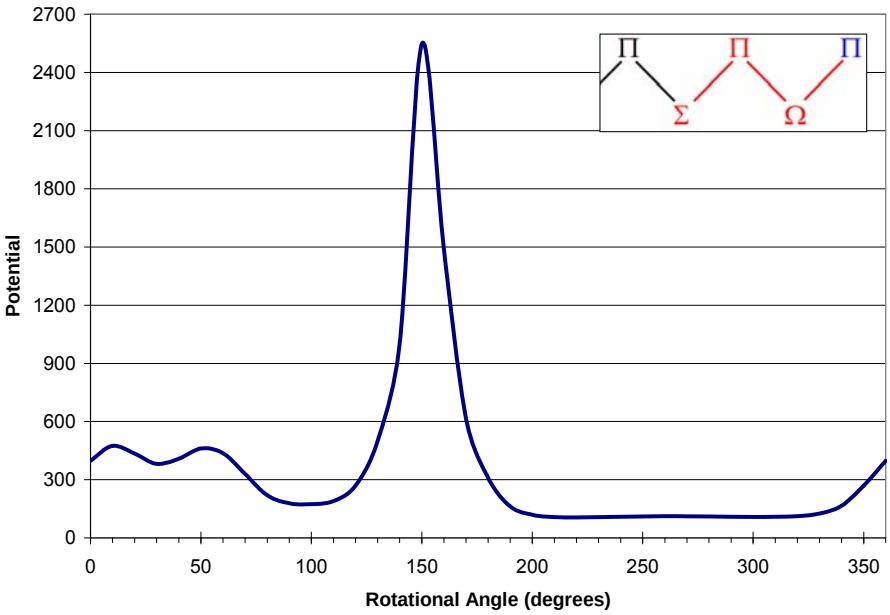

Figure 5.1.1-3: Torsional potential placing a Π segment after a Σ-Π-Ω segment sequence

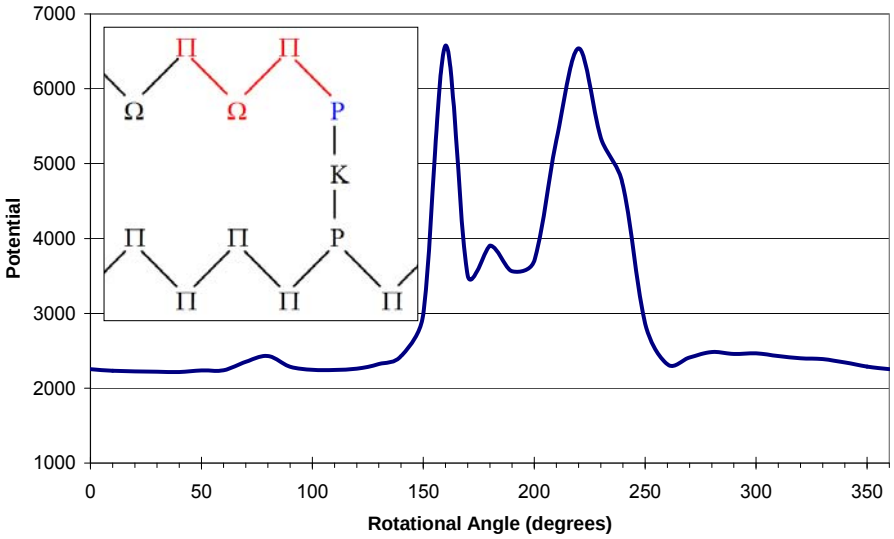

Figure 5.1.1-4: Torsional potential placing a P segment after a Π-Ω-Π segment sequence

All three of the examples pictured above have areas of both well defined angular positions with large energy barriers, such as 240° in Figure 5.1.1-2, 100° in Figure 5.1.1-3, and 172° in Figure 5.1.1-4, as well as areas of negligible barriers to rotation such as 75° in Figure 5.1.1-2, 220° in Figure 5.1.1-3, and 40° in Figure 5.1.1-4. Figures 5.1.1-2 through 5.1.1-4 are then used to calculate the low energy angles and their respective probabilities as outlined previously in Section 4.1. Table 5.1.1-2 lists the range and low energy angles of each possible configuration.

Table 5.1.1-2: Low energy angles and associated angular range of each segment configuration

Segment Sequence	Energy Minimum degrees	Range Minimum degrees	Range Maximum degrees
Π-Π-Σ-Π (chain end)	75	0	119
	164	120	220
	240	221	259
	310	260	359
Π-Σ-Π-Σ	220	41	285
Π-Ω-Π-Σ	305	286	325
Π-P-Π-Σ	350	326	40
Ω-Π-Σ-Π	188	71	218
Σ-Π-Σ-Π	250	219	308
	329	309	349
P-Π-Σ-Π	30	350	70
Π-Σ-Π-Ω	116	97	167
Π-Ω-Π-Ω	228	168	271
	305	272	329
Π-P-Π-Ω	40	330	96
Σ-Π-Ω-Π	32	12	54
	100	55	150
	220	151	260
	300	261	11
Ω-Π-Ω-Π	85	40	110
	139	111	152
P-Π-Ω-Π	300	153	260
	220	261	39
Π-Ω-Π-P	110	80	159
Π-Σ-Π-P	172	160	180
Π-P-Π-P			
Ω-Π-P-Π	195	181	220
Σ-Π-P-Π	40	221	79
P-Π-P-Π			

With the in-plane angles, all possible rotational angles and associated probabilities, and bond lengths known, it is left to estimate the physical length of each of the segments. Since the molecular weight of each segment is known the network density of a chain can be calculated by Equation 4.4-3 using a material density measured from experimental samples. The inverse of the network density is then the volume of a single simulated polymer chain. In the extreme

elongated case where the chain approximates a cylinder, a radius equal to the radius of a sphere with a volume the size of the smallest segment, Π, is used to calculate the overall length of the simulated polymer chain. This overall length is then used to calculate the lengths of each individual segment based on their molecular weights and the total molecular weight of the chain, listed below in Table 5.1.1-3. Although this method results in chain segment length estimations longer than expected in a real conformation, due to coiling, it does not inhibit the overreaching goal of the model of accurately comparing different formulations.

Table 5.1.1-3: Simulated polymer segment lengths

Segment Symbol	Segment Length (nm)
Π	0.2232
Ω	4.3643
Σ	2.2627
P	0.2072
Chain Radius	0.1677
Bond Length	0.1540

Knowing the in plane bond angles, rotational bond angles, bond lengths, molecular formula, and segment lengths, it is possible to build a simulated polymer chain using RIS theory. Rotational bond angles and segment order, where applicable, is determined through random number generation resulting in a slightly different polymer chain conformation each time the program is executed.

5.1.2 Formula EAS-155-93 Model Data

The grained molecular formula for sample EAS-155-93 is pictured below in Figure 5.1.2-1, having two photo-crosslinkable segments in the repeating pattern versus three for formula EAS-155-115.

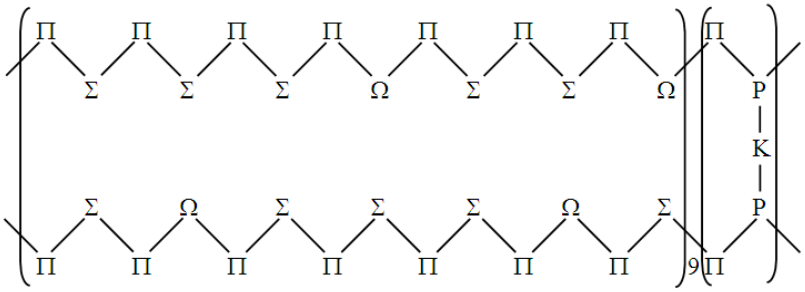

Figure 5.1.2-1: Molecular formula of LASMP formula EAS-155-93

The bond lengths between each segment and in plane angles are the same as the previous formula of 1.54 Å and 111° respectively. The molecular weights and modeled physical length of each segment are also the same as those listed in Tables 5.1.1-1 and 5.1.1-3 with the exception of the segment represented by Σ, listed below in Table 5.1.2-1.

Table 5.1.2-1: Molecular weights of LASMP polymer grained segments

Segment Symbol	Molecular Weight (Daltons)	Segment Length (nm)
Σ	118.1742	2.0103
Π	14.02658	0.2232
P	174.1785	0.2072
K	142.1956	NA
Ω	274.2687	4.3643

The rotational bond potentials and angle probabilities also remain identical to those listed in Table 5.1.1-2.

5.1.3 Formula EAS-155-143 Model Data

Pictured below in Figure 5.1.3-1 is the grained molecular structure of formula EAS-155-143. With every 4th segment containing photo-crosslinkable material of 124 segments between inherent crosslinks, as compared to every 4.7th of 126 segments for formula EAS-155-115 and every 7th of 126 segments for formula EAS-155-93, of the three modeled formulas presented it has the highest crosslink density in both the hard and soft states.

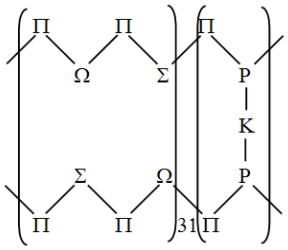

Figure 5.1.3-1: Molecular formula of LASMP formula EAS-155-143

The bond lengths between each segment, in plane angles, rotational bond potentials, and angle probabilities are the same as formula EAS-155-115. The molecular weights and modeled physical length of each segment are also the same as formula EAS-155-115, listed in Tables 5.1.1-1 and 5.1.1-3.

5.1.4 Conformation Build Statistics

Ten polymer conformations are generated for each of the three modeled formulas. Because the FITTR1 program used to fit the Johnson distributions to the data has a limit of 10,000 input values, the lengths of each formula conformation is adjusted so that each conformation of each of

the three formulas has approximately, but no more than, 10,000 *r*-values in the hard state. To save computing time, soft state predictions are limited to approximately 2,000 *r*-values. When the 10 conformations in each state are averaged together, the final numerical data presented in Section 5.2 and 7.0 include 100,000 *r*-values in the hard state and 20,000 *r*-values in the soft state, which is considered adequate for statistical reporting purposes. Table 5.1.4-1 lists the average *r*-value and number of *r*-values for each formula in both the hard and soft states.

Table 5.1.4-1: Average number and value of *r*-values

	r-values #	STDEV #	*r*-value Å	STDEV Å
115 soft	1935	46	404.8	7.4
115 hard	9754	55	47.8	0.1
93 soft	2167	42	360.1	3.9
93 hard	9666	79	49.8	0.1
143 soft	1933	26	417.8	6.3
143 hard	9571	62	47.0	0.1

As can be seen, formula 143 has the smallest average *r*-value in the soft state followed by formula 115 and finally formula 93. Formula 143 also has the largest *r*-value in the hard state and formula 93 the smallest.

As described in Section 4.3, Kolmogorov-Smirnov statistics are collected for each formulation under each fitting method in both the hard and soft states. Table 5.1.4-2 lists the KS statistics in the hard and soft states for each fitting method.

Table 5.1.4-2: Kolmogorov-Smirnov statistics for each distribution

	Hard State			Soft State		
Fit	93	115	143	93	115	143
1000	0.107	0.156	0.176	0.018	0.017	0.015
1001	0.114	0.189	0.219	0.021	0.025	0.021
1002	0.097	0.136	0.164	0.015	0.018	0.016
1003	0.104	0.147	0.156	0.018	0.018	0.017
1004	0.104	0.152	0.201	0.018	0.021	0.018
1005	0.116	0.165	0.186	0.014	0.017	0.016
1006	0.121	0.174	0.203	0.028	0.031	0.025
1007	0.123	0.171	0.183	0.022	0.025	0.025
2000	0.107	0.156	0.176	0.018	0.017	0.015
2001	0.107	0.156	0.176	0.034	0.035	0.032
2002	**0.058**	**0.075**	**0.071**	0.016	0.019	0.017
2003	0.087	0.078	0.074	0.018	0.018	0.018
2004	0.067	0.101	0.127	0.018	0.022	0.020
2005	0.082	0.105	0.125	0.015	0.019	0.016
2006	0.119	0.173	0.204	0.030	0.032	0.026
2007	0.111	0.150	0.172	0.034	0.037	0.035
3000	0.107	0.156	0.176	0.018	0.017	0.015
3001	0.119	0.171	0.195	0.015	0.018	0.015
3002	0.100	0.136	0.158	0.011	0.012	0.011
3003	0.106	0.148	0.156	0.012	0.013	0.012
3004	0.106	0.155	0.198	0.012	0.013	0.011
3005	**0.087**	**0.134**	**0.139**	**0.010**	**0.010**	**0.009**
3006	0.125	0.177	0.206	0.023	0.023	0.019
3007	0.110	0.159	0.176	0.013	0.013	0.013
4000	0.107	0.156	0.176	0.018	0.017	0.015
4001	0.151	0.190	0.202	0.106	0.105	0.105
4002	0.151	0.190	0.202	0.106	0.105	0.105
4003	0.151	0.190	0.202	0.106	0.105	0.105
4004	0.151	0.190	0.202	0.106	0.105	0.105
4005	0.151	0.190	0.202	0.106	0.105	0.105
4006	0.151	0.190	0.202	0.106	0.105	0.105
4007	0.151	0.190	0.202	0.106	0.105	0.105

The minimum KS statistic, and thus the smallest associated error, is attained by fitting method "3005" for each of the formulas in the soft state, which corresponds to a Johnson bounded (SB) distribution using the L_∞-norm estimation fitting method. Although the "2002" fitting method corresponding to a Johnson unbounded (SU) distribution and ordinary least squares fitting method, highlighted in blue in Table 5.1.4-2, has the smallest KS statistic in the hard state, the choice was made to evaluate the performance of the polymers based on the "3005" fitting

method, highlighted in red in Table 5.1.4-2, for several reasons. First, it is desired that the fitting method remain consistent between polymer states resulting in more consistent relative predictions. Second, the "3005" fitting method appears to be an *overall* better fit than the "2002" method, despite having a larger maximum difference between the fitted and actual data, see Figure 5.2.1.1-6.

5.2 RIS MODEL RESULTS

5.2.1 RIS Model Conformation Results

5.2.1.1 Formula EAS-155-115 Conformation Results

Pictured below in Figures 5.2.1.1-1 and 5.2.1.1-2 are example chain conformations of polymer formula EAS-155-115 both the hard and soft states. The blue lines represent individual bonds and the red lines delineate crosslink locations. The difference in the blue lines between Figures 5.2.1.1-1 and 5.2.1.1-2 are due to the figures representing different conformations, while the increase in length of the red lines between the two figures represents the increase in distance between crosslinks in the soft state versus the hard state. Figure 5.2.1.1-3 is an enlargement of a section of Figure 5.2.1.1-1 showing the centers of the polymer segments as blue circles, segment bonds as blue solid lines, and the locations of crosslinks and *r*-values as red dotted lines. As can be seen from the Figure, there is significant variation in the distances between crosslinks.

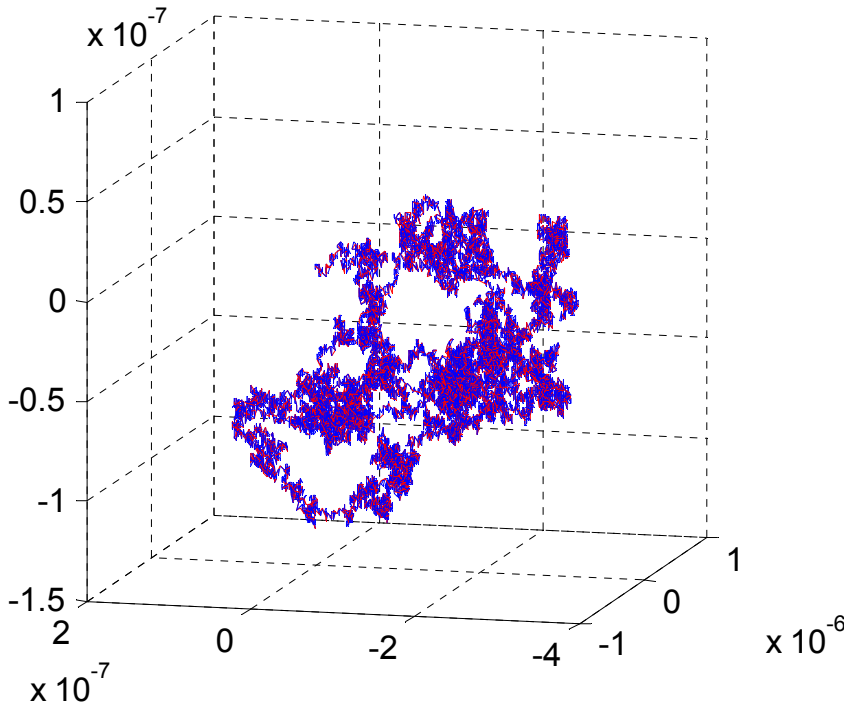

Figure 5.2.1.1-1: Example formula EAS-155-115 polymer chain conformation in the hard state

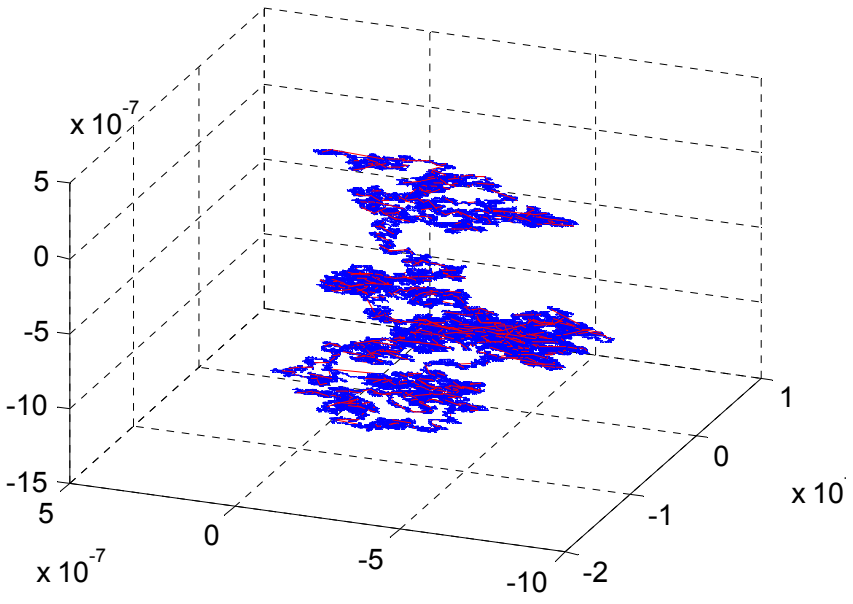

Figure 5.2.1.1-2: Example formula EAS-155-115 polymer chain conformation in the soft state

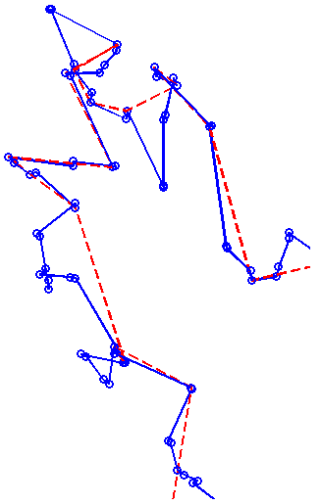

Figure 5.2.1.1-3: Enlargement of Figure 5.2.1.1-1 showing segment bonds and crosslink locations

From data collected during the generation of the polymer chain conformation, a list of *r*-values for both the inherent, P-K-P, crosslink locations and the photo-crosslink, Ω, locations are generated. These lists are then modeled using Johnson probability distribution functions as described in Section 4.2. Pictured below, Figures 5.2.1.1-4 and 5.2.1.1-5 show the modeled PDFs for both the hard case, using the list of *r*-values connecting photo-crosslink locations, and the soft case, using the list of *r*-values connecting inherent crosslinks in the polymer.

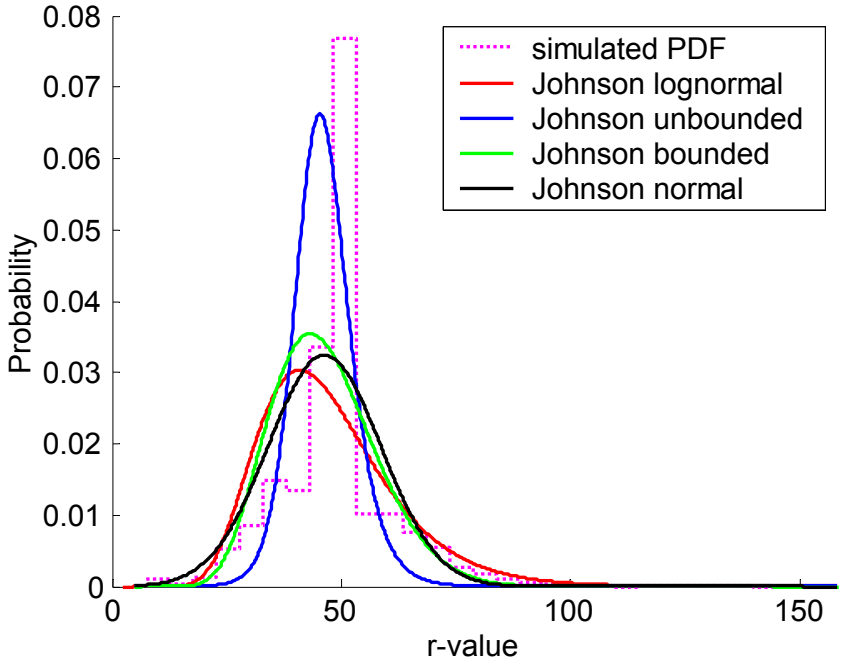

Figure 5.2.1.1-4: Johnson PDFs for formula EAS-155-115 in the hard state

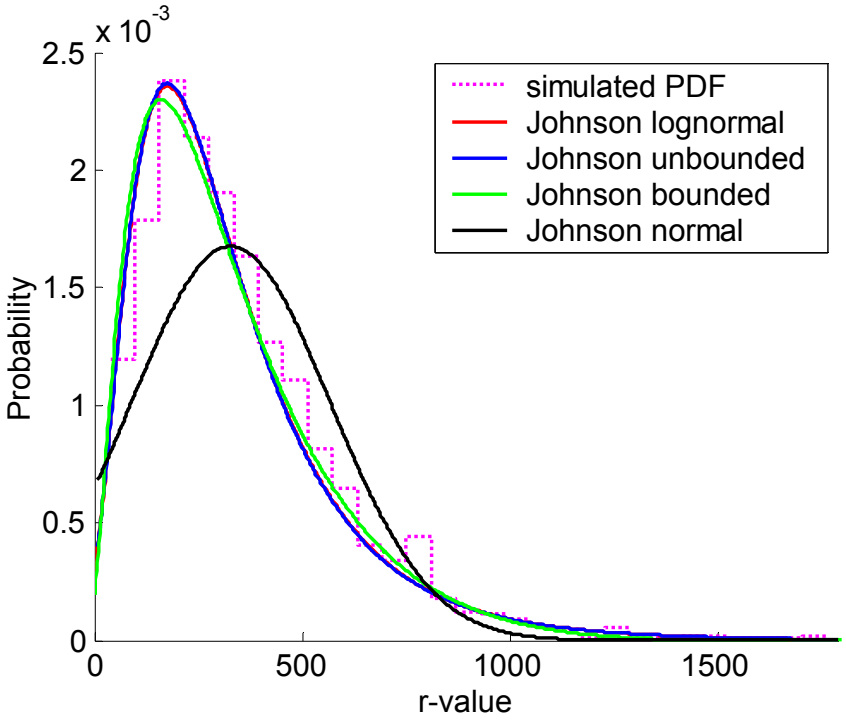

Figure 5.2.1.1-5: Johnson PDFs for formula EAS-155-115 in the soft state

As can be seen from the Figures, the bounded and unbounded distributions are the preferred fit in both states, while the normal distribution is much less accurate. Here, and throughout the work, all four Johnson distributions are presented in the figures for comparison. All numerical data, however, is based on the bounded distribution. From the Johnson distributions, cumulative distribution plots are also created, pictured below in Figures 5.2.1.1-6 and 5.2.1.1-7, and used to calculate Kolmogorov-Smirnov statistics, listed previously in Tables 5.1.4-2 and 5.1.4-3.

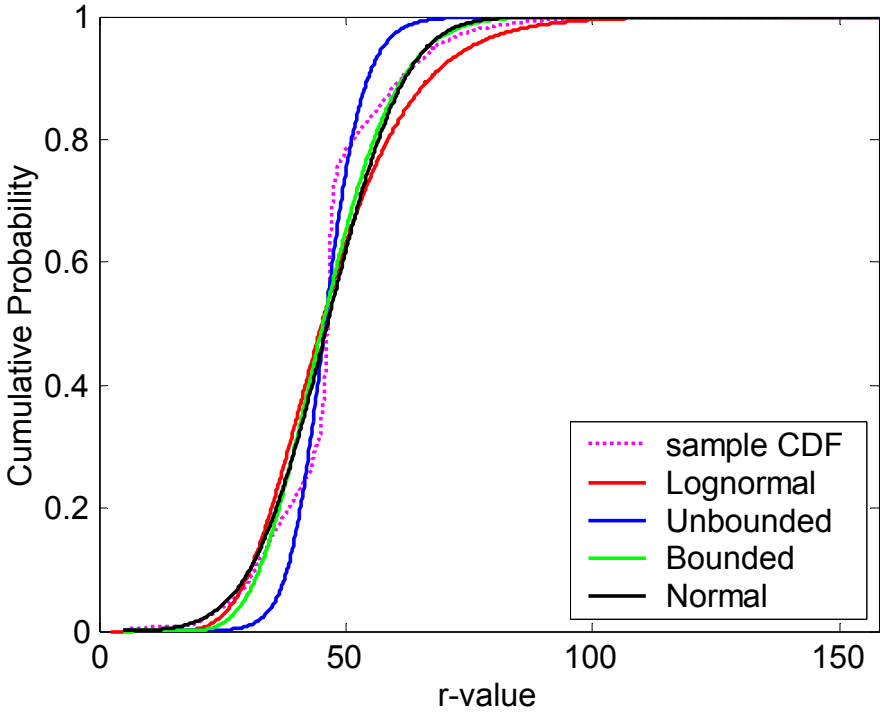

Figure 5.2.1.1-6: Johnson CDFs for formula EAS-155-115 in the hard state

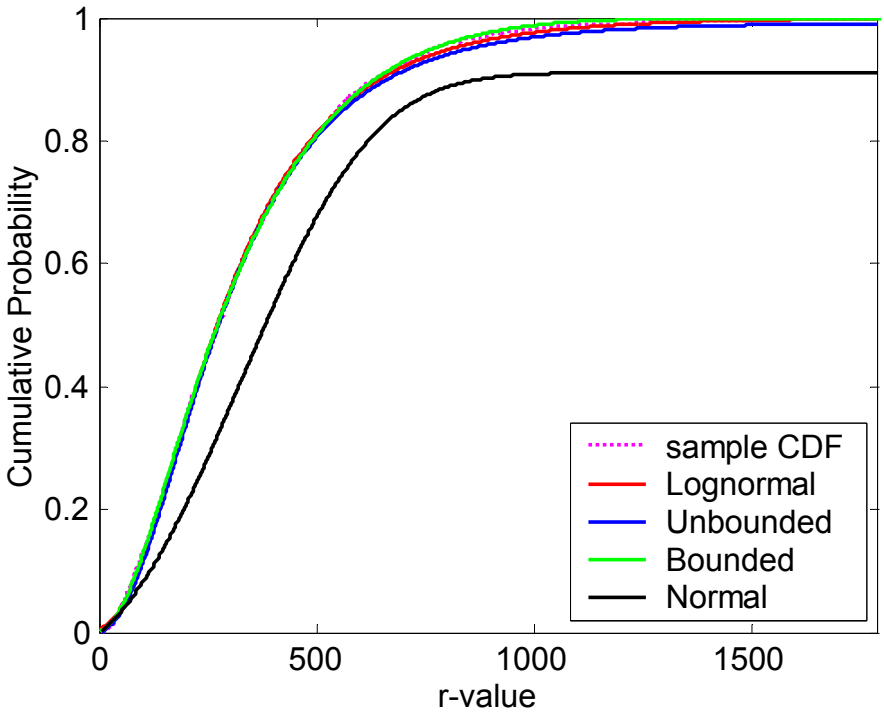

Figure 5.2.1.1-7: Johnson CDFs for formula EAS-155-115 in the soft state

While three of the distributions in the soft state illustrated in Figure 5.2.1.1-7 provide similar fits, differences in the distributions are more apparent in the hard state in Figure 5.2.1.1-6. As discussed previously, the bounded distribution is more accurate near the lower and upper limits of the data while the unbounded distribution more accurately captures the peak of the PDF or the center section of the CDF shown in Figure 5.2.1.1-6 in the hard state.

5.2.1.2 Formula EAS-155-93 Conformation Results

Example polymer chain conformations for formula EAS-155-93 are shown below in Figures 5.2.1.2-1 and 5.2.1.2-2.

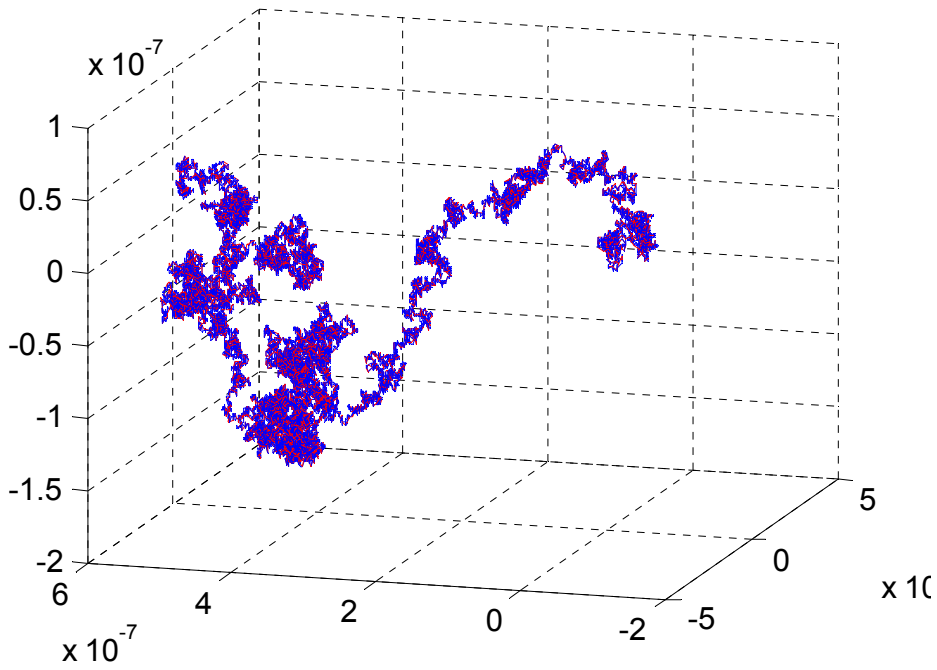

Figure 5.2.1.2-1: Example formula EAS-155-93 polymer chain conformation in the hard state

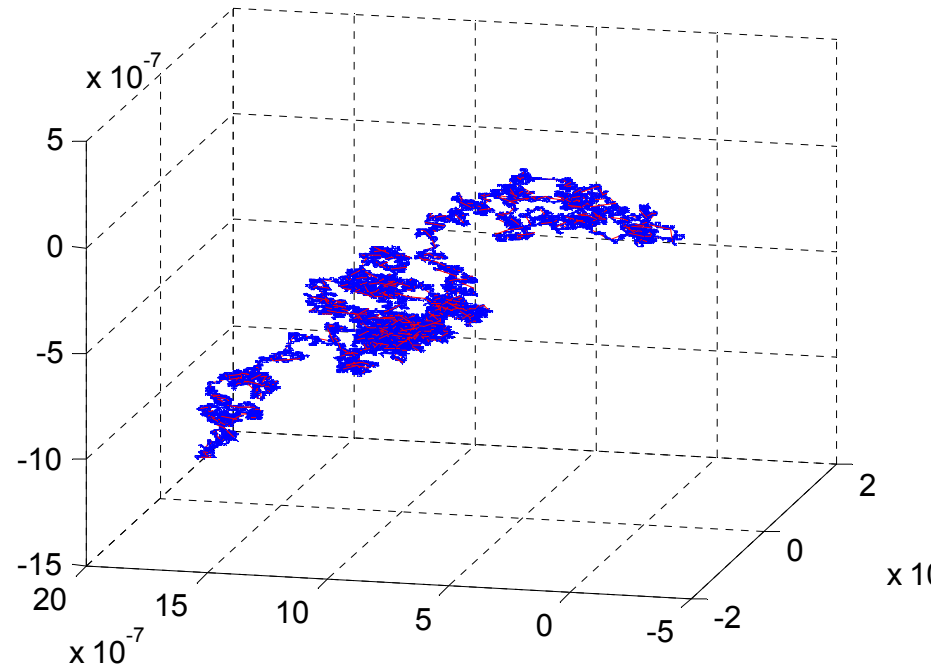

Figure 5.2.1.2-2: Example formula EAS-155-93 polymer chain conformation in the soft state

The conformations shown above for formula EAS-155-93 are similar in structure to those pictured for formula EAS-155-115. From the simulated polymer chain, lists of *r*-values are generated in both the hard and soft states of the polymer and modeled using the L_∞-norm fitting method. The PDFs and CDFs in the hard and soft states for formula EAS-155-93 are pictured below as Figures 5.2.1.2-3 through 5.2.1.2-6.

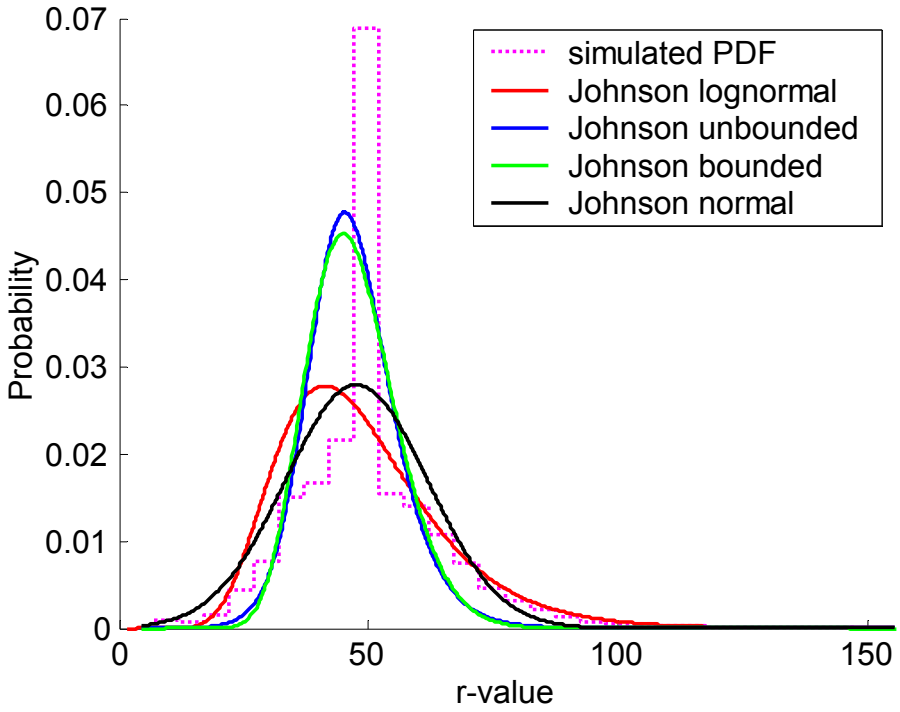

Figure 5.2.1.2-3: Johnson PDFs for formula EAS-155-93 in the hard state

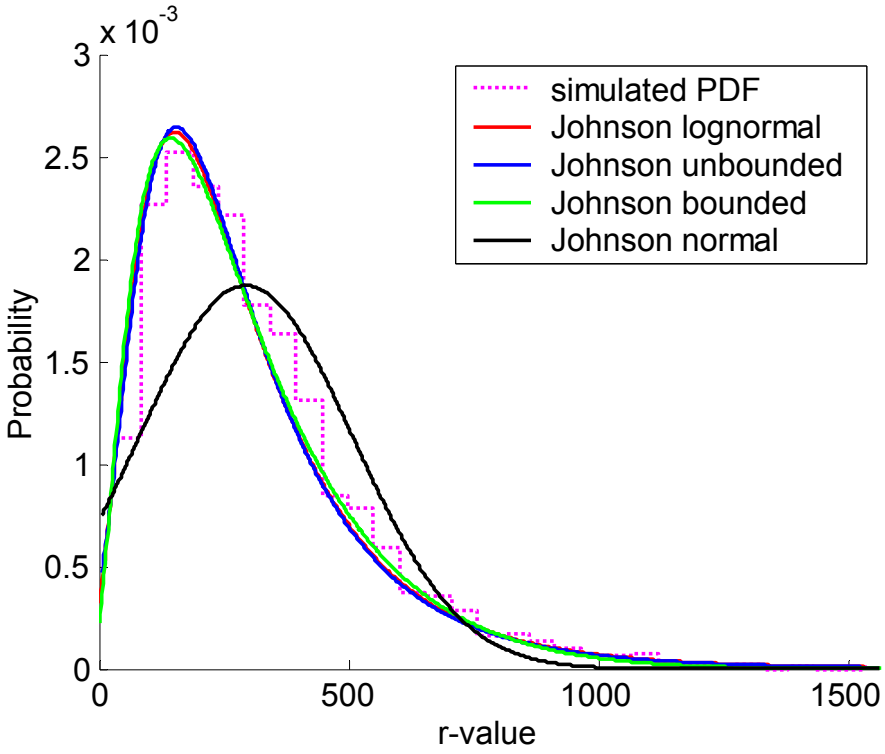

Figure 5.2.1.2-4: Johnson PDFs for formula EAS-155-93 in the soft state

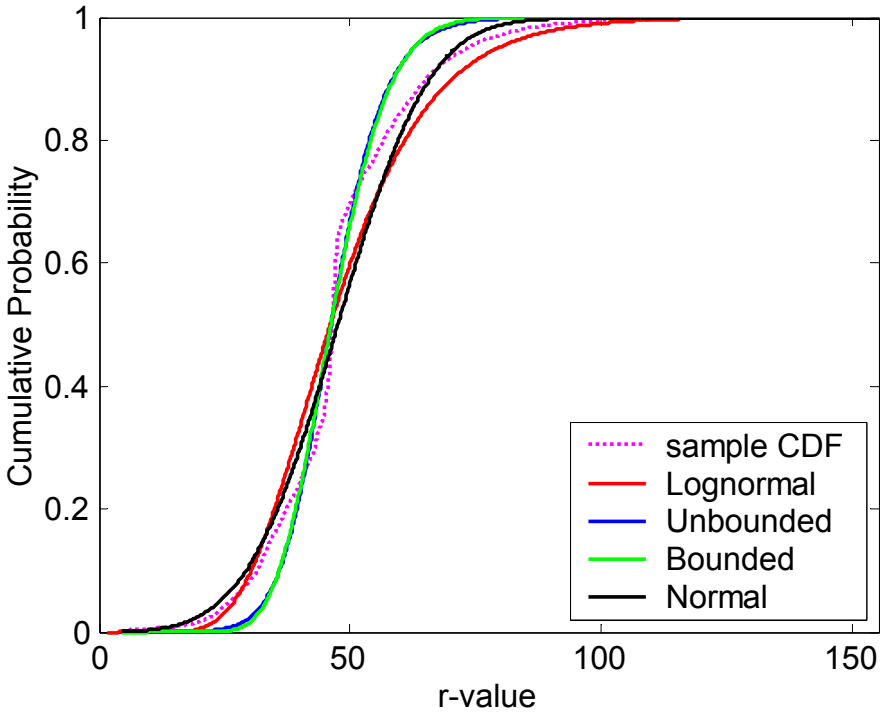

Figure 5.2.1.2-5: Johnson CDFs for formula EAS-155-93 in the hard state

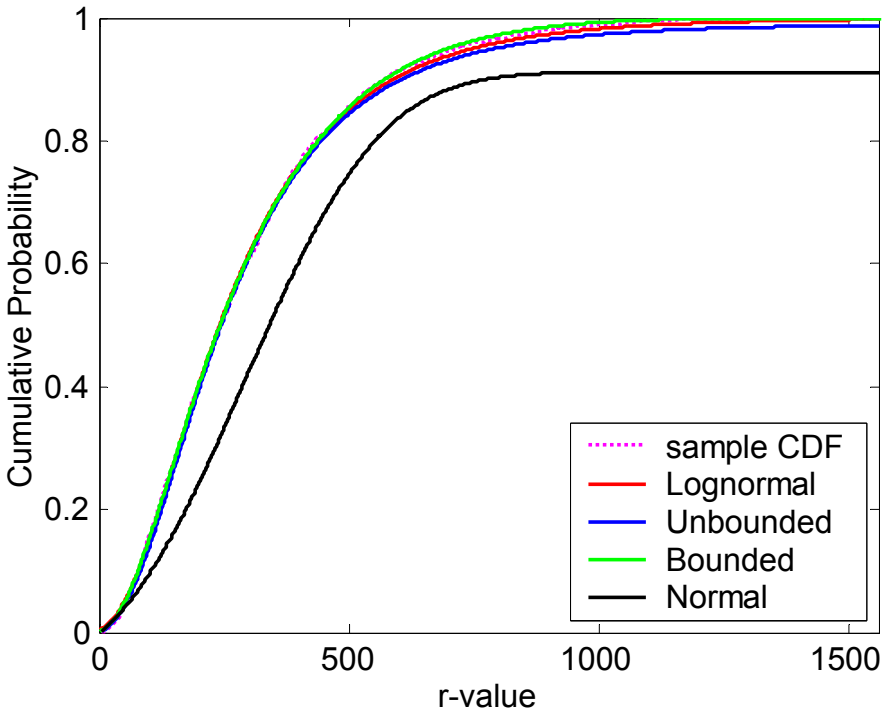

Figure 5.2.1.2-6: Johnson CDFs for formula EAS-155-93 in the soft state

As can be seen from the Figures, the unbounded and bounded distributions are very similar, both providing accurate representations of the simulated polymer chain for formula 93. The Kolmogorov-Smirnov statistics associated with the distributions pictured in Figures 5.2.1.2-5 and 5.2.1.2-6 are listed previously in Tables 5.1.4-2 and 5.1.4-3

5.2.1.3 Formula EAS-155-143 Conformation Results

Figures 5.2.1.3-1 and 5.2.1.3-2, pictured below, are typical conformations of formula EAS-155-143 with the associated PDFs and CDFs shown in Figures 5.2.1.3-3 through 5.2.1.3-6.

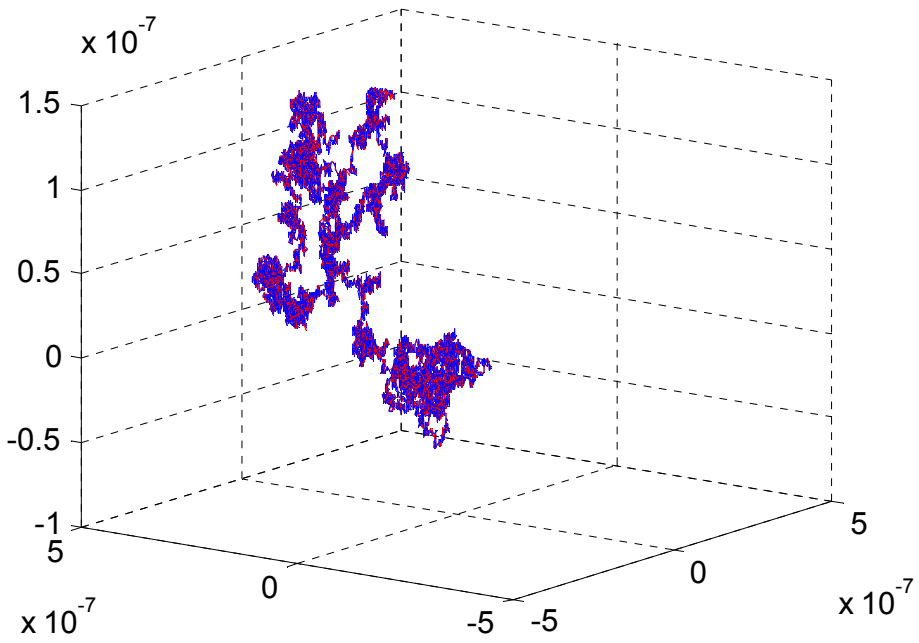

Figure 5.2.1.3-1: Example formula EAS-155-143 polymer chain conformation in the hard state

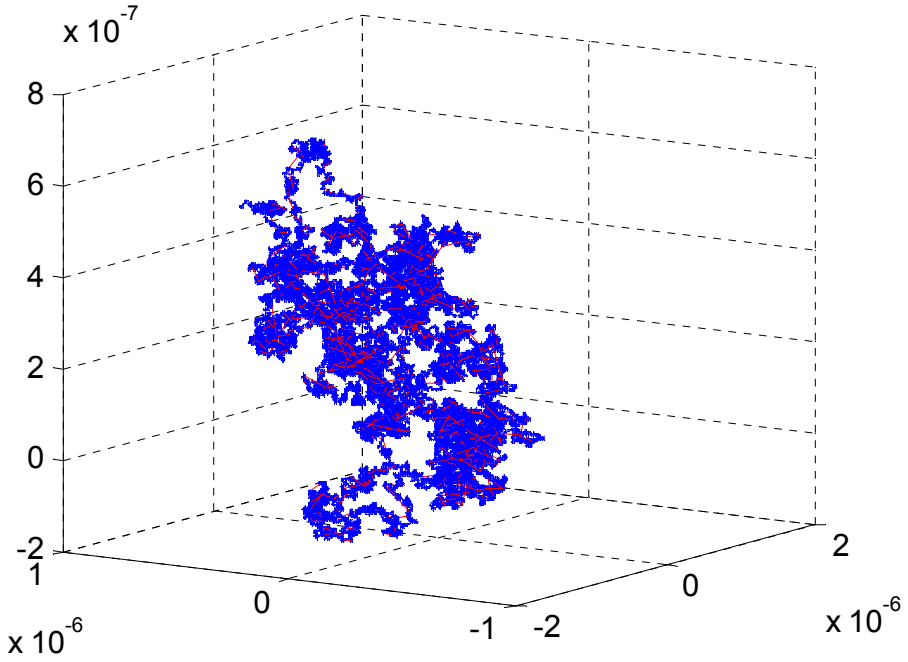

Figure 5.2.1.3-2: Example formula EAS-155-143 polymer chain conformation in the soft state

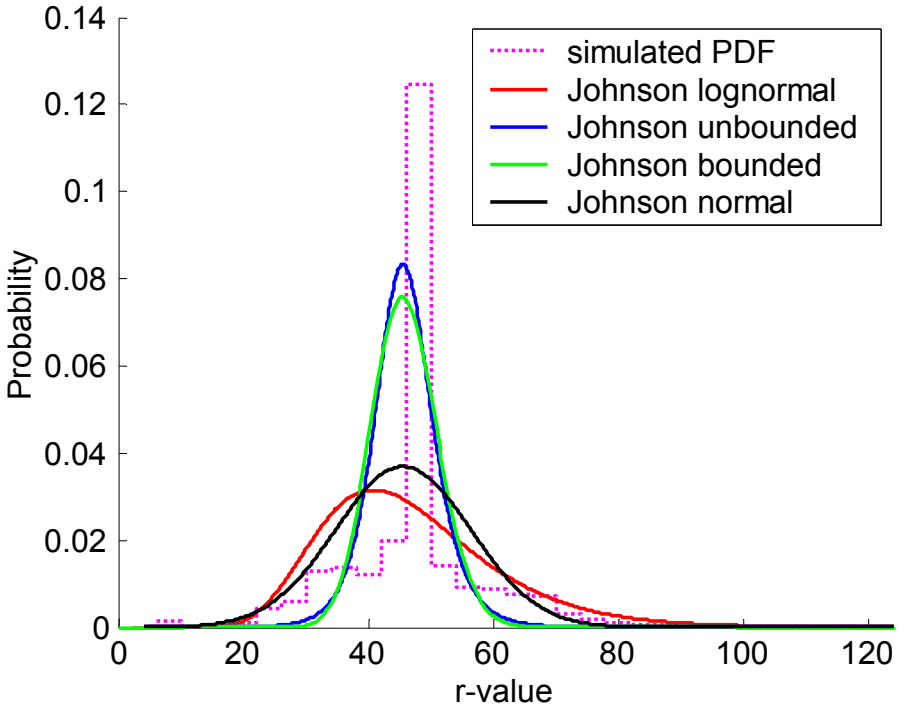

Figure 5.2.1.3-3: Johnson PDFs for formula EAS-155-143 in the hard state

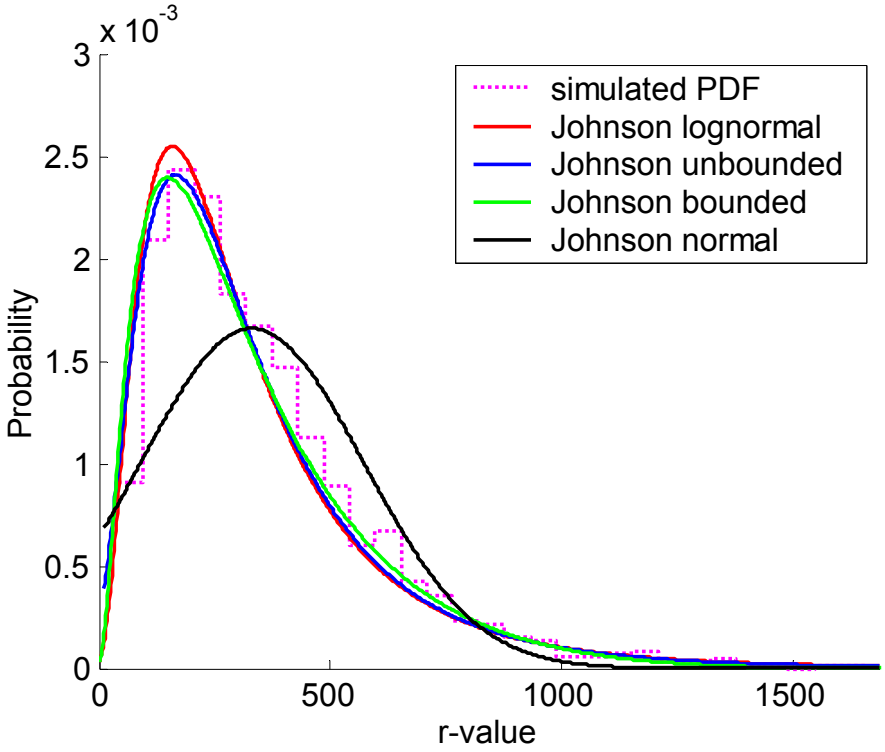

Figure 5.2.1.3-4: Johnson PDFs for formula EAS-155-143 in the soft state

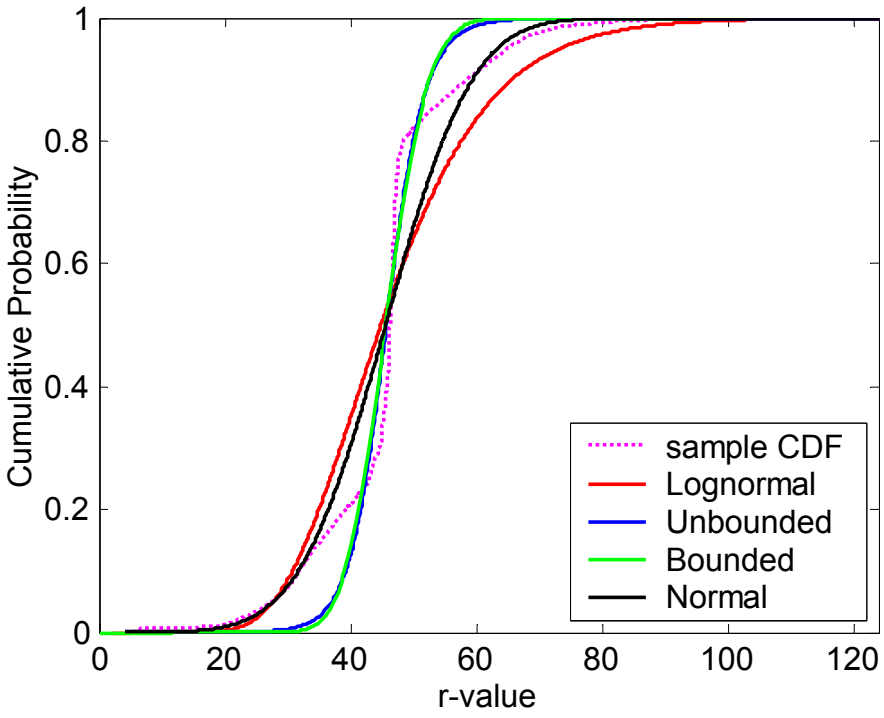

Figure 5.2.1.3-5: Johnson CDFs for formula EAS-155-143 in the hard state

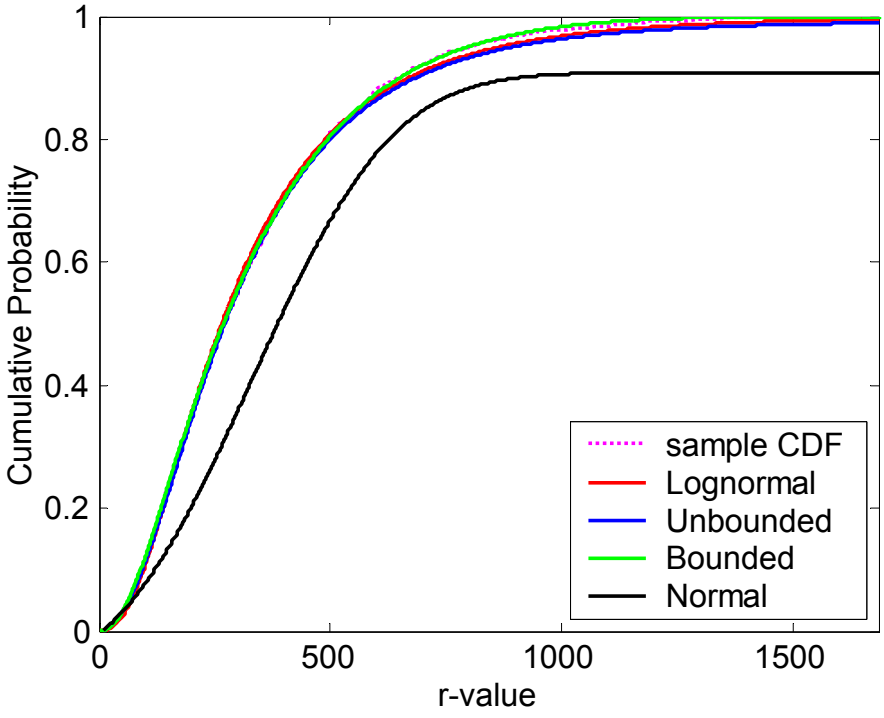

Figure 5.2.1.3-6: Johnson CDFs for formula EAS-155-143 in the soft state

As can be seen from the Figures, formula 143 also has similar structure to the previous two formulas. Also as with formula 93, the unbounded and bounded distributions modeling formula 143 are similar. The Kolmogorov-Smirnov statistics used to evaluate the "goodness of fit" associated with the distributions pictured in Figures 5.2.1.3-5 and 5.2.1.3-6 are listed above in Tables 5.1.4-2 and 5.1.4-3.

5.2.2 RIS Model Tensile Test Results

Using the Johnson Bounded distribution with the L_∞-norm estimation fitting method, the stress due to strain is calculated as described in Section 4.4 using statistical mechanics with the coefficients for simple extension from Table 4.4-1. Stress-strain curves for each of the three modeled formulas in both the soft and hard states are presented in the following sections. As can be seen in each of the graphs, the stress becomes zero at α equal to 1, representing a strain of 0. Quantities of α less than 1 represent compression; while quantities of α greater than 1 represent tension.

5.2.2.1 Formula EAS-155-115 Tensile Test Results

Presented below in Figures 5.2.2.1-1 and 5.2.2.1-2 are typical stress-strain curves for formula EAS-155-115 under simple tension. As expected, the stress is positive under tension and negative under compression.

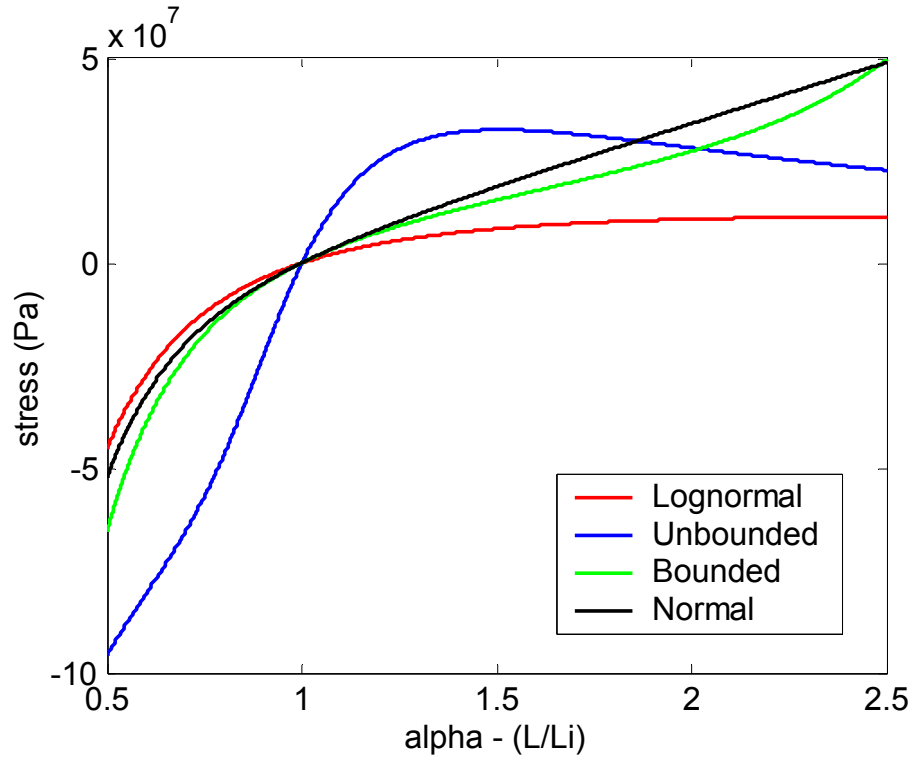

Figure 5.2.2.1-1: Predicted stress response of formula EAS-155-115 in the hard state

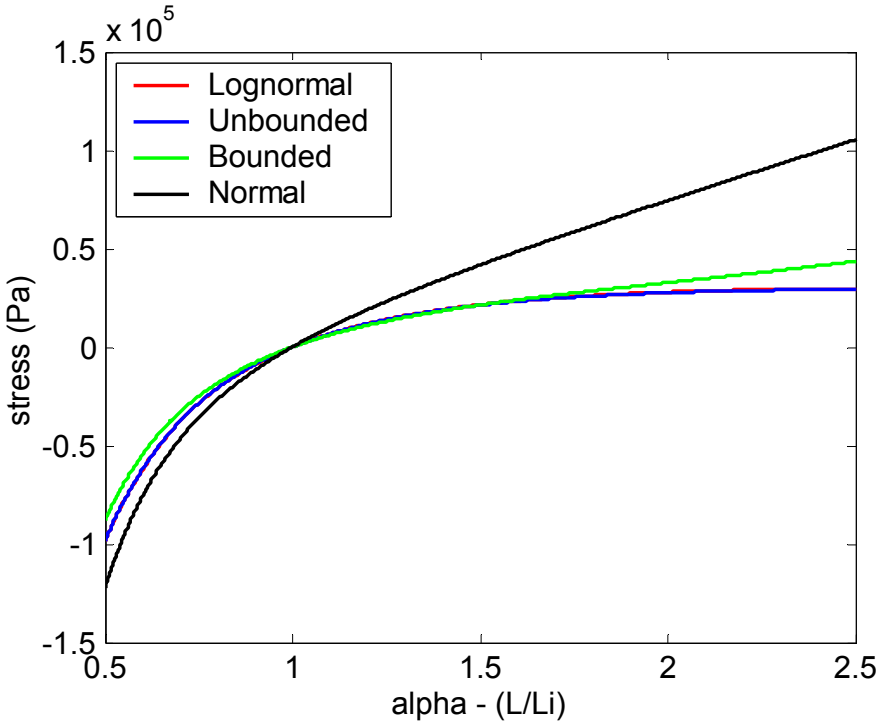

Figure 5.2.2.1-2: Predicted stress response of formula EAS-155-115 in the soft state

Table 5.2.2.1-1 below lists the predicted Young's modulus of the RIS model as compared to previously reported experimental results. Moreover, the experimental measurement of stiffness necessarily embodies stiffness gradation associated with light penetration limitations. Therefore, the empirically fit chemical kinetic model results are presented to estimate the stiffness of the samples' incident layer as a comparison base for the first principles RIS prediction. As is expected, the RIS model underestimates the stiffness of the polymer in both the soft and hard states by a significant amount.

Table 5.2.2.1-1: Comparison of Young's modulus predictions for formula 115

	Young's Modulus MPa	STDEV MPa
Experimental soft state	2.0	NA
RIS model soft state	0.063	0.003
Experimental sample averaged hard state	11.4	NA
Chemical Kinetic model theoretical hard state	110.0	NA
RIS model hard state	49.1	11.1

While both the soft and hard case predictions of Young's modulus are underestimates, the theory does accurately predict a large increase in stiffness due to crosslinking. This is expected due to the difference in the average simulated *r*-value, decreasing from 398.3Å to 47.8Å with increased crosslinking, resulting in an increase in the change in entropy calculated by Equation 4.4-2. Comparison between the experimentally measured stress response of the polymer and that predicted by the model is presented in Section 7.1.1.1 and Figures 7.1.1.1-3 and 4 for both the first principles RIS model and the junction constraints model, discussed in Chapter 6.

5.2.2.2 Formula EAS-155-93 Tensile Test Results

Presented below in Figures 5.2.2.2-1 and 5.2.2.2-2 are typical stress-strain curves for formula EAS-155-93 under simple tension as predicted by the RIS model.

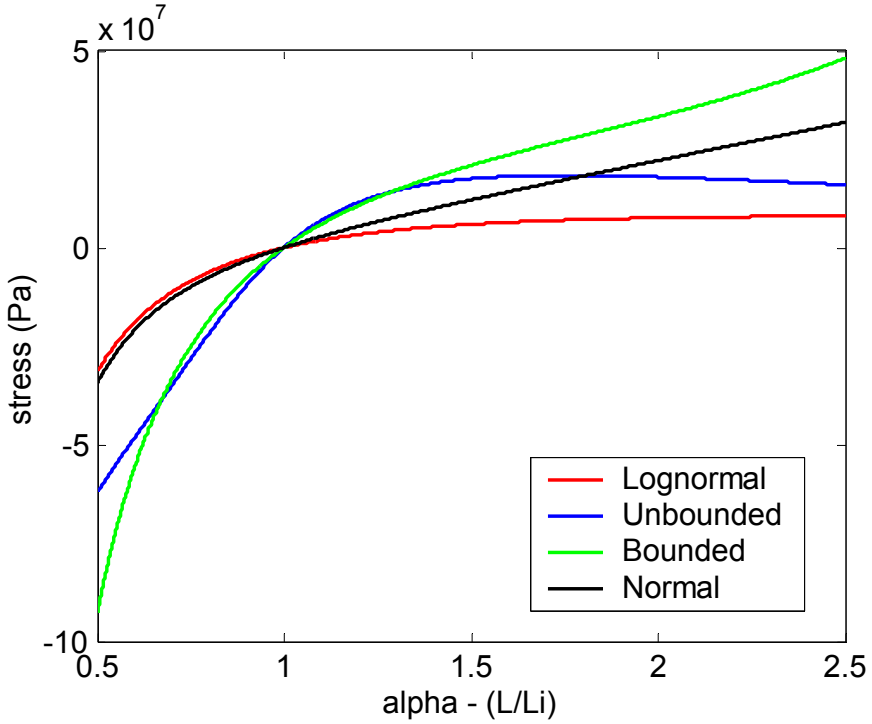

Figure 5.2.2.2-1: Predicted stress response of formula EAS-155-93 in the hard state

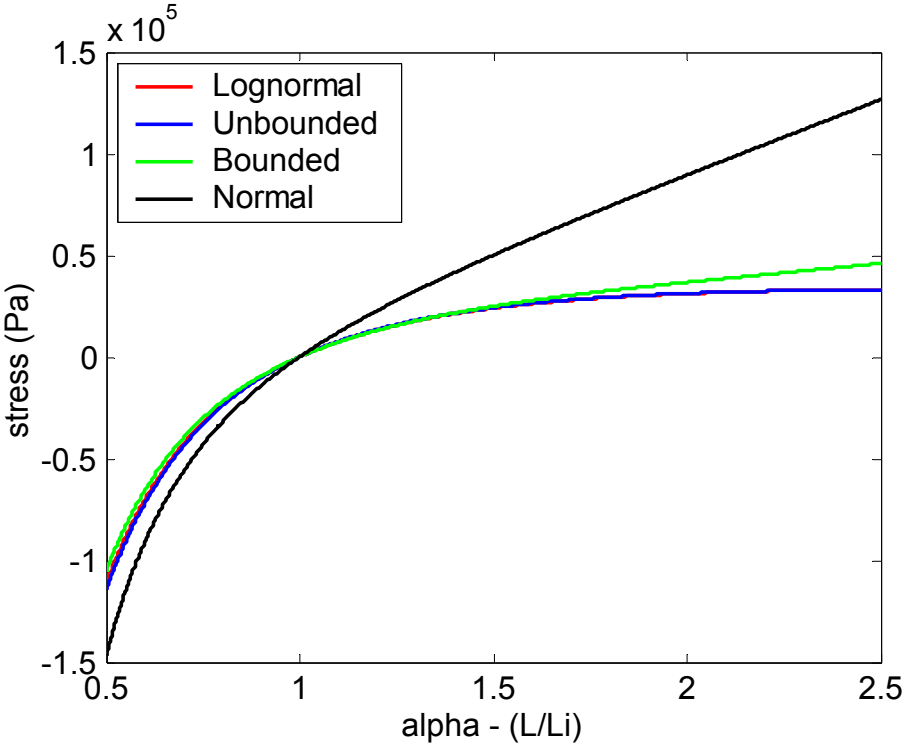

Figure 5.2.2.2-2: Predicted stress response of formula EAS-155-93 in the soft state

The soft state predictions are very similar in shape to that of formula 155 in the previous section while the hard state predictions differ substantially. The difference in the hard state is most pronounced by the unbounded curve. These differences are the result of how the Johnson distributions are fit to model sharp peaks. The peak of the unbounded curve modeling formula 115 in the hard state, Figure 5.2.1.1-4, is much sharper than the peak modeling formula 93 in Figure 5.2.1.2-3, resulting in drastically different stress-strain predictions. Table 5.2.2.2-1 below lists the predicted Young's modulus of the RIS model as compared to previously reported experimental results for formula 93. As is expected, the RIS model underestimates the stiffness of the polymer in both the soft and hard states by an amount similar to that found with formula 115. The predicted RIS Young's modulus of the polymer is only 7.7% of that expected from the chemical kinetic model. As with formula 115, comparison between the experimentally measured

stress response of the polymer and that predicted by the model is presented in Section 7.1.1.2 and Figures 7.1.1.2-3 and 4 for both the first principles RIS model and the junction constraints model, discussed in Chapter 6.

Table 5.2.2.2-1: Comparison of Young's modulus predictions for formula 93

	Young's Modulus MPa	STDEV MPa
Experimental soft state	5.0	NA
RIS model soft state	0.080	0.006
Experimental sample averaged hard state	106.7	NA
Chemical Kinetic model theoretical hard state	850.0	NA
RIS model hard state	65.1	15.1

Although there are more photo crosslink locations in formula EAS-155-115, Figure 5.1.1-1, the physical lengths of the Ω segments in formula EAS-115-93 are longer than formula EAS-155-115, leading to relatively similar simulated r_0 values. In the soft case, the average r_0 value for formula EAS-155-93 is slightly smaller than formula EAS-155-115, expectedly yielding a slightly higher modulus prediction for formula EAS-155-93, which is consistent with the trends seen in experimental testing. In the hard state, however, the average r_0 value for formula EAS-155-93 is slightly larger than for formula EAS-155-115, resulting in slightly lower modulus predictions. While the method correctly predicts a significant increase in stiffness due to crosslinking, increasing from 2.3 to 103.0 MPa, the relative stiffness between the two formulas is not consistent with experiment. A possible source of error explaining this discrepancy includes inaccuracies in the method used to calculate the physical lengths of the individual segments, which is based on their molecular weights. The error also could be a result of inaccuracies in the hard state modulus estimation from the chemical kinetic model, presented in Section 3.1, which is expected to overestimate the polymer's stiffness. When accounting for the standard deviation

associated with each formula's r_0 value, however, the two formulas are statistically indifferent according to the model.

5.2.2.3 Formula EAS-155-143 Tensile Test Results

Figures 5.2.2.3-1 and 5.2.2.3-2 shown below are typical stress-strain curves for formula EAS-155-143 under simple tension as predicted by the RIS model. Again, due to the differences in the distribution of *r*-values, and thus the subsequent PDF describing them, the stress-strain curves are noticeably different than those previously presented for formulas 115 and 93.

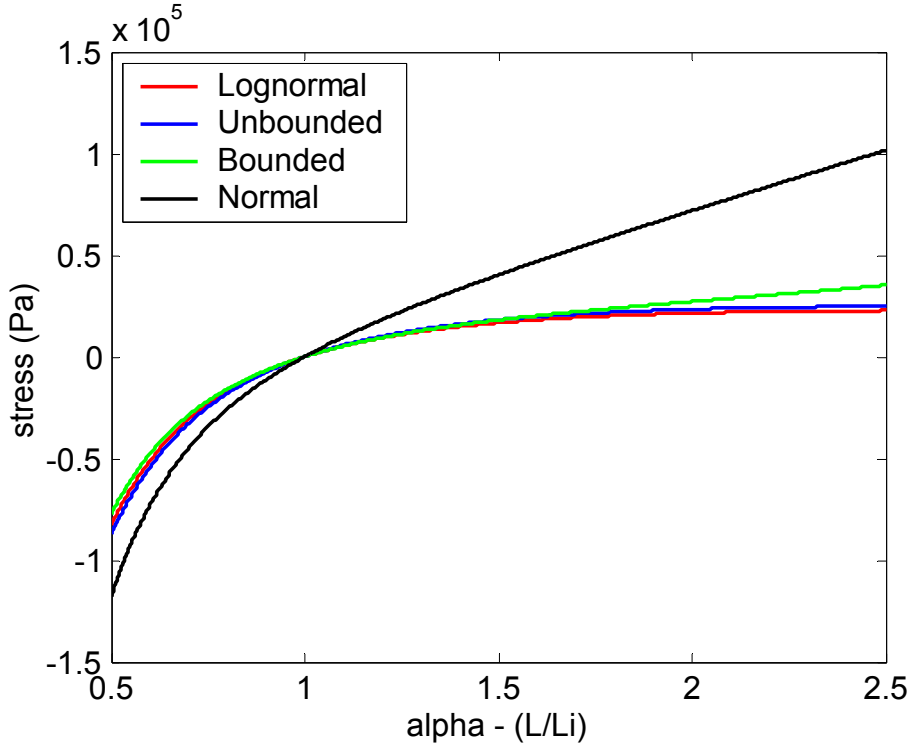

Figure 5.2.2.3-1: Predicted stress response of formula EAS-155-143 in the soft state

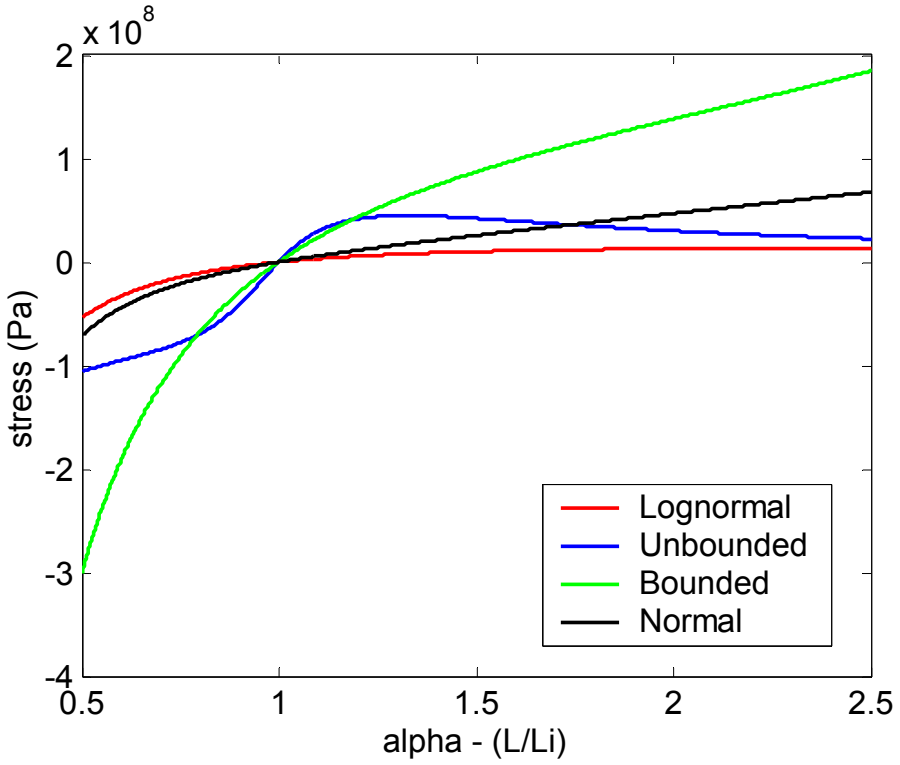

Figure 5.2.2.3-2: Predicted stress response of formula EAS-155-143 in the hard state

Table 5.2.2.3-1 below lists the predicted Young's modulus of the RIS model as compared to previously reported experimental results for formula 143. As expected, the RIS model underestimates the stiffness of the polymer in the soft state by an amount similar to that found with formula 115. While the model predicts a hard state modulus of 232 MPa, experimental data is unavailable for comparison.

Table 5.2.2.3-1: Comparison of Young's modulus predictions for formula 143

	Young's Modulus MPa	STDEV MPa
Experimental soft state	1.13	NA
RIS model soft state	0.063	0.002
Experimental sample averaged hard state	NA	NA
Chemical Kinetic model theoretical hard state	NA	NA
RIS model hard state	232.0	81.7

5.3 RIS MODEL CONCLUSIONS

RIS theory underestimates the Young's moduli of the polymer. It does, however, provide an accurate and valuable gage for the relative material properties between formulae. Experimentally, formula 143 is the least stiff in both the soft and hard states, followed by formula 115, with formula 93 being the stiffest. This ranking of the stiffness of the polymer in the soft state is mirrored by the predicted moduli by RIS theory. Although the nominal values are inaccurate, the relative predictions coincide with observed experimental values. Thus, the original goal of the model of having the capability to evaluate select candidate formulas with respect to other formulas of the same chemical makeup is achieved. The ability of quickly and accurately ranking candidate formulas according to their predicted stiffness will drastically reduce the time required for formula synthesis and material testing.

Table 5.3-1: Comparison of RIS predicted and experimental Young's moduli

		Soft State MPa	Hard State MPa
Formula 115	Experimental	2.0	110
	RIS model	0.06	49
Formula 93	Experimental	5.0	850
	RIS model	0.08	65
Formula 143	Experimental	1.13	NA
	RIS model	0.06	232

6.0 JUNCTION CONSTRAINT THEORY

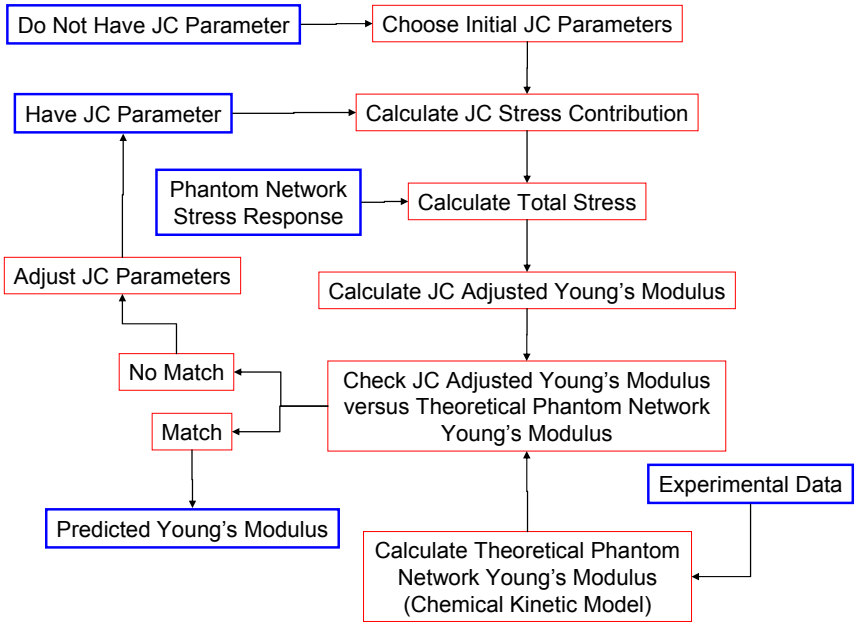

Figure 6.0-1: Module 4, diagram of flow for junction constraint theory model

The application of rotational isomeric state theory as described in Chapters 5 and 6 considers only a single polymer chain, or phantom network, and neglects all physical chain interactions with itself or neighboring chains, resulting in underestimated material characteristics. In this chapter, to account for physical constraints on the polymer chain, the stress on the chain is described as having two contributions, one derived from the phantom network as outlined in the previous chapters and one due to junction constraints, where a junction is defined as any point where a force is exerted on the polymer chain, such as a crosslink or physical entanglement. The

integration of junction constraint considerations into the phantom network is described by the flow chart of Figure 6.0-1 [15-17].

6.1 MODEL DERIVATION

The below derivation is a brief synopsis of the original proof, a more detailed review of which can be found here [97-99]. To include the stress due to junction constraints, a statistical approach is taken based on the graphical representation shown in Figure 6.1-1. The elastic free energy of a phantom network of Gaussian chains is expressed by:

$$\Delta A_{ph} = \left(\frac{1}{2}\right)\zeta kT\left(\lambda_1^2 + \lambda_2^2 + \lambda_3^2 - 3\right) \tag{6.1-1}$$

where ζ is the cycle rank, k is Boltzmann's constant, T is temperature, and λ represents the stretch in the three primary directions relative to an unperturbed reference state.

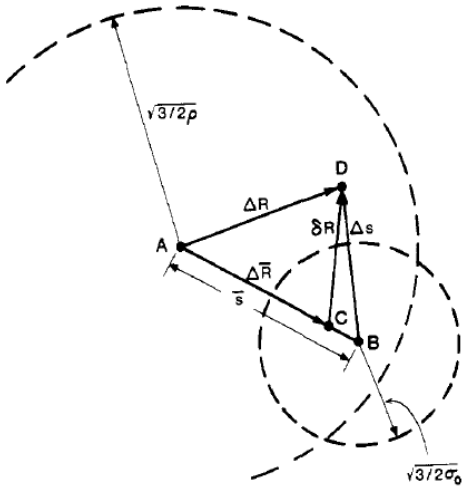

Figure 6.1-1: Diagram depicting the basis of junction constraint theory [98]

The points *A*, *B*, *C*, and *D* represent the mean location of the junction being modeled (*A*), the mean location of the nearest neighboring junction (*B*), the current location of the nearest neighboring junction (*C*), and the current location of the modeled junction (*D*). The distances between the current modeled junction, the mean location, and the mean neighboring junction location are represented by *R* and *S* respectively. The distributions of *R* and *S* are described by the following Gaussian functions [97-99]:

$$R(\Delta X) = \left(\rho/\pi\right)^{1/2} \exp\left[-\rho(\Delta X)^2\right] \tag{6.1-2}$$

$$\left\langle (\Delta X)^2 \right\rangle = 1/2\rho \tag{6.1-3}$$

$$S(\Delta x) = \left(\sigma_{\lambda_x}/\pi\right)^{1/2} \exp\left[-\sigma_{\lambda_x}(\Delta x)^2\right] \tag{6.1-4}$$

Taking the product of Equations 6.1-2 and 6.1-4 results in the probability of a displacement ΔR_i of junction *i*. Also, we know that the actual distribution of the components $\{\Delta X\}$ of the vectors locating the junctions in the real network $\{\Delta R\}$ under strain relative to their mean positions in the phantom network is calculated by the convolution of the normalized result for the X coordinate and the quantity $\Theta\left(\Delta\overline{X}\right)$ [97-99]. It is then asserted that $\Theta\left(\Delta\overline{X}\right)$ and $R_*(\Delta X)$ (the convolution result) are Gaussian for all strains. The distribution of mean relative positions of the centers of the constraints, $H\left(\overline{x}\right)$ can then be expressed. After substitution, $R_*(\Delta X)$ becomes:

$$R_*(\Delta X) = \left(\frac{\rho_{*\lambda}}{\pi}\right)^{1/2} \exp\left[-\rho_{*\lambda}(\Delta X)^2\right] \tag{6.1-5}$$

where

$$\frac{\rho}{\rho_{*\lambda}} = 1 + \frac{\left(\frac{\sigma_\lambda}{\rho}\right)\left[\left(\frac{\sigma_\lambda}{\rho}\right)\left(\rho\eta_\lambda^{-1} - 1\right) - 1\right]}{\left(1 + \frac{\sigma_\lambda}{\rho}\right)^2} \tag{6.1-6}$$

Since the actual distribution in the reference state must conform to the distribution in the phantom network [97-99],

$$\eta_0^{-1} = \rho^{-1} + \sigma_0^{-1} \tag{6.1-7}$$

From Equation 6.1-7, substitution of $\rho\eta_\lambda^{-1}$ in Equation 6.1-6 with $(\eta_0/\eta_\lambda)(1 + \rho/\sigma_0)$ yields

$$\frac{\rho}{\rho_{*\lambda}} = 1 + \frac{\left(\frac{\sigma_\lambda}{\rho}\right)^2\left(\frac{\eta_0}{\eta_\lambda} - 1\right) + \left(\frac{\sigma_\lambda}{\rho}\right)\left[\left(\frac{\eta_0}{\eta_\lambda}\right)\left(\frac{\sigma_\lambda}{\sigma_0}\right) - 1\right]}{\left(1 + \frac{\sigma_\lambda}{\rho}\right)^2} \tag{6.1-8}$$

From Equation 6.1-1, the principal components of stress contributed by constraints are given by [97-99]

$$\tau_{jc} = \frac{vkT}{2}\left[K\left(\lambda_1^2\right)\frac{\partial \lambda_1^2}{\partial \alpha} + K\left(\lambda_2^2\right)\frac{\partial \lambda_2^2}{\partial \alpha} + K\left(\lambda_3^2\right)\frac{\partial \lambda_3^2}{\partial \alpha} \right] \tag{6.1-9}$$

with

$$K\left(\lambda^2\right) = B\left[\frac{\dot{B}}{B+1} + \frac{g\left(\dot{g}\, B + g\, \dot{B} \right)}{gB+1} \right] \tag{6.1-10}$$

$$B = \frac{\rho}{\rho_{*\lambda}} - 1 \tag{6.1-11}$$

$$g = \frac{\rho}{\sigma_\lambda} \tag{6.1-12}$$

and

$$\dot{B} = \frac{\partial B}{\partial \lambda^2} \tag{6.1-13}$$

$$\dot{g} = \frac{\partial g}{\partial \lambda^2} \tag{6.1-14}$$

To force the centers of the domains to be affine under macroscopic strain,

$$\frac{\eta_\lambda}{\eta_0} = \lambda^{-2} \tag{6.1-15}$$

We are then left to define the form of σ, which is a function of λ and is a measure of the severity of the interaction between neighboring junctions. This is accomplished by expressing the variance of σ with respect to λ as a power series [97-99]:

$$\begin{aligned}\frac{1}{\sigma_\lambda} &= \frac{\lambda^2}{\sigma_1} + \frac{\lambda^3}{\sigma_2} + \frac{\lambda^4}{\sigma_3} + \frac{\lambda^5}{\sigma_4} + \ldots \\ \frac{1}{\sigma_0} &= \frac{1}{\sigma_1} + \frac{1}{\sigma_2} + \frac{1}{\sigma_3} + \frac{1}{\sigma_4} + \ldots\end{aligned} \tag{6.1-16}$$

While previous works have truncated the expansion at λ^2, the expansion is left open ended in the current work for flexibility of fitting. When Equations 6.1-16 are combined, the resulting expression for the variance of σ becomes

$$\frac{\sigma_0}{\sigma_\lambda} = \lambda^2\left[1 + \frac{\sigma_0}{\sigma_2}(\lambda - 1) + \frac{\sigma_0}{\sigma_3}(\lambda^2 - 1) + \frac{\sigma_0}{\sigma_4}(\lambda^3 - 1) + \ldots\right] \tag{6.1-17}$$

Defining the coefficients as

$$\begin{aligned}\kappa &= \frac{\sigma_0}{\rho} \\ \xi &= \frac{\rho}{\sigma_2} \\ \omega &= \frac{\rho}{\sigma_3} \\ \phi &= \frac{\rho}{\sigma_4}\end{aligned} \tag{6.1-18}$$

Substituting Equations 6.1-18 into Equation 6.1-17 then yields

$$\frac{\sigma_0}{\sigma_\lambda} = \lambda^2\left[1+\kappa\xi(\lambda-1)+\kappa\omega\left(\lambda^2-1\right)+\kappa\phi\left(\lambda^3-1\right)+...\right] \tag{6.1-19}$$

Inserting Equation 6.1-19 into Equation 6.1-12 and taking into account Equations 6.1-18, the quantity *g* becomes

$$g = \frac{\sigma_0}{\sigma_\lambda}\frac{1}{\kappa} = \lambda^2\left[\kappa^{-1}+\xi(\lambda-1)+\omega\left(\lambda^2-1\right)+\phi\left(\lambda^3-1\right)+...\right] \tag{6.1-20}$$

Similarly, from Equations 6.1-8, 6.1-11, 6.1-12, and 6.1-15, the quantity *B* becomes

$$B = \frac{\lambda^2\left(1+\kappa^{-1}\right)-g-1}{\left(1+g\right)^2} \tag{6.1-21}$$

From Equations 6.1-10, 6.1-13, 6.1-14, 6.1-20, and 6.1-21, the stress contribution due to junction constraints is fully characterized. More details of the original theory can be found here [97-99]. The quantities κ, ξ, ω, and φ are phenomenalogically fit parameters, where κ characterizes the stress response of the polymer due to the initial network entanglements and ξ, ω, φ, and any other included higher order term coefficients, represent the departure of the system from affine deformation.

6.2 JUNCTION CONSTRAINT THEORY STABILITY ISSUES

Due to the phenomenological nature of the model, it is possible for instabilities to occur. For certain combinations of coefficients, the denominators of quantities B, $\dot{B}$, and K, shown below in Equations 6.2-1 through 6.2-3, can approach 0. This occurs when either g, B, or the quantity $g*B$ approach -1.

$$B = \frac{\lambda^2\left(1+\kappa^{-1}\right)-g-1}{(1+g)^2} \tag{6.2-1}$$

$$K\left(\lambda^2\right) = B\left[\frac{\dot{B}}{B+1} + \frac{g\left(\dot{g}\,B + g\,\dot{B}\right)}{gB+1}\right] \tag{6.2-2}$$

$$\dot{B} = \frac{\left(1+\kappa^{-1}-\dot{g}\right)(1+g)^2 - \left(\lambda^2\left(1+\kappa^{-1}\right)-g-1\right)\left(2\,\dot{g}(1+g)\right)}{(1+g)^4} \tag{6.2-3}$$

Figures 6.2-1 through 6.2-3 below are mappings of when instabilities occur during tensile, equi-biaxial, and shear tests. The three tests are different because the stretch for each of the tests is different; affecting the quantities g and B, see Table 4.4-1. An instability is said to occur, denoted by a dot in the figures, when the denominator of one of the Equations 6.2-1 through 6.2-3 is between -0.05 and 0.05 and the stretch is between 0.5 and 1.5 in any of the three coordinate directions.

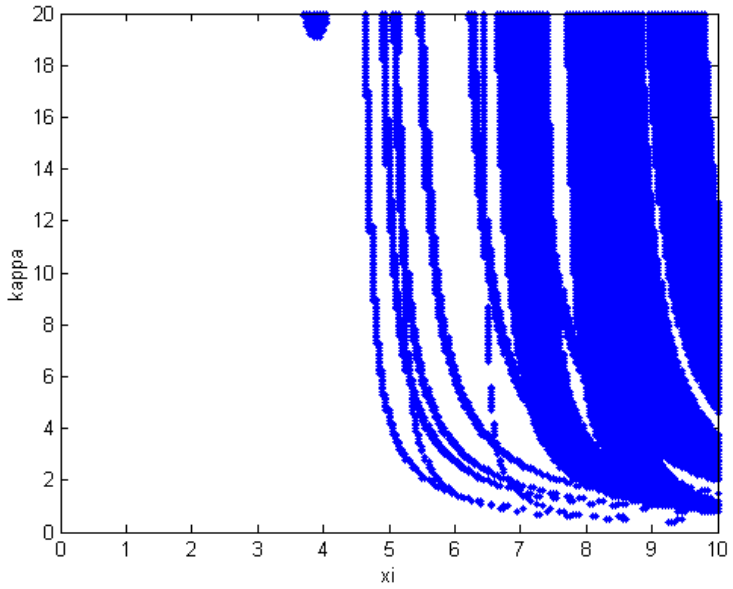

Figure 6.2-1: Instabilities occurring during simple tension modeling

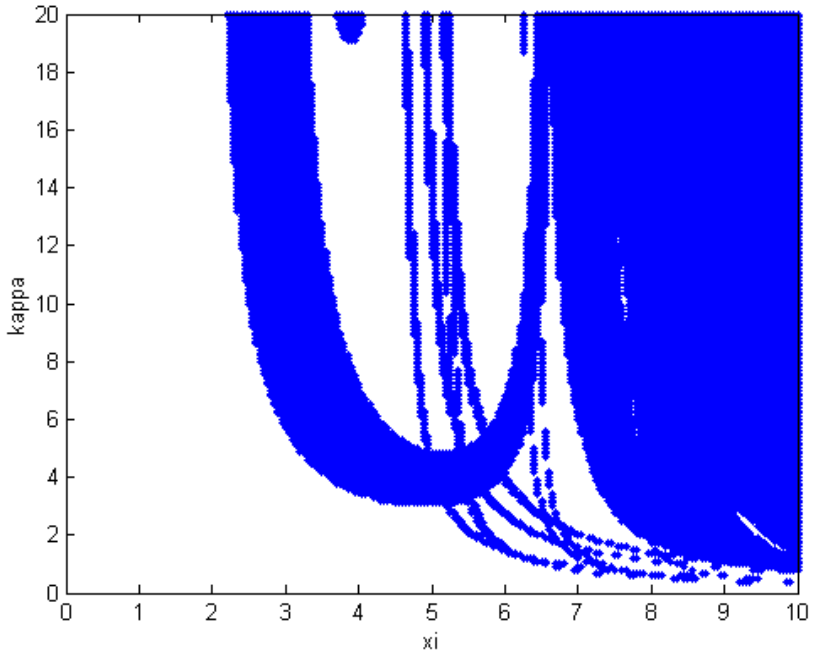

Figure 6.2-2: Instabilities occurring during biaxial modeling

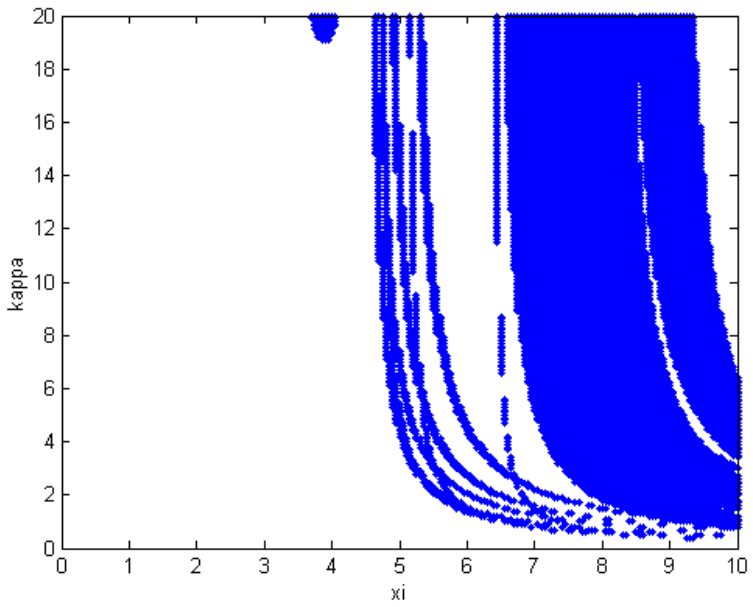

Figure 6.2-3: Instabilities occurring during shear modeling

As can be seen, instabilities occur when ξ is less than 4.5 during tension modeling, 2.0 during biaxial strain modeling, and 4.5 during shear modeling. The safe range during biaxial modeling can be extended to values less than 4.5 for ξ if instabilities occurring only between a stretch of 0.8 and 1.2 are considered. To circumvent these instabilities, κ is given a value of 3.0 and ξ a value of 0.15, well within the range of stable values, with all other higher order coefficients set to 0. Since these values are not high enough to correct the disparities between the RIS predicted modulus values and those found experimentally, however, an additional junction constraint correction factor is added. This correction factor is simply multiplied by the predicted junction constraint stress component and provides the necessary flexibility to force the predicted Young's modulus to match the experimental value.

6.3 MODEL INTEGRATION WITH RIS THEORY

The presented method of calculating the effects of junction constraints results in the prediction of the amount of stress derived solely from a phantom network chain's interactions with neighboring chains. This stress contribution then, is simply added to the stress contribution of the phantom network as calculated using RIS theory for the total stress on the polymer.

$$\sigma_T = f^* + C_{JC}\tau_1 \tag{6.3-1}$$

where σ_T is the total stress on the chain, f^* is the stress due to the phantom network, C_{JC} is the junction constraints correction factor, and τ_1 is the stress due to junction constraints. The total stress on the polymer is then used to calculate the modulus of the polymer as in Equation 4.4-8 as the strain approaches 0.

7.0 JUNCTION CONSTRAINT THEORY MODEL RESULTS

7.1 JUNCTION CONSTRAINT MODEL CALIBRATION

Since the modulus of the polymer is calculated as stretch, α, approaches 1 (strain goes to 0) the departure from affine deformation is expected to have little impact. This also leads to the conclusion, verified by experiment, that any junction constraint coefficient or combination of coefficients may be used to calibrate the model and obtain the desired predicted Young's modulus. Changing the higher order coefficients used in the model results in changes to the predicted stress strain curves, as shown below in Figures 7.1-1 and 7.1-2, with the associated junction constraint coefficients listed in Table 7.1-1.

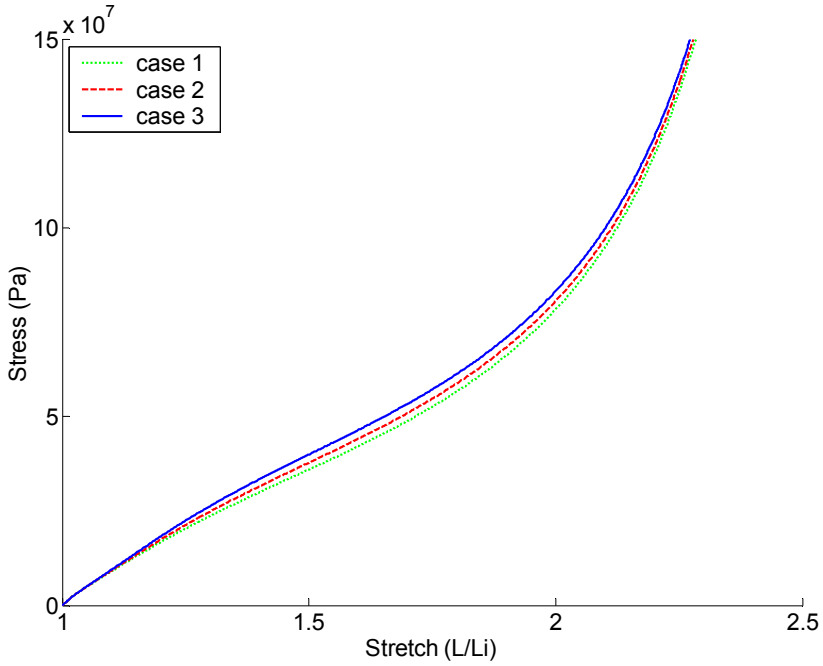

Figure 7.1-1: Stress-strain dependence on higher order junction constraint coefficients in the hard case

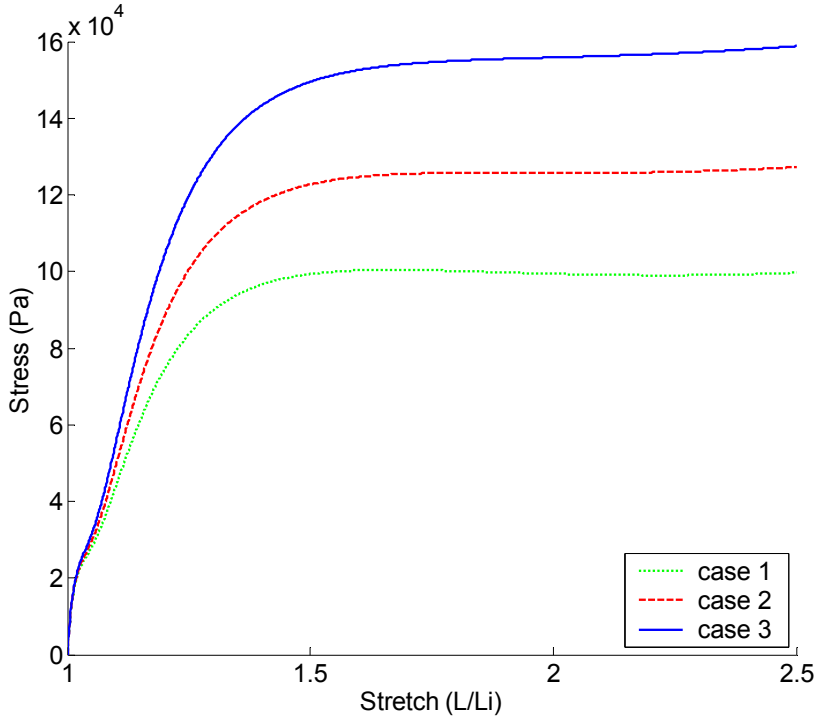

Figure 7.1-2: Stress-strain dependence on higher order junction constraint coefficients in the soft case

Table 7.1-1: Stress-strain dependence on higher order junction constraint coefficients

	Case 1	Case 2	Case 3
κ	10.0	10.0	10.0
ξ	10.7	0.0	0.0
ω	0.0	5.4	0.0
φ	0.0	0.0	3.6

As shown in the above Figures, the model can be calibrated to predict the desired experimental Young's modulus using any combination of junction constraint coefficients. Altering which higher order coefficients are used gives the user a separate and deliberate method to tailor the model to accurately predict other quantities derived from the stress strain curve such as yield and ultimate stresses. From Figures 7.1-1 and 7.1-2 and Table 7.1-1, using increasingly higher order junction constraint coefficients to calibrate the model results in increasingly higher predictions of yield and ultimate stresses in both the soft and hard cases, although the difference is much more pronounced in the soft case. This difference between the two modulus states of the polymer is expected because the higher order terms account for the departure of the system from affine deformation. From Figures 5.2.1.1-5 and 5.2.1.1-6, it can be seen that the distribution of *r*-values, or distances between crosslinks, in the hard case is much smaller than in the soft case. The more uniformly distributed the crosslinks are, yielding a tight distribution, the more affine the deformation is expected to be. This also leads to the conclusion that in the soft state, at a microscopic level, the polymer undergoes non-affine deformation, reaffirming the impact of including junction constraints when predicting material properties.

To calibrate the model, specifically the phenomenologically determined coefficients of the junction constraint theory, several conformations are analyzed and the results averaged. Ten polymer conformations are generated using the above RIS method, each yielding approximately

10,000 *r*-values in the hard case and 2000 in the soft case. Each case is then fit with a Johnson bounded PDF using the L_∞-norm fitting method. The values of the Johnson fitting parameters, δ, λ, ξ, and γ are then input into the phantom network chain model outlined above in Chapter 4.0. The resulting model predictions of the junction constraint theory are then matched to experimental data by adjusting the junction constraint correction factor as described in Section 6.2. The averages and standard deviations of the junction constraint correction factors are listed below in Table 7.1-2.

Table 7.1-2: Average junction constraint correction factors

		JC correction factor	STDEV
Formula 115	Soft	103.8	2.4
	Hard	38.3	12.0
Formula 93	Soft	217.1	4.2
	Hard	568.9	5.7
Formula 143	Soft	60.7	0.8
	Hard 93-ratio	23.2	NA
	Hard 115-ratio	164.6	NA

Since no experimental data for formula 143 in the hard state is available, the model cannot be calibrated for this state. Alternatively, estimations are made based on the ratio of correction factors in the soft and hard states of formulas 93 and 115 and the correction factor for formula 143 in the soft state.

7.1.1 JC Model Tensile Test Results

7.1.1.1 Formula EAS-155-115 Tensile Test Results

Below, a representative case comparing the stress contributions with respect to strain of the phantom network and junction constraints as well as the total stress response of the polymer in

the soft state is presented in Figure 7.1.1.1-1. Shown in Figure 7.1.1.1-2 is the stress contributions from the phantom network, junction constraints, and the total response in the hard state. The average predicted phantom network Young's modulus, junction constraint Young's modulus, root-mean-squared *r*-value, and Kolmogorov-Smirnov statistic from the 10 conformations are also presented below in Table 7.1.1.1-1 compared to the experimentally determined Young's moduli for formula EAS-155-115.

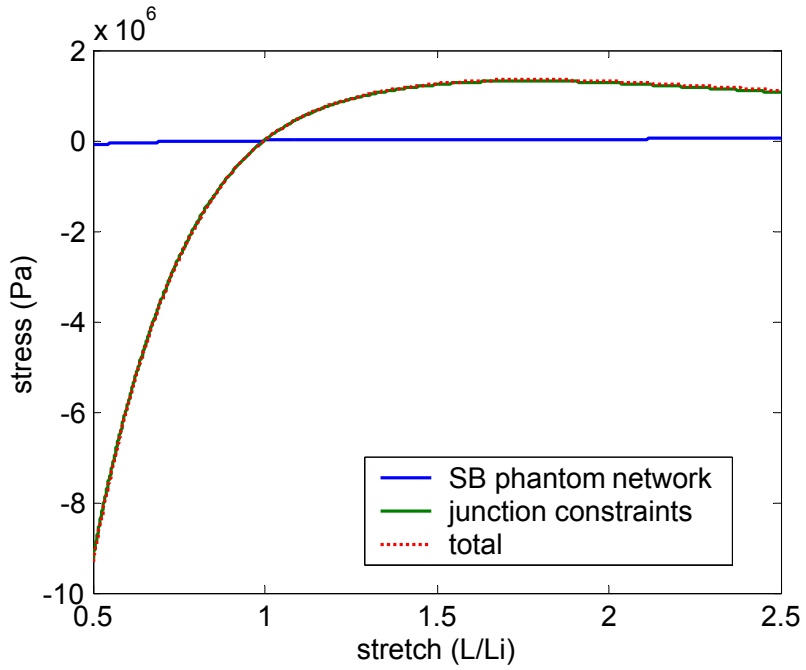

Figure 7.1.1.1-1: Predicted stress contributions under simple tension for formula EAS-155-115 in the soft state

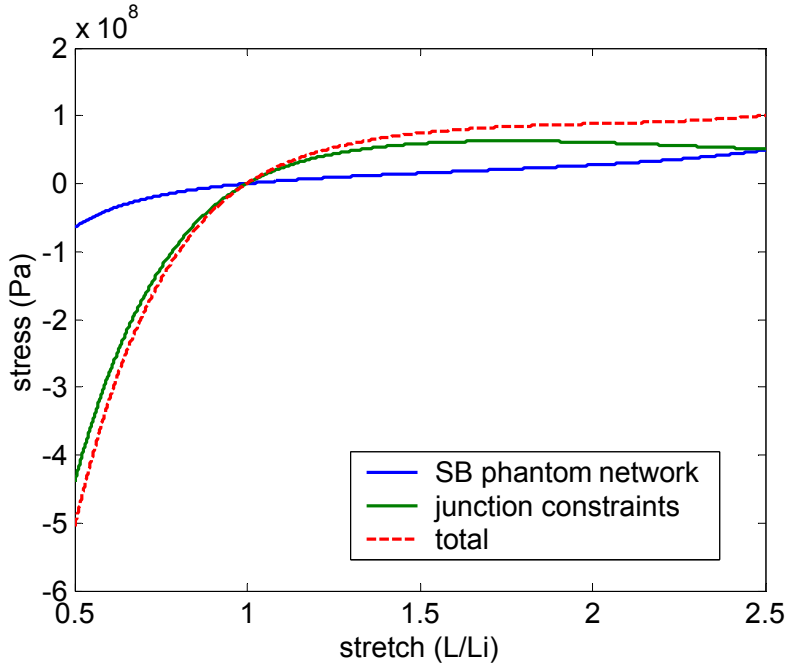

Figure 7.1.1.1-2: Predicted stress contributions under simple tension for formula EAS-155-115 in the hard state

Table 7.1.1.1-1: Junction constraint theory predicted hard and soft state properties of formula EAS-155-115

	Soft State		Hard State	
	Young's Modulus	STDEV	Young's Modulus	STDEV
	MPa	MPa	MPa	MPa
Experimental	2.0	NA	11.4	NA
Chemical Kinetic Model	NA	NA	110	NA
Phantom Network	0.063	0.003	49.1	11.1
Junction Constraints	2.0	0.0	110.0	0.0

In Table 7.1.1.1-1, *Experimental* refers to the sample averaged Young's modulus obtained experimentally, *Chemical Kinetic Model* refers to the theoretical predicted maximum Young's modulus in the hard state, *Phantom Network* refers to the soft and hard state Young's moduli as predicted by RIS theory, and *Junction Constraints* refers to the soft and hard state Young's moduli predicted when the junction constraint theory is included. As can be seen, the Young's modulus of the polymer predicted including junction constraints coincides exactly with experiment. This is because the coefficients in Equation 4.5-28 and the junction constraint

correction factor are phenomenologically fit ensuring this result. Although the theoretical hard state modulus predicted by the chemical kinetic model is believed to be an overestimate since it assumes that all possible photo-crosslinks are formed; the junction constraint model is calibrated to coincide with the chemical kinetic model for demonstrative purposes highlighting the versatility of the theory.

Figures 7.1.1.1-3 and 4 below compare the experimentally determined sample averaged stress response of the polymer to that predicted by junction constraint theory and RIS theory for both the hard and soft states. In the soft state, the junction constraint theory predicted stress response precisely matches the experimentally measured stress response. This is expected since in the soft state, the stiffness of the polymer is uniform through the thickness of the sample. In the hard case, however, the through thickness distribution of the stiffness of the polymer is non-uniform, resulting in the averaged measured stress being lower than that of the incident surface layer of the sample. Since the junction constraint theory presented simulates only a single polymer chain, and thus is incapable of any through thickness stiffness distribution, the Young's modulus predicted by junction constraint theory is phenomenologically fit to the theoretical single chain Young's modulus of the chemical kinetic model, which as seen in Figure 7.1.1.1-4 is significantly higher than the sample averaged stiffness measured experimentally.

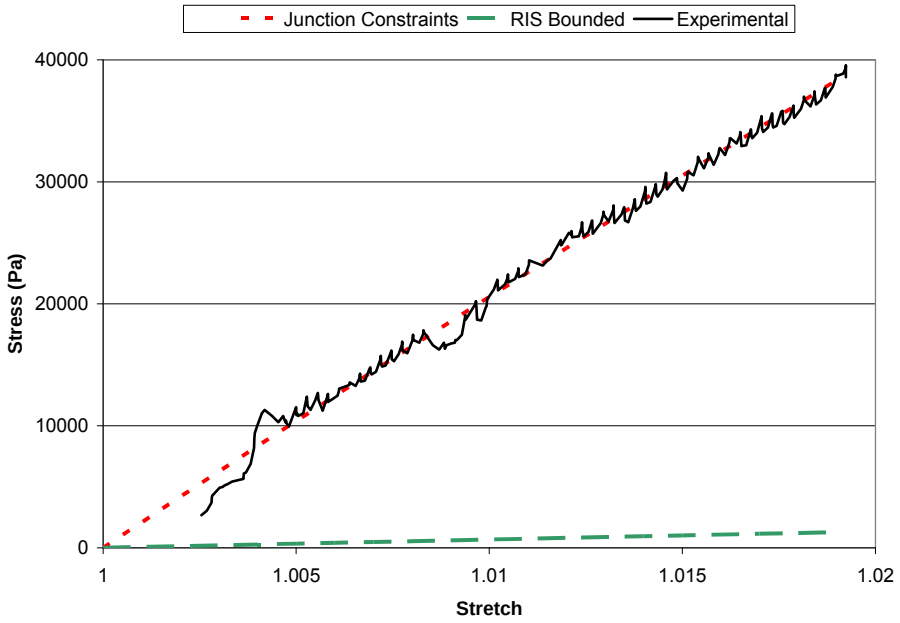

Figure 7.1.1.1-3: Comparison between experiment and predicted RIS model stress response of formula EAS-155-115 in the soft state

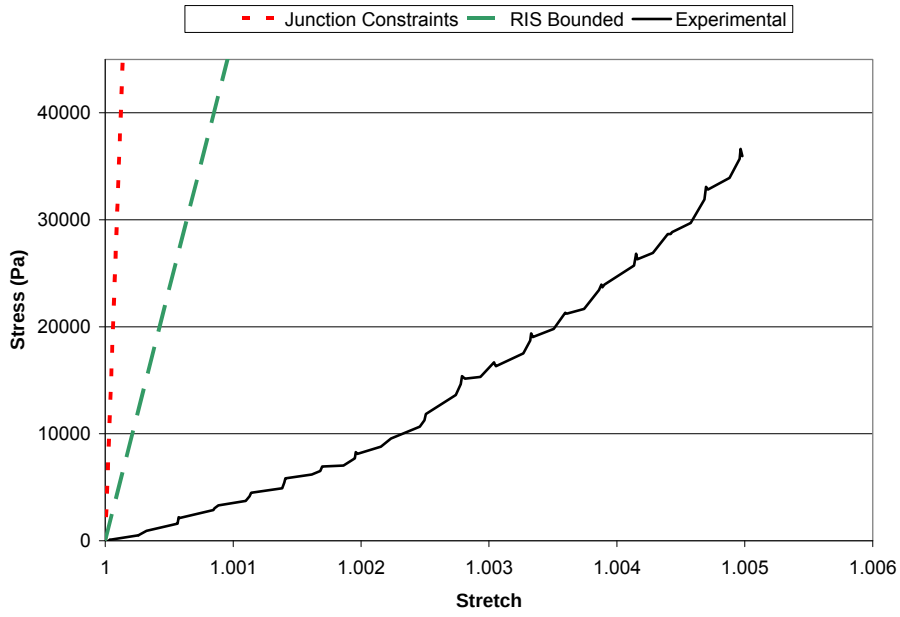

Figure 7.1.1.1-4: Comparison between experiment and predicted RIS model stress response of formula EAS-155-115 in the hard state

7.1.1.2 Formula EAS-155-93 Tensile Test Results

Pictured below in Figures 7.1.1.2-1 and 7.1.1.2-2 are the stress strain predictions for formula EAS-155-93 under simple tension. As can be seen, the predicted stresses for formula 93 are much higher than that of formula 115, correlating with the higher modulus predictions listed in Table 7.1.1.2-1.

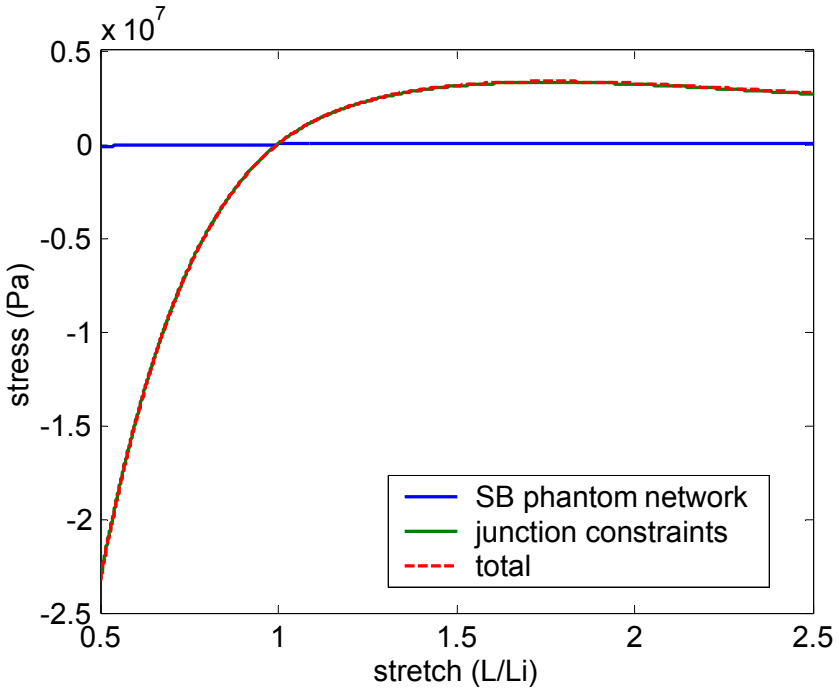

Figure 7.1.1.2-1: Predicted stress contributions under simple tension for formula EAS-155-93 in the soft state

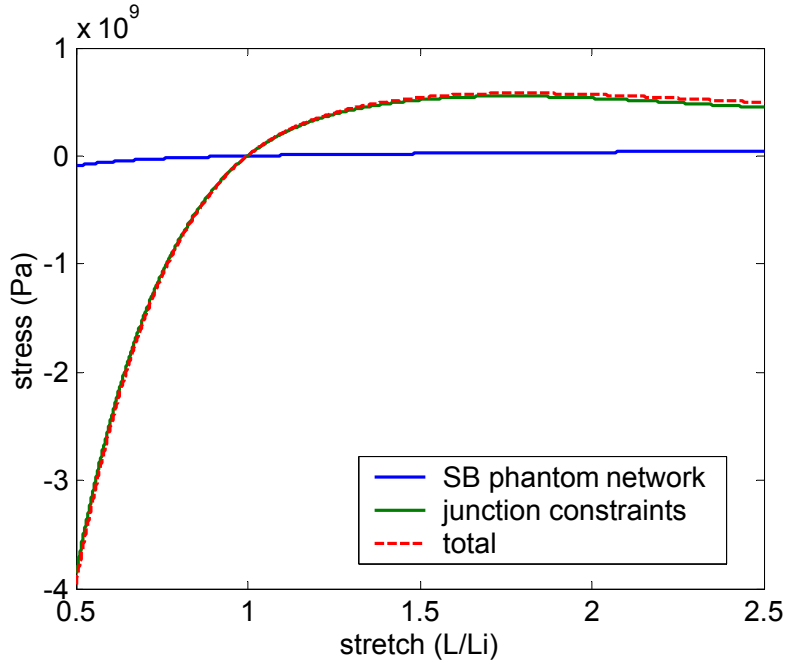

Figure 7.1.1.2-2: Predicted stress contributions under simple tension for formula EAS-155-93 in the hard state

Table 7.1.1.2-1: Junction constraint theory predicted hard and soft state properties of formula EAS-155-93

	Soft State		Hard State	
	Young's Modulus	STDEV	Young's Modulus	STDEV
	MPa	MPa	MPa	MPa
Experimental	5.0	NA	107	NA
Chemical Kinetic Model	NA	NA	850.0	NA
Phantom Network	0.080	0.006	65.1	15.1
Junction Constraints	5.0	0.0	850.0	0.0

Figures 7.1.1.2-3 and 4 below compare the experimentally determined sample averaged stress response of the polymer to that predicted by junction constraint theory and RIS theory for both the hard and soft states. As with formula EAS-155-115, the junction constraint theory predicted stress response matches the experimentally measured stress response in the soft state, with the exception of the region below a stretch of 1.008 due to slack in the sample during testing. Although in Figure 7.1.1.2-4 it appears that the RIS method captures the correct slope of the curve in the hard state, the two cannot be directly compared because the experimental curve is a

sample average with a non-uniform distribution of stiffness through the thickness of the sample while the RIS predicted stress response is for a single phantom network chain. Also as with Figure 7.1.1.2-3, the stress below a stretch of 1.001 is due to slack in the sample.

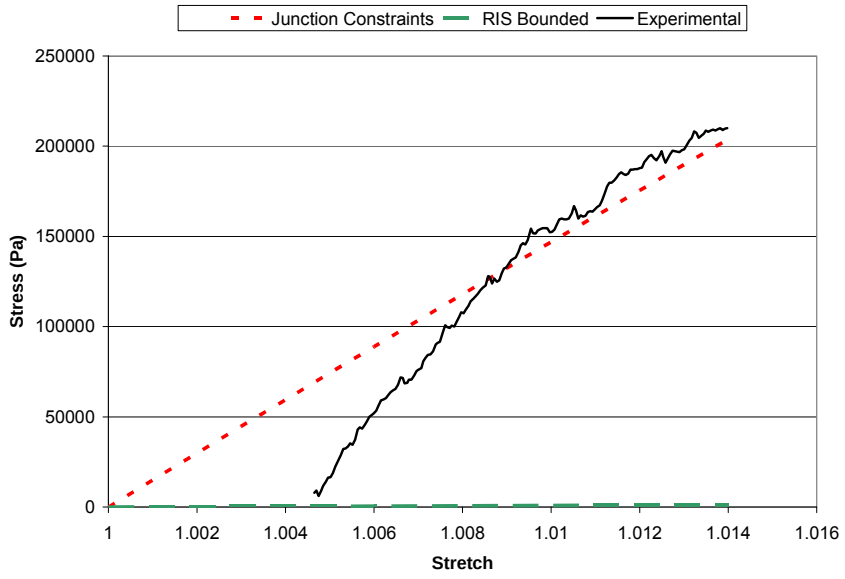

Figure 7.1.1.2-3: Comparison between experiment and predicted RIS model stress response of formula EAS-155-93 in the soft state

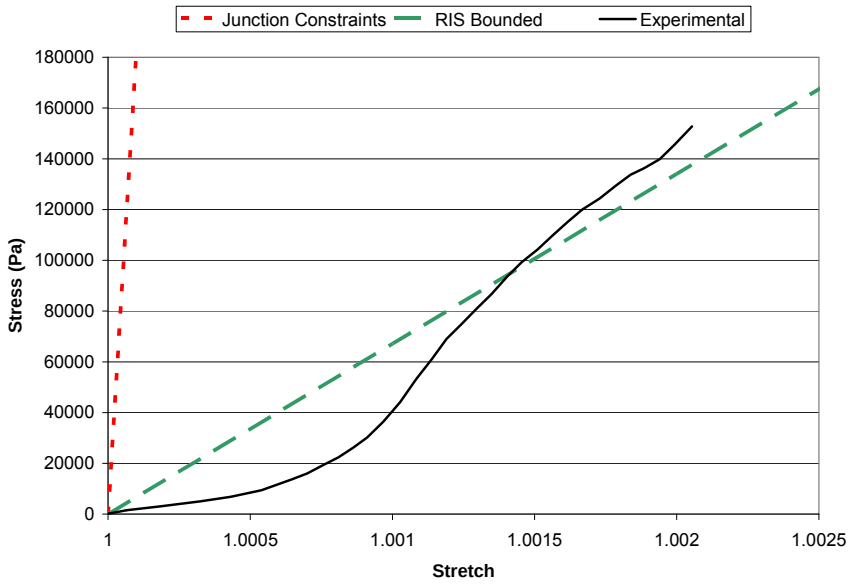

Figure 7.1.1.2-4: Comparison between experiment and predicted RIS model stress response of formula EAS-155-93 in the hard state

7.1.1.3 Formula EAS-155-143 Tensile Test Results

Pictured below in Figures 7.1.1.3-1 through 7.1.1.3-3 are the stress strain predictions for formula EAS-155-143 under simple tension. As described earlier, there is no reliable experimental data available for formula EAS-155-143 in the hard state. Thus to estimate the hard state modulus of the formula 143, the junction constraint correction factor is estimated based on the ratio of the junction constraint correction factor in the hard and soft states for formulas EAS-155-93 and EAS-155-115 and the correction factor for formula 143 in the soft state. The resulting correction factors used are listed in Table 7.1-2.

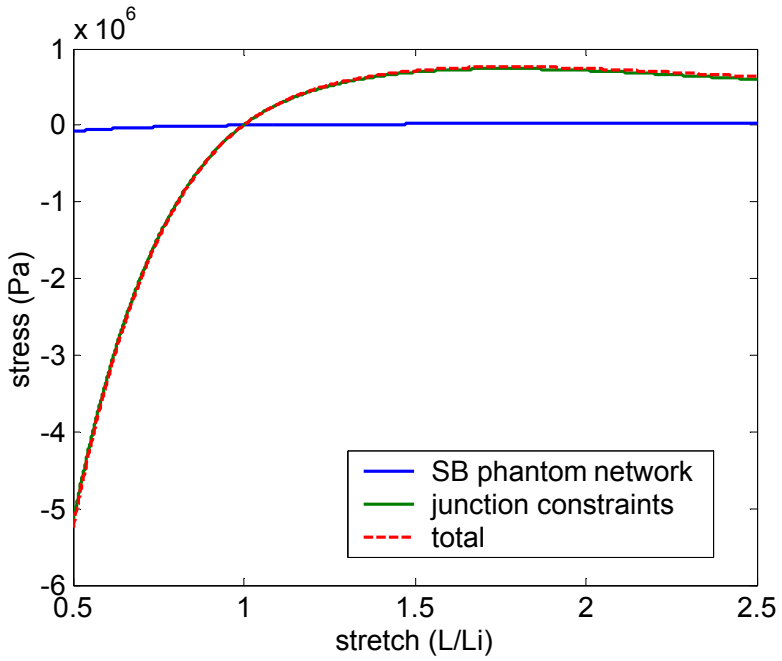

Figure 7.1.1.3-1: Predicted stress contributions under simple tension for formula EAS-155-143 in the soft state

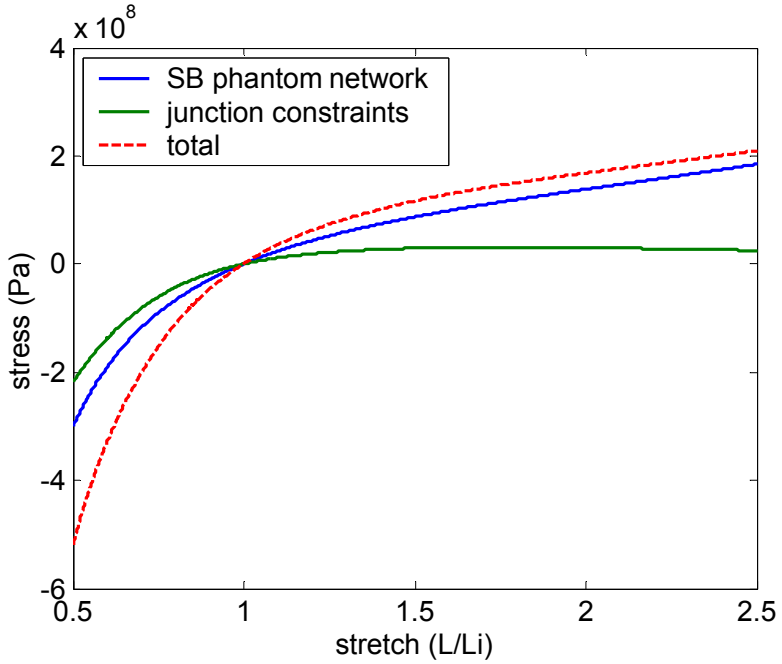

Figure 7.1.1.3-2: Predicted stress contributions under simple tension for formula EAS-155-143 in the hard state using formula 93 ratio

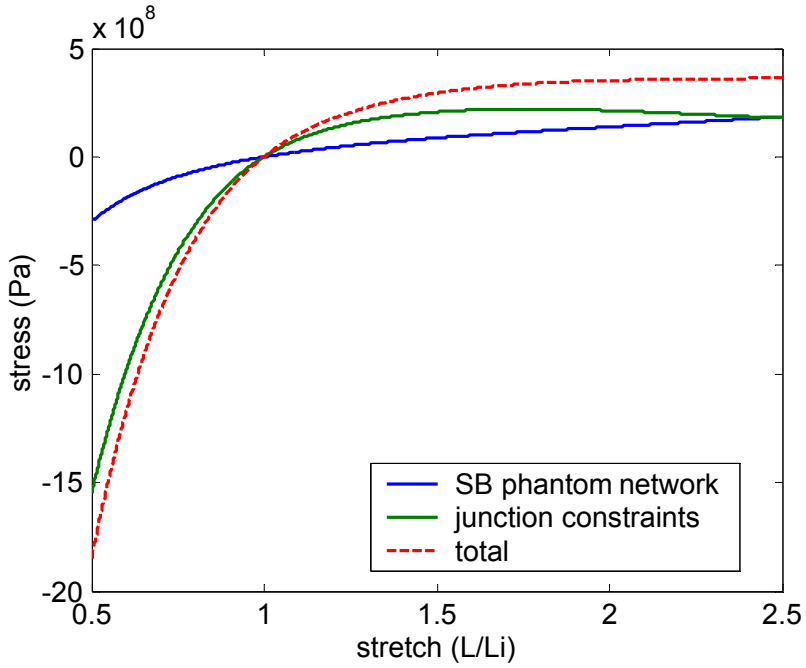

Figure 7.1.1.3-3: Predicted stress contributions under simple tension for formula EAS-155-143 in the hard state using formula 115 ratio

Table 7.1.1.3-1: Junction constraint theory predicted hard and soft state properties of formula EAS-155-143

	Soft State		Hard State	
	Young's Modulus	STDEV	Young's Modulus	STDEV
	MPa	MPa	MPa	MPa
Experimental	1.1	NA	NA	NA
Chemical Kinetic Model	NA	NA	NA	NA
Phantom Network	0.06	0.002	232	82
Junction Constraints 93 ratio	1.1	0.0	124	27
Junction Constraints 115 ratio			318	770

There are more photo crosslink locations in formula 143, every 4th segment, than are in either formula 115, every 4.7th segment, or formula 93, every 7th segment. Formula 143 also has the smallest average *r*-value of the three modeled formulas in the hard state. It would be expected, then, that formula 143 would have the highest Young's modulus of the three in the hard state. This is not the case, however, as the predicted hard state Young's modulus of formula 143 using the correction factor calculated from formula 93 is lower than the predicted Young's modulus of formula 93. This results in the conclusion that formulas 93, 115, and 143 are not sufficiently similar enough for the use of a single junction constraint correction factors universally applied to all three formulas. This conclusion is further justified by recognizing that junction constraint theory is based on the assumption that the distribution of fluctuations in the chain caused by entanglements are Gaussian in nature, however it is well known that this is not the case [106,110]. For these reasons, junction constraint model results for Formula EAS-155-143 in the equi-biaxial and shear strain states is located in Appendix B, as the predictions may offer insight into the modeling methodology, but are unlikely to be physically accurate.

7.1.2 JC Model Equi-biaxial Test Results

7.1.2.1 Formula EAS-155-115 Equi-biaxial Test Results

Pictured below in Figures 7.1.2.1-1 and 7.1.2.1-2 are the stress predictions for formula EAS-155-115 under equi-biaxial strain. Equi-biaxial strain is modeled using the quantities listed in Table 4.4-1.

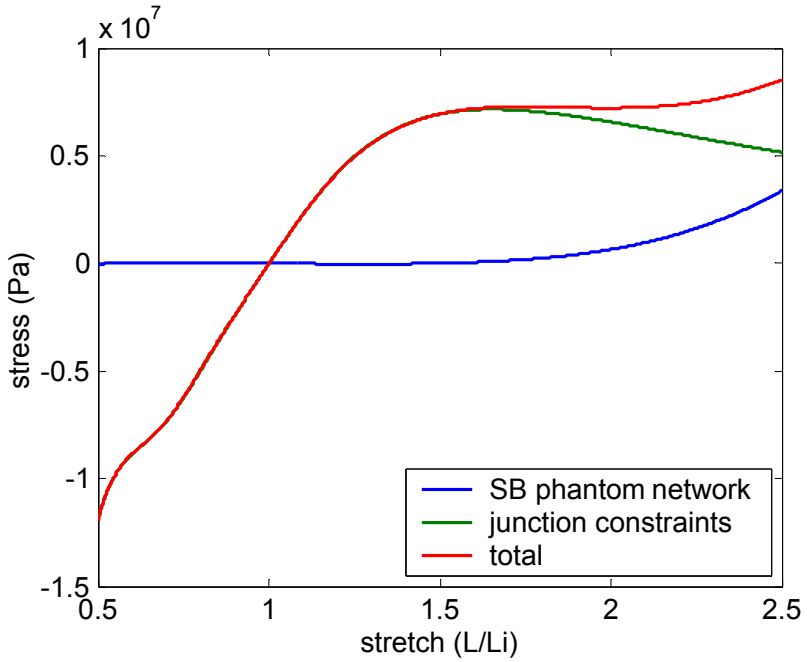

Figure 7.1.2.1-1: Predicted stress contributions under equi-biaxial strain for formula EAS-155-115 in the soft state

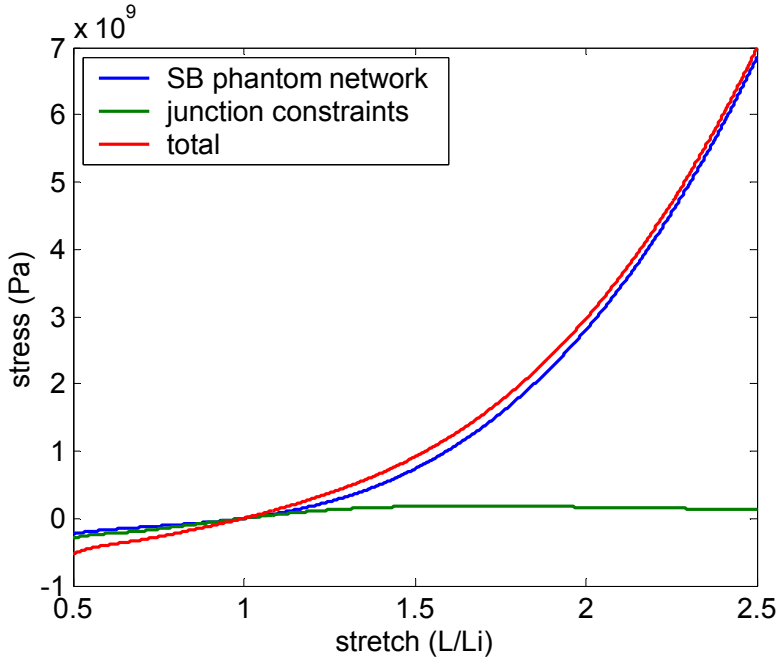

Figure 7.1.2.1-2: Predicted stress contributions under equi-biaxial strain for formula EAS-155-115 in the hard state

Table 7.1.2.1-1: Junction constraint theory predicted hard and soft state properties of formula EAS-155-115 under equi-biaxial strain

	Biaxial Modulus SB MPa	STDEV MPa
Soft State	8.0	0.0
Hard State	422	5.6

The biaxial modulus reported in Table 7.1.2.1-1 is calculated with Equation 4.4-8 using the stress and strain in the primary direction using the Johnson bounded distribution. Equi-biaxial experimental data for LASMP is unavailable at this time, thus the presented data is offered as an example of how the model can be used to predict material properties without the need for experiment.

7.1.2.2 Formula EAS-155-93 Equi-biaxial Test Results

Pictured below in Figures 7.1.2.2-1 and 7.1.2.2-2 are the stress predictions for formula EAS-155-93 under equi-biaxial strain.

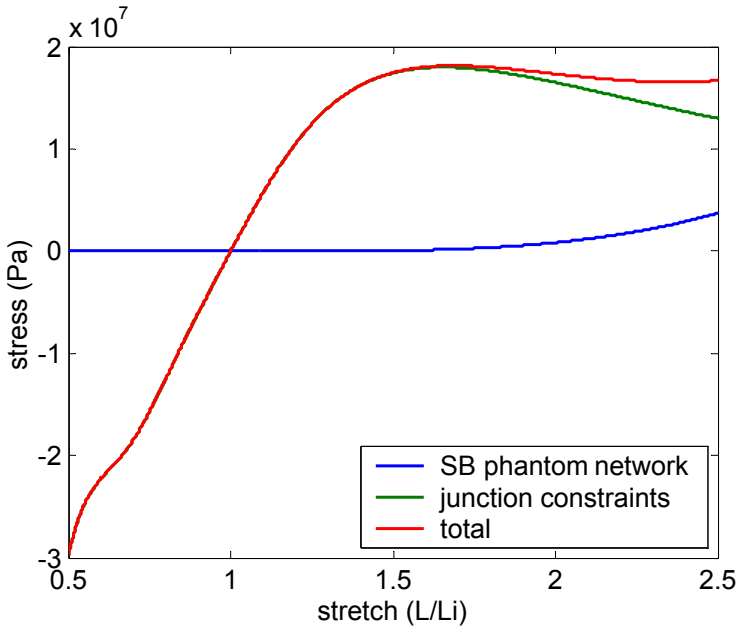

Figure 7.1.2.2-1: Predicted stress contributions under equi-biaxial strain for formula EAS-155-93 in the soft state

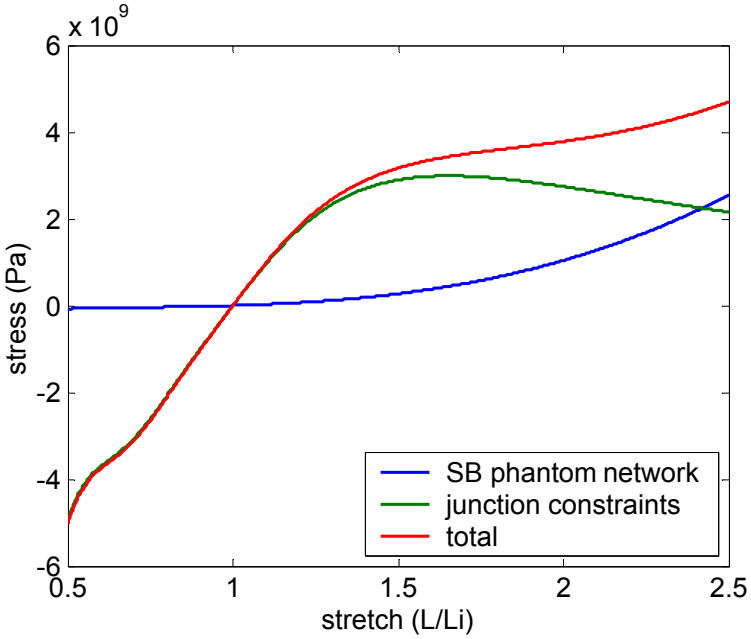

Figure 7.1.2.2-2: Predicted stress contributions under equi-biaxial strain for formula EAS-155-93 in the hard state

Table 7.1.2.2-1: Junction constraint theory predicted hard and soft state properties of formula EAS-155-93 under equi-biaxial strain

	Biaxial Modulus SB MPa	STDEV MPa
Soft State	20	0.0
Hard State	3380	2.7

Although the magnitudes of the ultimate stresses predicted under biaxial strain for formulas 115 and 93 are similar, the predicted biaxial modulus of formula 93 in the hard state is much higher. The proportional difference in biaxial modulus between formulas 93 and 115, however, is in agreement with the proportional difference in Young's modulus between the two formulas.

7.1.3 JC Model Shear Test Results

Presented below are results of the junction constraint theory model under shear using the quantities listed in Table 4.4-1. The shear modulus is calculated using Equation 7.1.3-1 [106].

$$f_1 = G\left(\lambda_1 - \frac{1}{\lambda_1^3}\right) \tag{7.1.3-1}$$

Where f_1 is the stress in the primary direction, G is the shear modulus, and λ_1 is the stretch in the primary direction.

7.1.3.1 Formula EAS-155-115 Shear Test Results

Pictured below in Figures 7.1.3.1-1 and 7.1.3.1-2 are the stress predictions for formula EAS-155-115 under shear. Table 7.1.3.1-1 lists the predicted shear moduli in the hard and soft states using the Johnson bounded distribution.

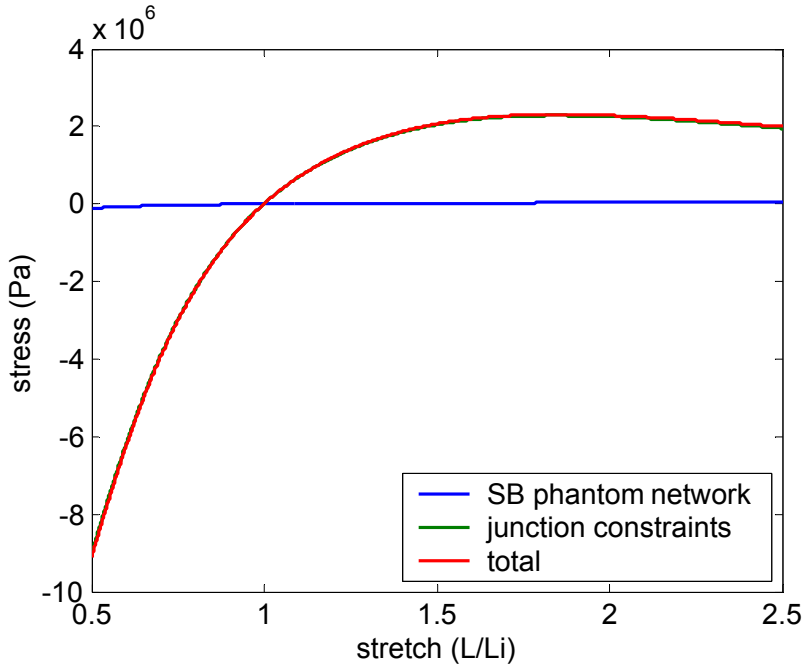

Figure 7.1.3.1-1: Predicted stress contributions under shear strain for formula EAS-155-115 in the soft state

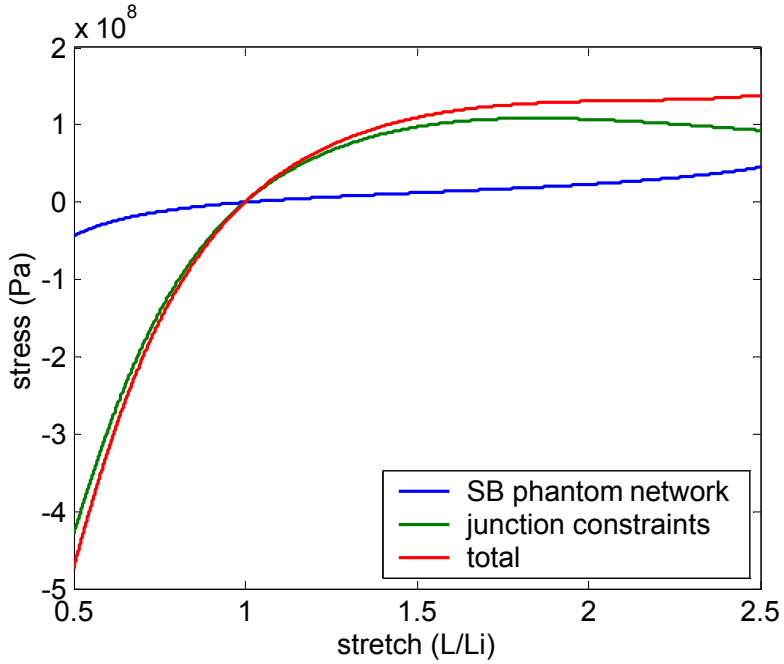

Figure 7.1.3.1-2: Predicted stress contributions under shear strain for formula EAS-155-115 in the hard state

Table 7.1.3.1-1: Junction constraint theory predicted hard and soft state properties of formula EAS-155-115 under shear

	Shear Modulus SB MPa	STDEV MPa
Soft State	1.2	0.0
Hard State	52	9.7

7.1.3.2 Formula EAS-155-93 Shear Test Results

Pictured below in Figures 7.1.3.2-1 and 7.1.3.2-2 are the stress predictions for formula EAS-155-93 under shear. Table 7.1.3.2-1 lists the predicted shear moduli in the hard and soft states using the Johnson bounded distribution.

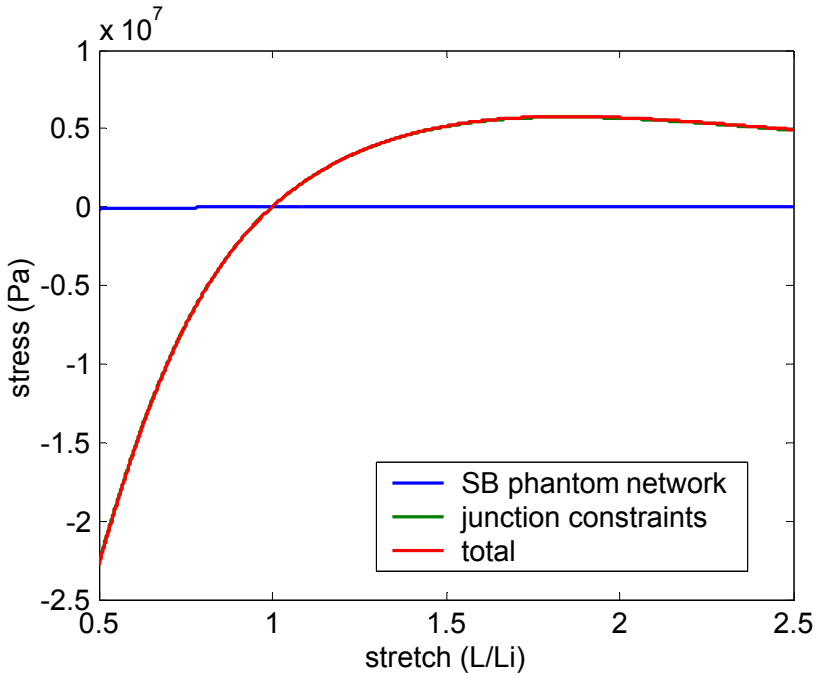

Figure 7.1.3.2-1: Predicted stress contributions under shear strain for formula EAS-155-93 in the soft state

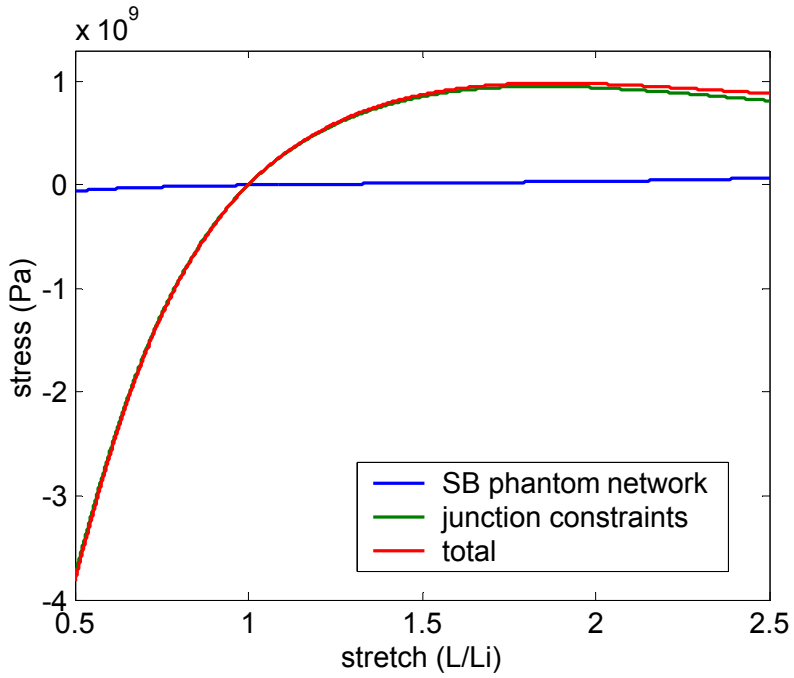

Figure 7.1.3.2-2: Predicted stress contributions under shear strain for formula EAS-155-93 in the hard state

Table 7.1.3.2-1: Junction constraint theory predicted hard and soft state properties of formula EAS-155-93 under shear

	Shear Modulus SB MPa	STDEV MPa
Soft State	3.0	0.0
Hard State	509	1.8

As can be seen from Table 7.1.3.2-1 and is expected, the predicted shear modulus of formula 93 is much higher than that predicted for formula 115 in both the hard and soft states.

7.2 JUNCTION CONSTRAINT MODEL CONCLUSIONS

Table 7.2-1: Junction constraint model Young's, biaxial, and shear modulus predictions

		Phantom Network		Junction Constraint Theory	
Strain State	Formula	Soft State	Hard State	Soft State	Hard State
Tensile	115 (MPa)	0.06	50	2.0	110
	93 (MPa)	0.08	65	5.0	850
Equi-biaxial	115 (MPa)	NA	NA	7.9	422
	93 (MPa)	NA	NA	19.8	3384
Shear	115 (MPa)	NA	NA	1.2	52
	93 (MPa)	NA	NA	3.0	509

As highlighted by the distribution of junction constraint correction factors in Table 7.1-2, junction constraint theory is ill-suited for predictive applications. It is however, capable of being calibrated for a specific formula allowing the modeling of alternative loading scenarios, making it useful for design purposes. This of course does not exclude the theory from being utilized to model other LASMP formulas that are more similar in molecular structure than the formulas presented. As well as the quantities shown above, other material response characteristics may also be calculated using the presented method and data, further enhancing the model's usefulness for design.

8.0 FUTURE RESEARCH

While the presented research is a promising start to both the realization of a commercially available light activated shape memory polymer as well as a refined model methodology for predicting macroscopic response of proposed polymer systems based on microscopic parameters, there is much work to be done. The viability of the polymer in real applications remains untested. Material properties such as fatigue, creep, crack growth resistance, oxidation, damage to the backbone due to optical irradiation, and others need to be quantified for the polymer to be implemented in applications. Novel activation schemes, while proposed and theoretically viable, also remain untested. Other factors such as manufacturing techniques, cost of production, and life cycle analysis are also issues facing the introduction of any new material.

Further research is also needed to refine the proposed model. While the model is designed and presented to be modular in nature with the ability to replace any given step, actually replacing the theories presented with alternative methods has not been tried and thus the limits of doing so are unknown. The effect of complex data, such as a bimodal distribution of *r*-values, on the accuracy of the method is also unknown. The method is theoretically capable of predicting other quantities derivable from the stress strain curve, provided sufficient accuracy regarding the coefficients used in the junction constraint theory such as yield and ultimate stresses. This capability would provide a powerful tool and enable the model to be used with material design software such as ABAQUS, but has to date not been attempted. The two models

presented, the chemical kinetic model and the RIS model, also have the ability to be integrated resulting in a more detailed prediction of the evolution of Young's modulus. The chemical kinetic model can be used to predict the degree and depth of crosslinking given a dose of radiation which can then be used by the RIS model predicting the through thickness and sample averaged stiffness of polymers not available for experimental characterization.

As an alternative to the methods described above using statistical mechanics to calculate the change in entropy of the polymer chain with respect to strain, yielding the stress response of the polymer, molecular dynamics (MD) can also be used to model the polymer and predict macroscopic material properties based on the molecular structure. The presented study uses the Large-scale Atomic/Molecular Massively Parallel Simulator (LAMMPS), developed and made available by Sandia National Laboratories and is a readily downloadable application used to model interatomic interactions [113,115,116].

8.1 LAMMPS MODELING

The atomic coordinates for the atoms included in the MD simulation are determined as with the previous method using RIS theory. The bond potentials, in plane bond angles, and dihedral potentials are the same as previously determined. To model the polymer in either state, only a section of atoms between two crosslinks is included in the simulation. This results in the simulation of formula EAS-155-115 including 91 "atoms" when modeling the polymer in the soft state and 7 "atoms" in the hard state. Because the exact molecular structure is proprietary, the polymer is modeled in LAMMPS as if the grained segments of the polymer, as described previously, where individual atoms with all of the information to model the polymer (bond

lengths, bond potentials, in plane angles and potentials, and rotational dihedral angles and potentials) known for the included molecules.

Since MD simulations are not the intention of this work, the following is only a brief outline of the method used. The three dimensional simulation uses "real" units, "full" atom style, and a non-periodic shrink-wrapped "s s s" boundary. The bond potential between two molecules is modeled using the Lennard Jones potential with coulombic interactions with the inner and outer global switching cutoffs for the Lennard Jones potential set as 1.0 and 45.2. The outer cutoff is significantly larger than expected because the "atoms" in the simulation represent molecules. The optional coulombic interaction coefficients are neglected and the pair coefficients are set to 0.0. This essentially turns off pair potentials, rendering the above moot, while preventing the molecules from interacting with each other in any way not explicitly stated in the input file. This is needed because the model includes only a single polymer chain. If general interactions are allowed, the chain, upon executing an energy minimization, will coil onto itself since it is unrestricted. In a real polymer, however, this is prevented by physical entanglements with neighboring chains. Because modeling several polymer chains is computationally prohibitive, the pair coefficients are set to 0.0 and any bond potentials explicitly described. The potential must be included however to prevent the program from terminating early with an error stating the potential is missing. The Lennard Jones potential and coulomb interaction equations used are presented below in Equations 8.1-1.

$$LJ(r) = 4\varepsilon\left[\left(\frac{\sigma}{r}\right)^{12} - \left(\frac{\sigma}{r}\right)^{6}\right]$$
$$C(r) = \frac{Cq_i q_j}{\varepsilon r} \tag{8.1-1}$$

The harmonic bond style is used in the simulation, described by Equation 8.1-2 below, and serves as the criteria describing bond length. There are six possible bond lengths in the simulated polymer with the following coefficients.

Table 8.1-1: Bond style coefficients

Bonded Molecules	K (energy/dist^2)	r_0 (distance)
Omega to Sigma	100	3.77198
Pie to Sigma	100	3.77198
PKP to Sigma	100	3.77198
Sigma to Omega	100	45.183
Sigma to Pie	100	24.1669
Sigma to PKP	100	3.61159

$$E = K\left(r - r_0\right)^2 \tag{8.1-2}$$

The names given to the molecules in column 1 of Table 8.1-1 are the same as those used to describe the molecular structure of the polymer in Chapter 4. These coefficients result in the bond potentials seen below in Figure 8.1-1.

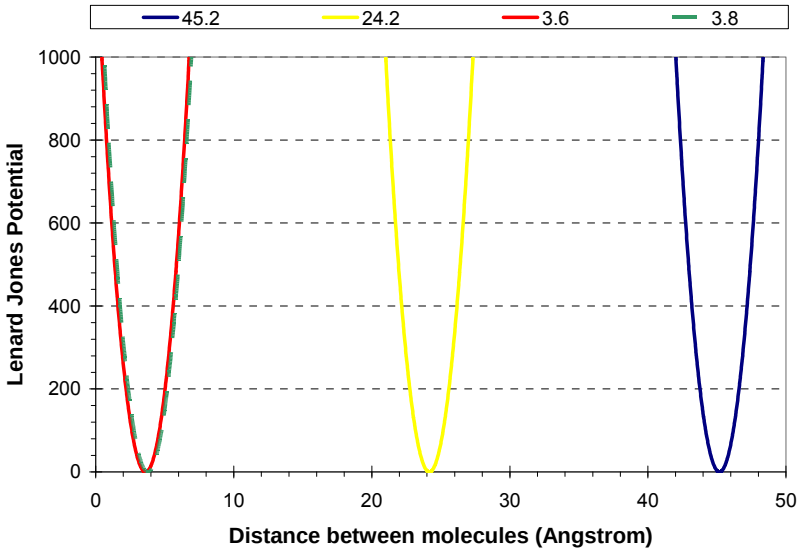

Figure 8.1-1: Bond potentials

The minimum energy locations, r_0 in Table 8.1-1, represent the calculated bond lengths of the different bonds using RIS theory with the in plane angle between each pair of molecules being 111 degrees, as presented in Chapter 4. The harmonic angle style is used with coefficients of 1000 energy/radian^2 and 111 degrees, representing K and Θ_0 respectively, seen below in Equation 8.1-3.

$$E = K(\theta - \theta_0)^2 \tag{8.1-3}$$

The exact magnitude of K is not known, although it is assumed that rotation about a bond is the chief mechanism of deformation, thus the coefficient of K describing the in plane angle is given a relatively large value. A graph of the in plane angle potential is shown below in Figure 8.1-2.

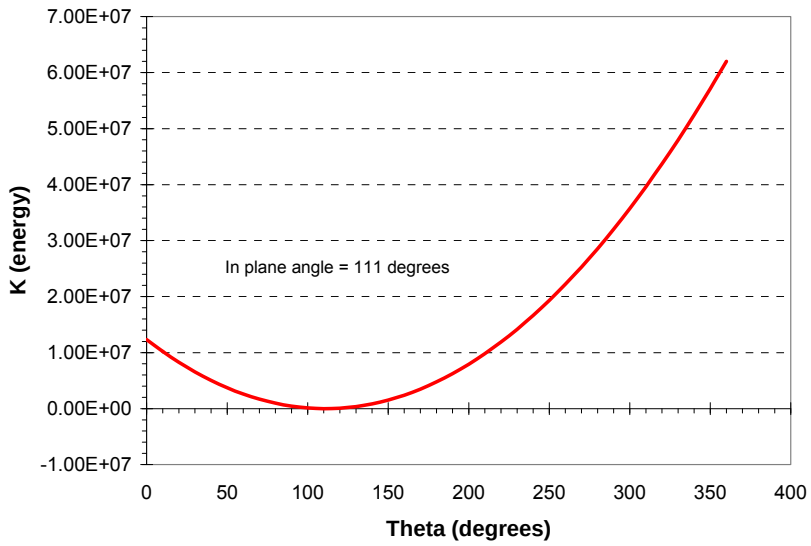

Figure 8.1-2: In plane angle bond potential

The charmm potential is used to describe the rotational dihedral bond angles of the simulated polymer, shown below in Equation 8.1-4.

$$E = K\left[1 + \cos\left(n\phi - d\right)\right] \tag{8.1-4}$$

A value of 1500 is assigned to K in Equation 8.1-4 for all dihedral angles. Figure 8.1-3, below, is the shows a select few of the calculated dihedral angle potentials.

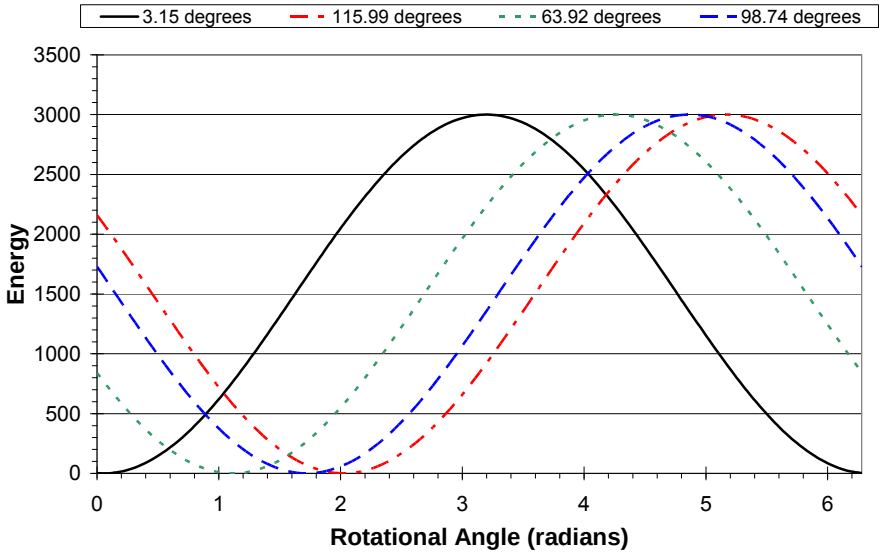

Figure 8.1-3: Rotational dihedral potentials

Finally, the bonds, angles, and dihedrals and their associated molecules are listed in the input file and random initial velocities prescribed to all molecules.

The first and last atoms in the chain are identified forces applied during the simulation. An "nvt" command equalizing the temperature at 300K, the force increased incrementally, and the positions of the atoms output until the simulation fails.

8.2 RESULTS AND EXPERIMENTAL COMPARISON

In the soft state, the initial conformation in LAMMPS, after the temperature is equilibrated and the simulation minimized, is shown below in Figure 8.2-1.

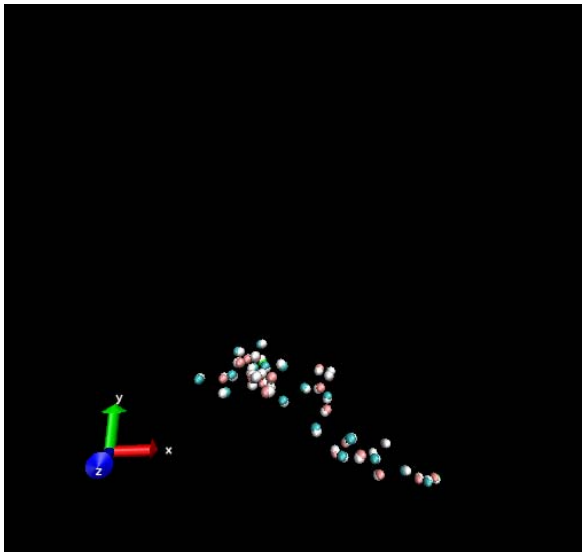

Figure 8.2-1: LASMP conformation in the soft state

Approximately half way through the simulation the polymer chain has been strained approximately 218% with a force of 27 Pa, and is pictured below in Figure 8.2-2.

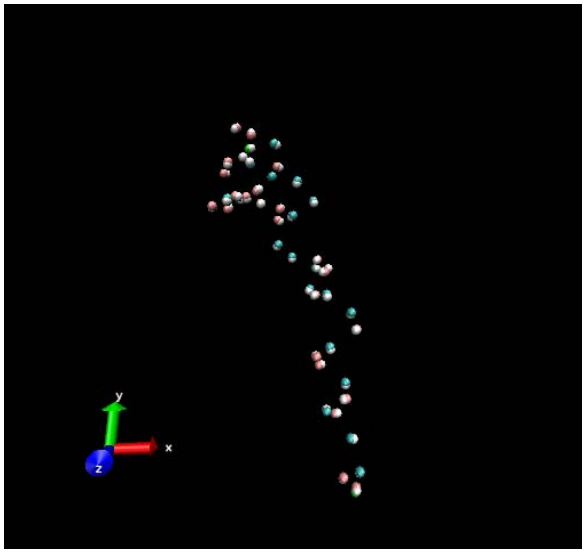

Figure 8.2-2: LASMP in the soft state approximately half way through the simulation

The simulation fails after approximately 110 steps at a final strain of 380% at a force of over 60 Pa. The final step is shown below in Figure 8.2-3.

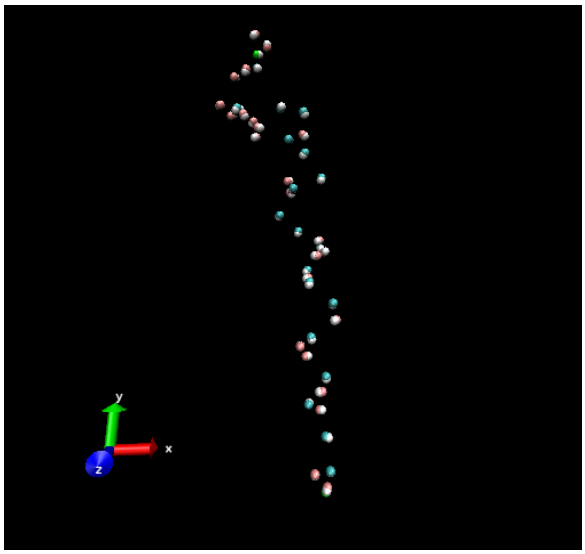

Figure 8.2-3: LASMP in the soft state just before simulation failure

The soft state simulation of the polymer yielded a Young's modulus of 9.7 Pa, as seen below in Figure 8.2-4, and predicts the polymer to be highly elastic.

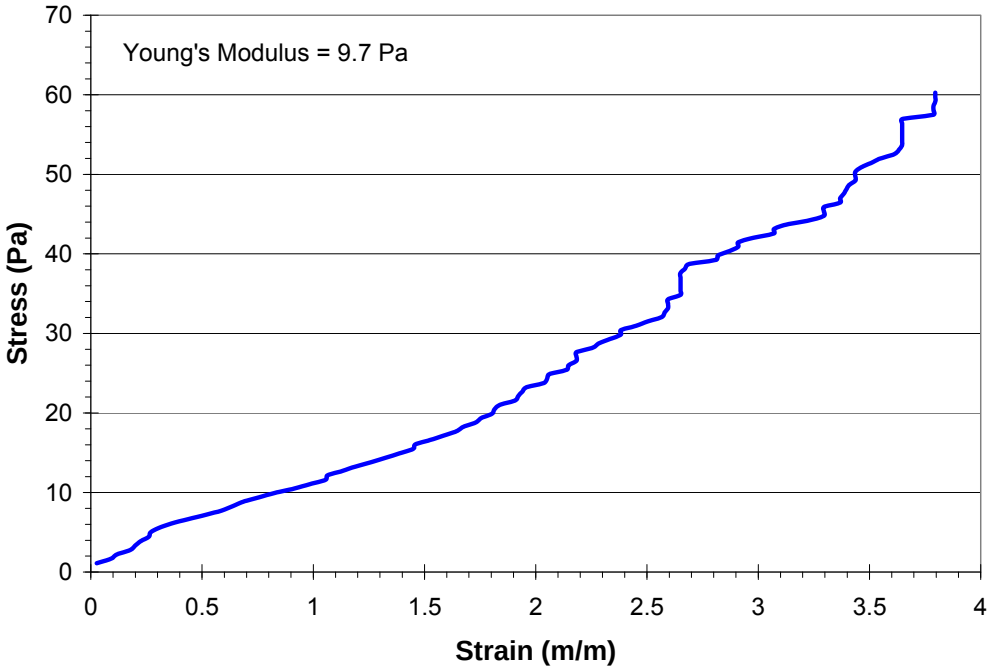

Figure 8.2-4: Constitutive response predicted by LAMMPS for LASMP in the soft state

In the hard state, the polymer has much fewer molecules between crosslinks and is thus much shorter. The initial conformation after thermal equilibration and simulation minimization for the hard state simulation is pictured below in Figure 8.2-5.

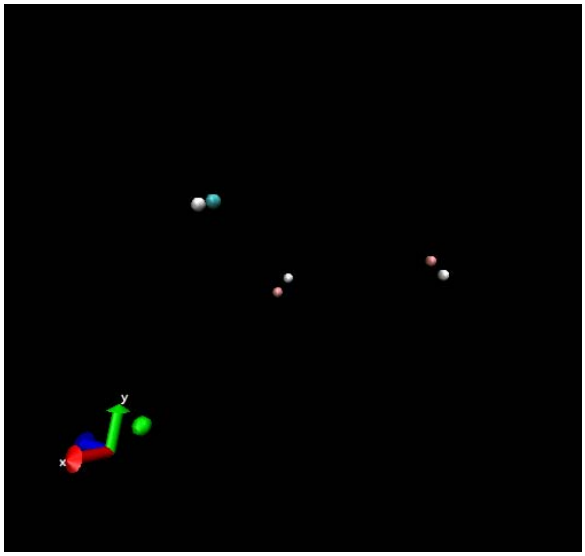

Figure 8.2-5: Hard state initial conformation

As can be seen, the molecules appear to be uncharacteristically far from one another, this is however expected due to the nature of the simulation and the zoom required so that the entire frame is utilized. Approximately half way through the simulation, at step 55, the strain on the polymer is 270% with an applied force of 29 Pa, shown below in Figure 8.2-6.

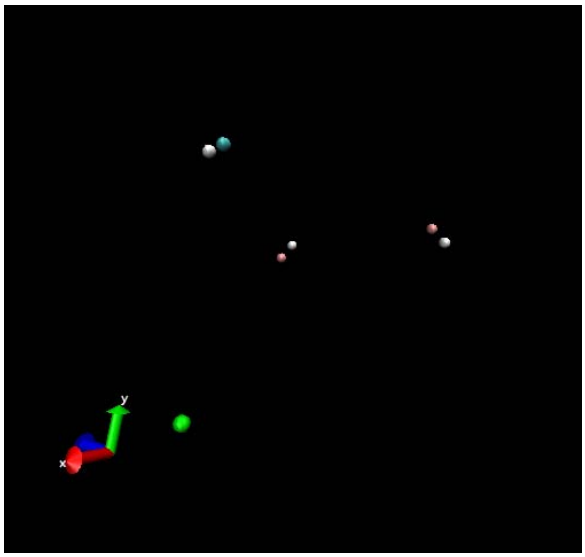

Figure 8.2-6: Step 55 simulating LASMP in the hard state using LAMMPS

The simulation fails after approximately 102 steps at a final strain of 365% at a force of over 56 Pa. The final step is shown below in Figure 8.2-7.

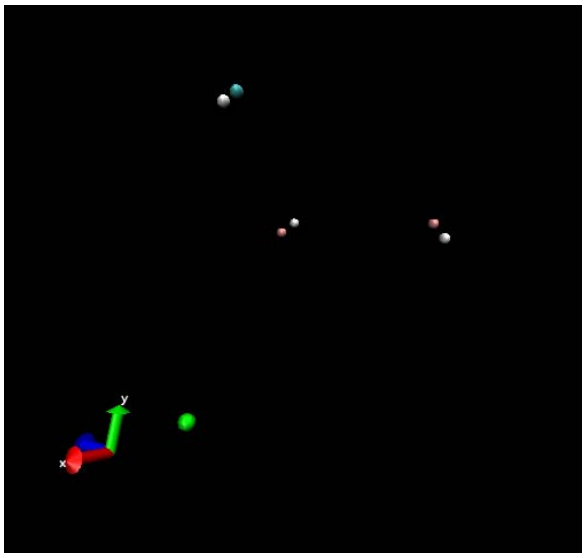

Figure 8.2-7: Final step before failure of LASMP in the hard state

The hard state simulation of the polymer yielded a Young's modulus of 28.2 Pa, as seen below in Figure 8.2-8, also showing the polymer to be highly elastic.

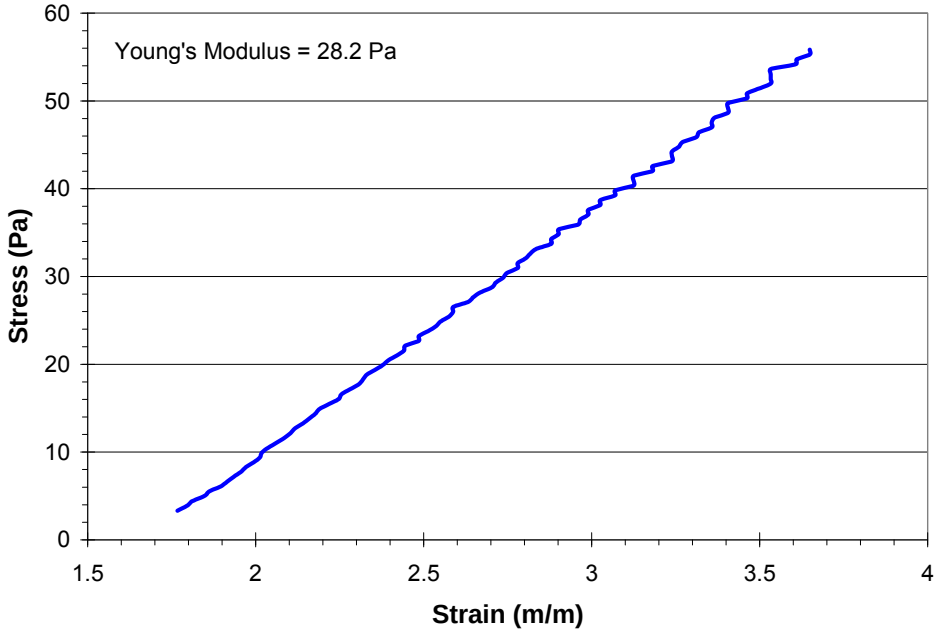

Figure 8.2-8: Constitutive response of LASMP in the hard state as predicted by LAMMPS

Below, Table 8.2-1 lists the experimentally determined Young's modulus and all of the predicted Young's moduli for each of the three simulation methods in both the hard and soft states of the polymer.

Table 8.2-1: Predicted Young's modulus comparison

	Young's Modulus soft (Pa)	Young's Modulus hard (Pa)
Experimental	$2.0*10^6$	$110.0*10^6$
Phantom Network Theory	$0.1*10^6$	$49.1*10^6$
Junction Constraint Theory	$2.0*10^6$	$110.0*10^6$
LAMMPS	9.7	22.8

8.3 MOLECULAR DYNAMICS CONCLUSIONS

As can be seen from Table 8.2-1, the only method accurately predicting the nominal value of Young's modulus of the polymer is the statistical mechanics method when junction constraints are included. This method, however, requires that experimental results of a molecularly similar polymer are available to calibrate the model, which in some instances will not be the case. In contrast, neither the phantom network model nor the MD simulation using LAMMPS requires any knowledge of macroscopic material parameters prior to use. This provides a very useful tool in evaluating candidate material formulations of new polymers. Although the phantom network model is significantly more accurate, both can be used to qualitatively evaluate the relative properties of a polymeric material. Both the phantom network model and LAMMPS simulation accurately predict the hardening of the material with increased crosslinking due to optical stimulation.

The lower values of Young's modulus predicted by the LAMMPS simulation are believed to be due to several factors. First, there is error in the potentials themselves. The actual potentials are non-regular functions and require higher order approximations to model correctly. This results in misplaced, underestimated, and overestimated energy barriers for extension and rotation in the LAMMPS simulation. Improving the modeling of these potentials, though beyond the scope of the current work, should result in more accurate predictions. Also, in the current LAMMPS simulation, movement in the transverse directions to the applied force is unrestricted, resulting in a slight rotation of the polymer chain. In reality, neighboring chains in the polymer would hinder such rotation, increasing the strength of the polymer. Finally, the simulation, as with the phantom network model, does not take into account any physical entanglements or other interactions with neighboring chains. Theoretically it is possible to

model several chains using MD, however currently it is computationally unpractical. Each full polymer chain includes tens of thousands of molecules. To model neighboring chain interaction, hundreds of thousands of chains would need to be simulated so that edge and end effects would be accounted for. Such a large simulation would require computing power and computation run time that would negate the purpose of the project, which is to reduce the time required to determine the optimum formula of a given polymer for a specific application. Finally, the polymer chain modeled here is simply one conformation of the polymer. The number of molecules between crosslinks and their order vary greatly. The simulation presented here includes five molecules between the end points in the hard state. Statistically, however, there can be anywhere from 1 to 9 molecules between the endpoints. The distribution of which varies between polymer formulas. For a more accurate prediction of Young's modulus in the hard state, all of the possible conformations should be modeled and the resulting material properties condensed using a weighted average.

9.0 CONCLUSIONS

Several candidate formulas of light activated shape memory polymer have been experimentally characterized and their properties' dependence on optical stimulus defined. While the optimal formula is still under investigation, candidate formulations have proven that significant modulus change in a feasible amount of time is attainable. Reversible modulus changes of over 600% have been achieved in current formulas, opening the door to a wide range of applications. Having a power requirement of less than 1.5J/g, they are extremely attractive for applications requiring the ability to switch between two modulus states where power is restricted, such as space applications.

The presented method of building a polymer chain using rotational isomeric state theory, modeling the distribution of crosslink to crosslink distances, or *r*-values, using Johnson distributions, relating the conformational entropy to changes in stress due to strain with Boltzmann statistical mechanics and the three chain rule, and accounting for the stress due to interactions with neighboring chains using junction constraint theory has proven a valuable and accurate tool in evaluating the material properties of light activated shape memory polymer. The modular nature of the method allows the theory to be adapted to systems with varying behavior, such as a bimodal distribution of *r*-values. The phenomenological fitting nature of junction constraint theory yields nominally accurate Young's modulus predictions while also providing some customization of the stress strain curve, which in future studies may lead to accurate

predictions of such quantitative quantities as yield stress and ultimate stress as well as qualitative observations such as ductility. The method is well suited for evaluating the relative stiffness of proposed formulas, providing a valuable assessment in the continuing effort to optimize LASMP formula. It greatly decreases the time required for formula evaluation with respect to traditional experimental techniques and also provides an avenue to customer-tailored formulations in the future.

APPENDIX A

EXAMPLE POLYMER CHAIN CONFORMATIONS

The following graphs show example polymer chain conformations for formulas EAS-155-115, EAS-155-93, and EAS-155-143 in both the soft and hard states. The blue lines represent the polymer chain backbone and the red lines designate photo-crosslinkable locations. The hard state conformations comprise of approximately 10,000 crosslinks while the soft state conformations comprise of approximately 2000 crosslinks. As can be seen, the difference in crosslink density between the hard and soft states is clearly visible.

A.1 FORMULA EAS-155-115 SOFT STATE CONFORMATIONS

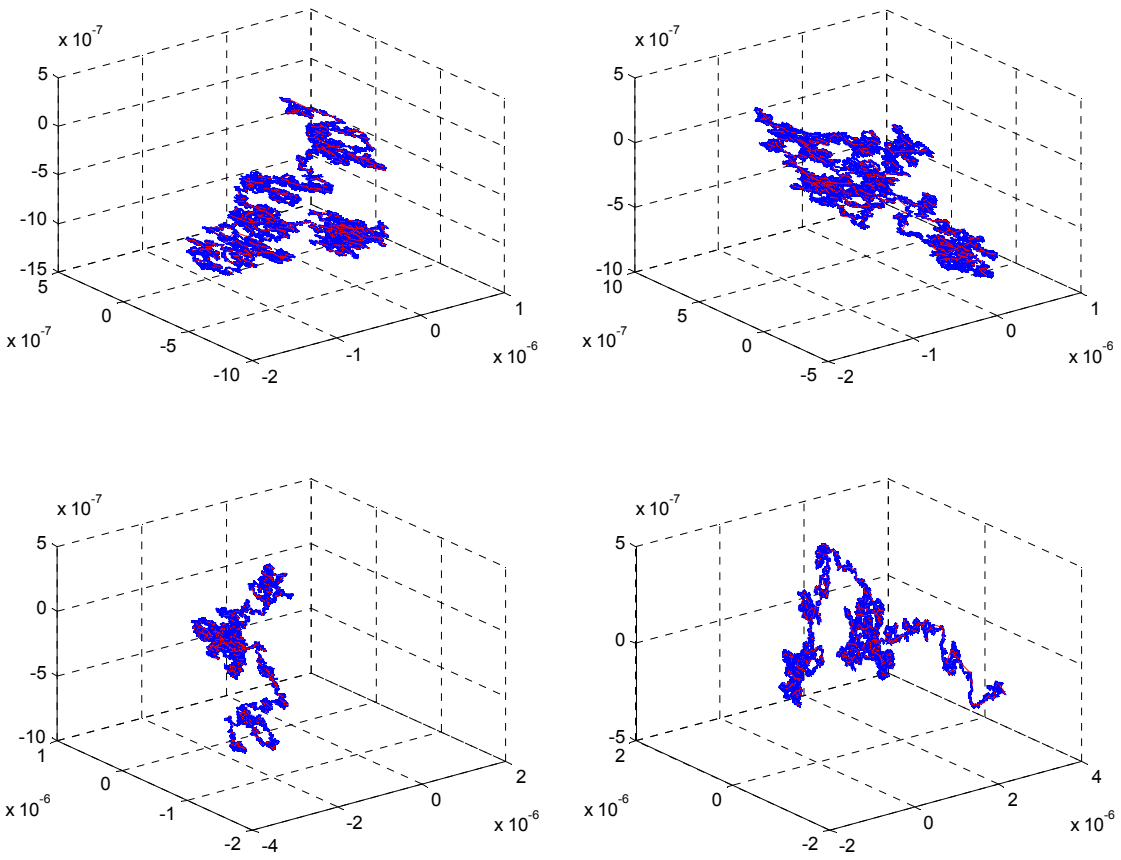

A.2 FORMULA EAS-155-115 HARD STATE CONFORMATIONS

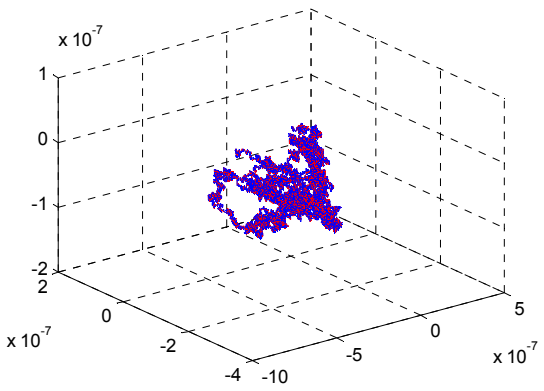

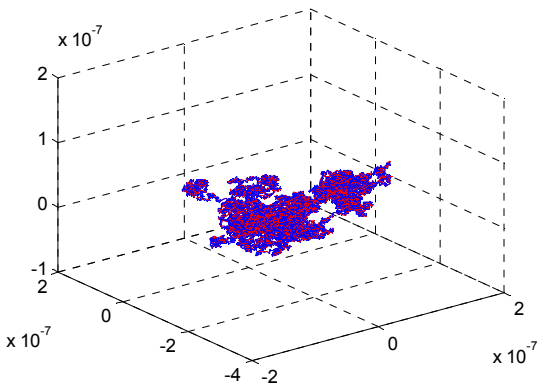

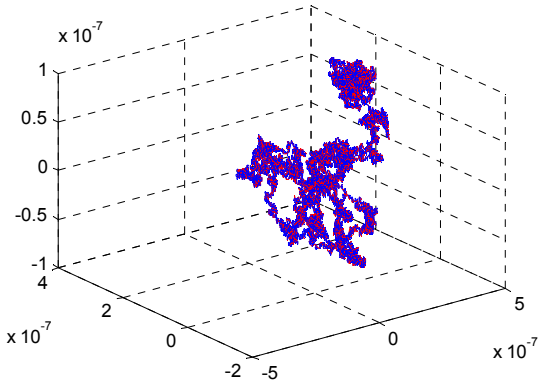

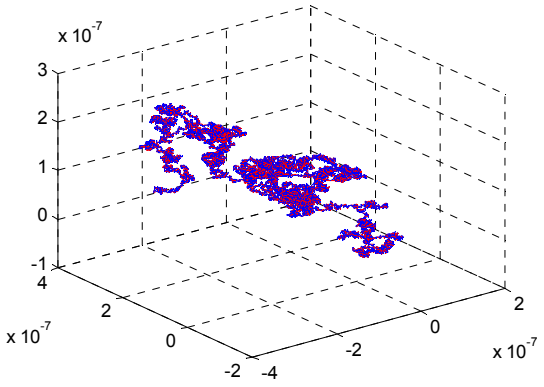

A.3 FORMULA EAS-155-93 SOFT STATE CONFORMATIONS

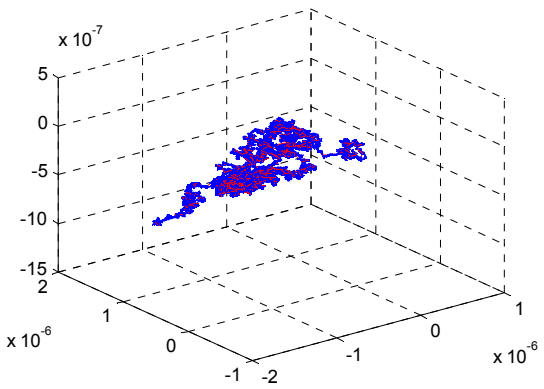

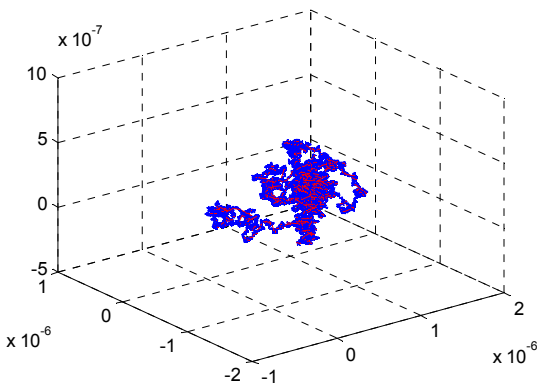

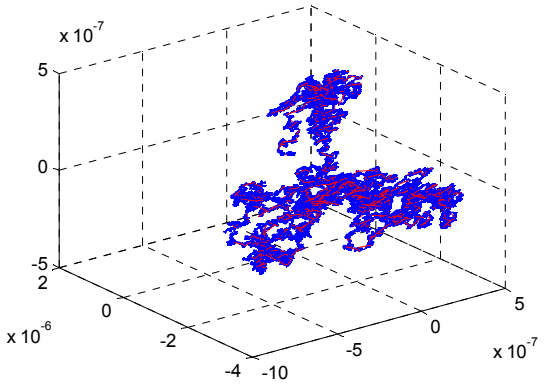

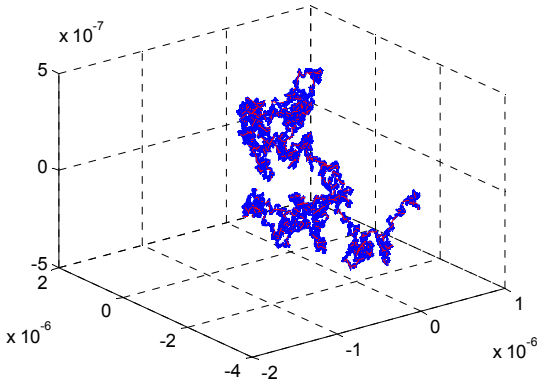

A.4 FORMULA EAS-155-93 HARD STATE CONFORMATIONS

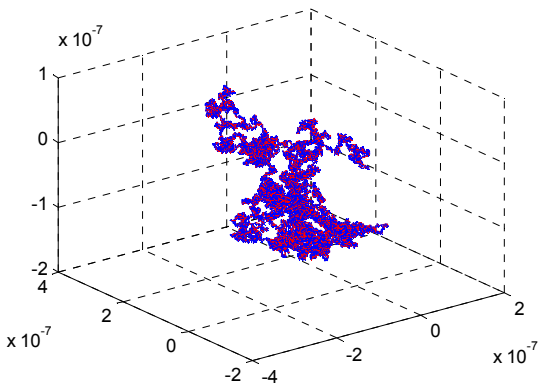

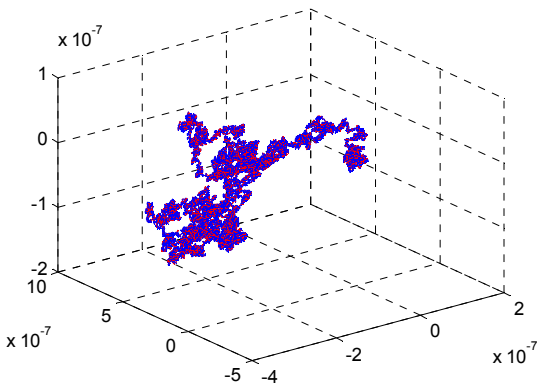

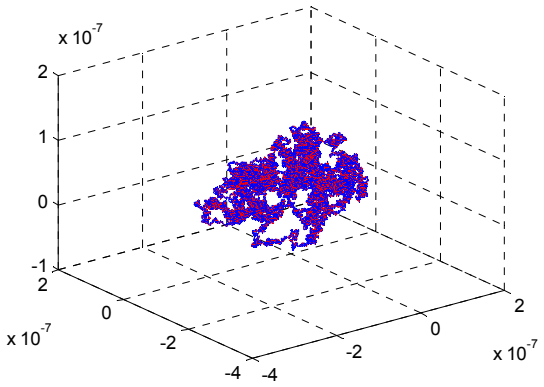

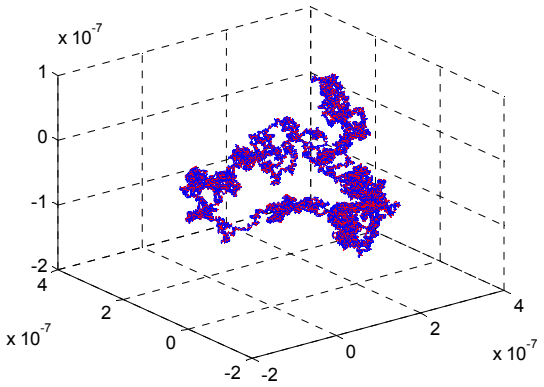

A.5 FORMULA EAS-155-143 SOFT STATE CONFORMATIONS

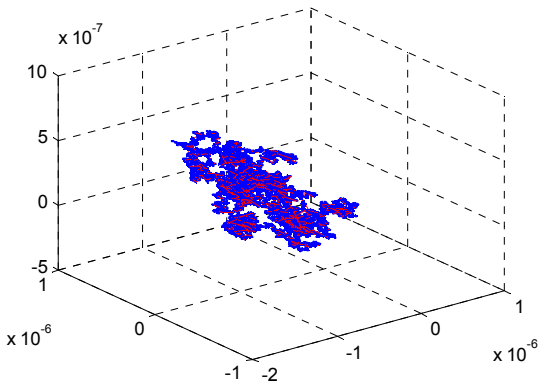

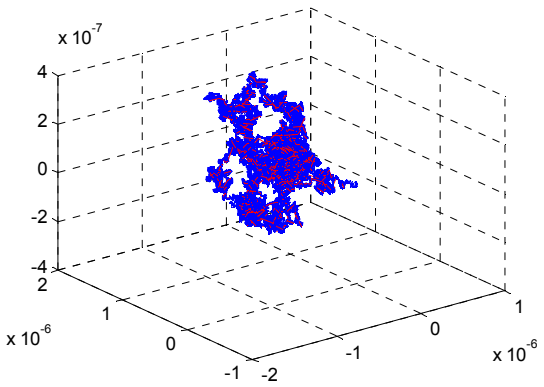

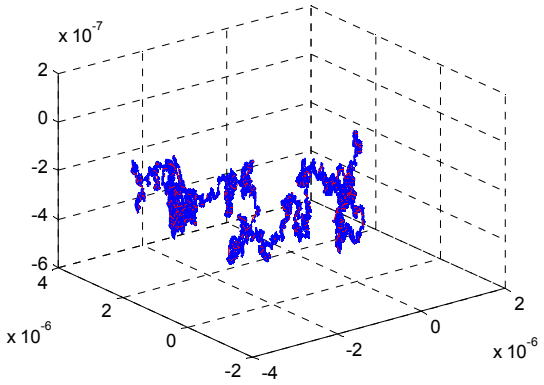

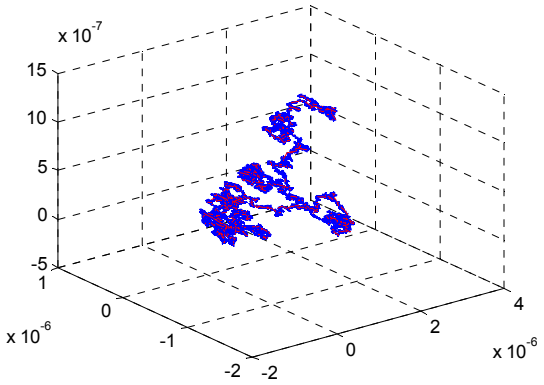

A.6 FORMULA EAS-155-143 HARD STATE CONFORMATIONS

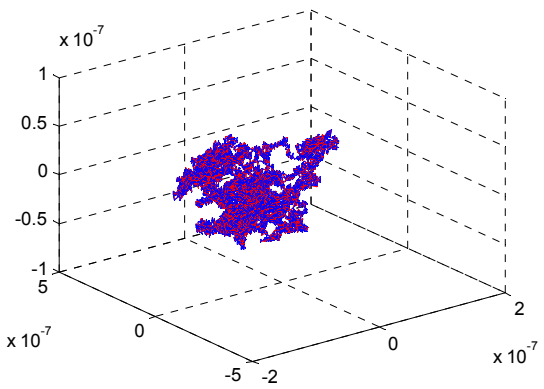

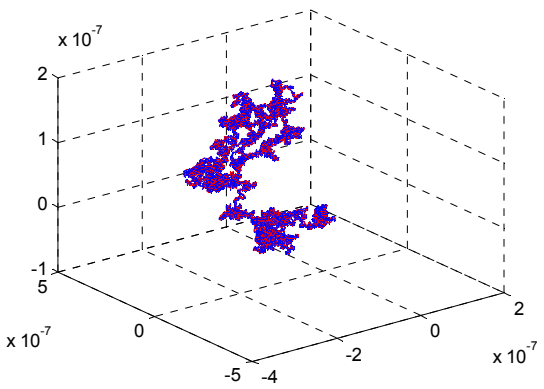

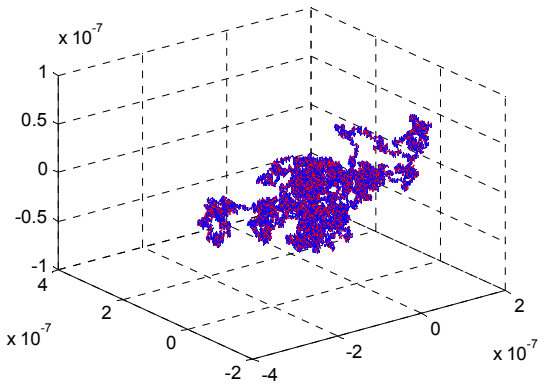

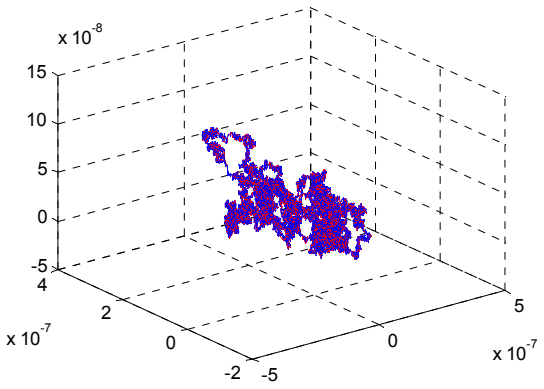

APPENDIX B

FORMULA EAS-155-143

B.1 FORMULA EAS-155-143 EQUI-BIAXIAL TEST RESULTS

Pictured below in Figures B.1-1 through B.1-3 are the stress predictions for formula EAS-155-143 under equi-biaxial strain. As previously, hard state predictions are shown using calculated junction constraint correction factors using both formula 93 and 115.

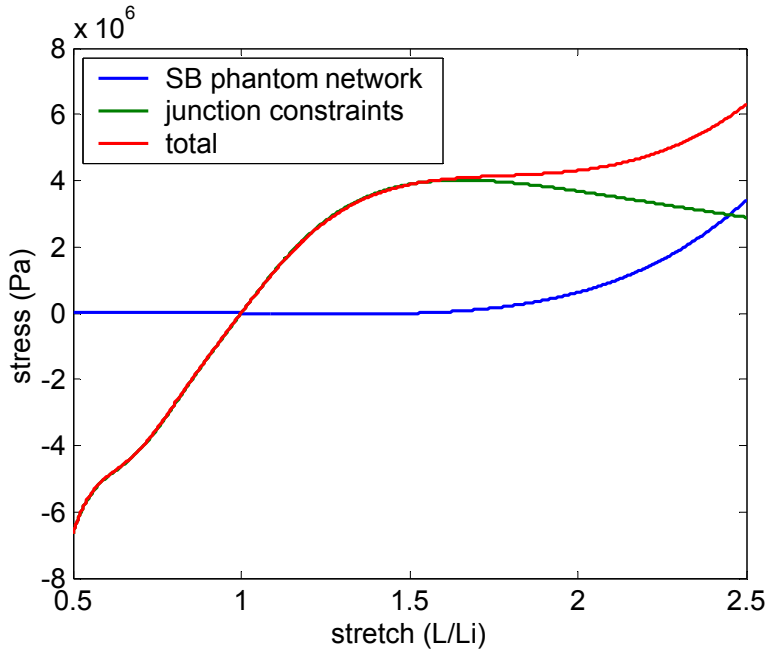

Figure B.1-1: Predicted stress contributions under equi-biaxial strain for formula EAS-155-143 in the soft state

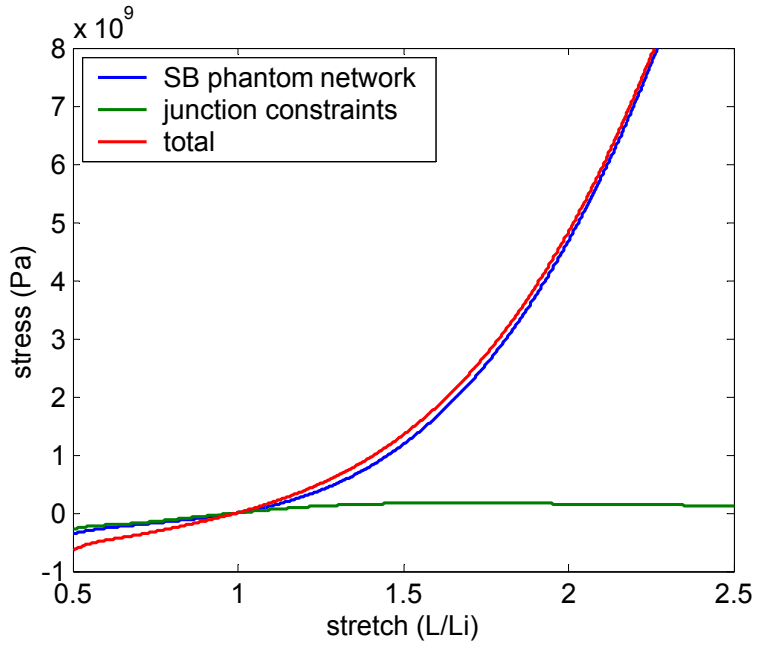

Figure B.1-2: Predicted stress contributions under equi-biaxial strain for formula EAS-155-143 in the hard state using formula 93 ratio

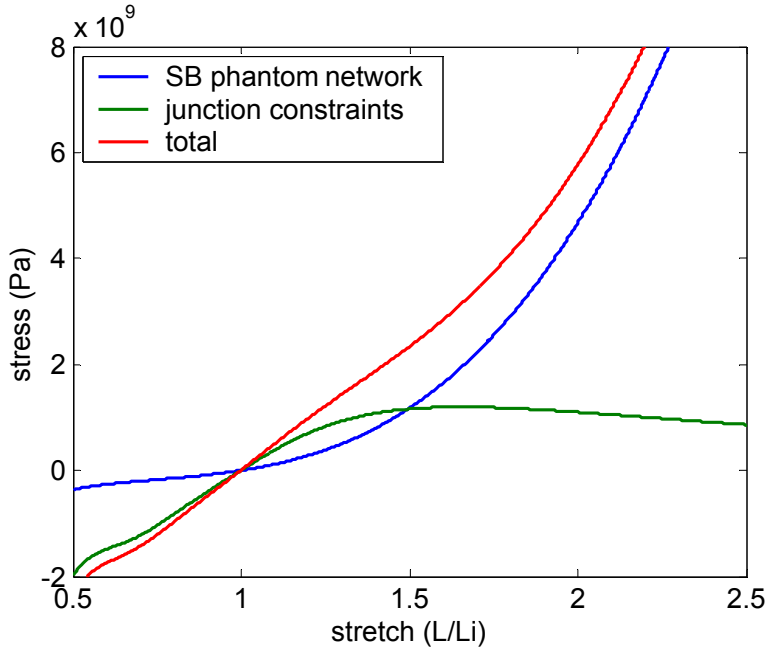

Figure B.1-3: Predicted stress contributions under equi-biaxial strain for formula EAS-155-143 in the hard state using formula 115 ratio

Table B.1-1: Junction constraint theory predicted hard and soft state properties of formula EAS-155-143 under equi-biaxial strain

	Biaxial Modulus SB MPa	STDEV MPa
Soft State	4.4	0.0
Hard State 93-ratio	473	104
Hard State 115-ratio	1600	106

The soft state predicted biaxial modulus is lower than that of formulas 93 and 115, which is in agreement with the trends of the predicted Young's moduli of the three formulas. The hard state biaxial modulus predicted using the formula 93 ratio is lower than the hard state biaxial modulus predicted for formula 93 but higher than that predicted for formula 115. The hard state biaxial modulus predicted using the formula 115 ratio is also higher than the predicted biaxial modulus for formula 115 and lower than that predicted for formula 93. This change in order based on the magnitude of the biaxial modulus with respect to the order based on the predicted Young's moduli for the formula again leads to the conclusion that the junction constraint theory is ill-suited for predictive purposes.

B.2 FORMULA EAS-155-143 SHEAR TEST RESULTS

Pictured below in Figures B.2-1 through B.2-3 are the stress predictions for formula EAS-155-143 under shear. Table B.2-1 lists the predicted shear moduli in the hard and soft states using the Johnson bounded distribution.

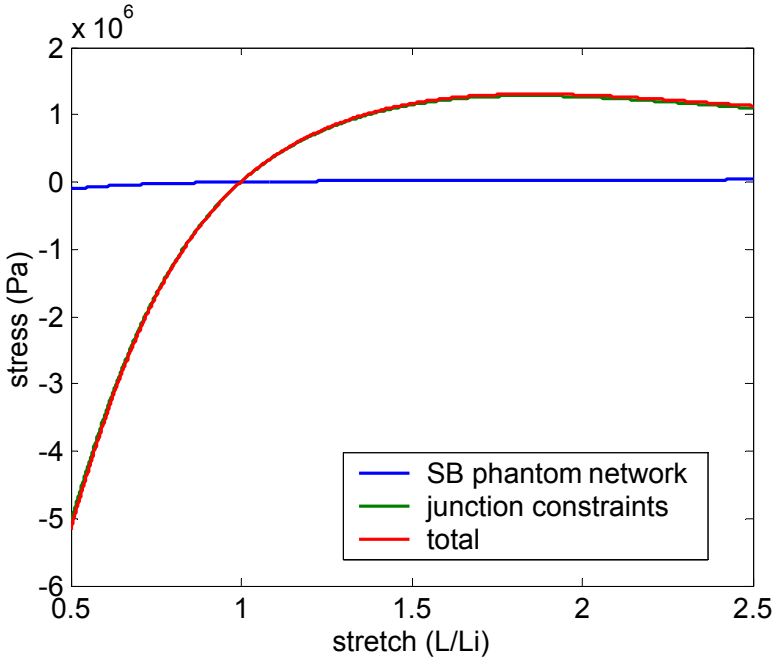

Figure B.2-1: Predicted stress contributions under shear strain for formula EAS-155-143 in the soft state

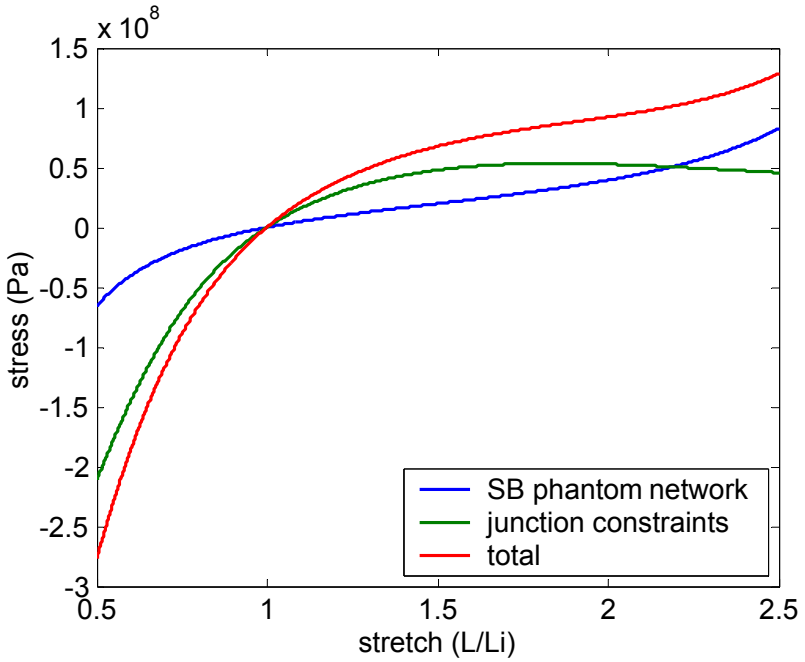

Figure B.2-2: Predicted stress contributions under shear strain for formula EAS-155-143 in the hard state using formula 93 ratio

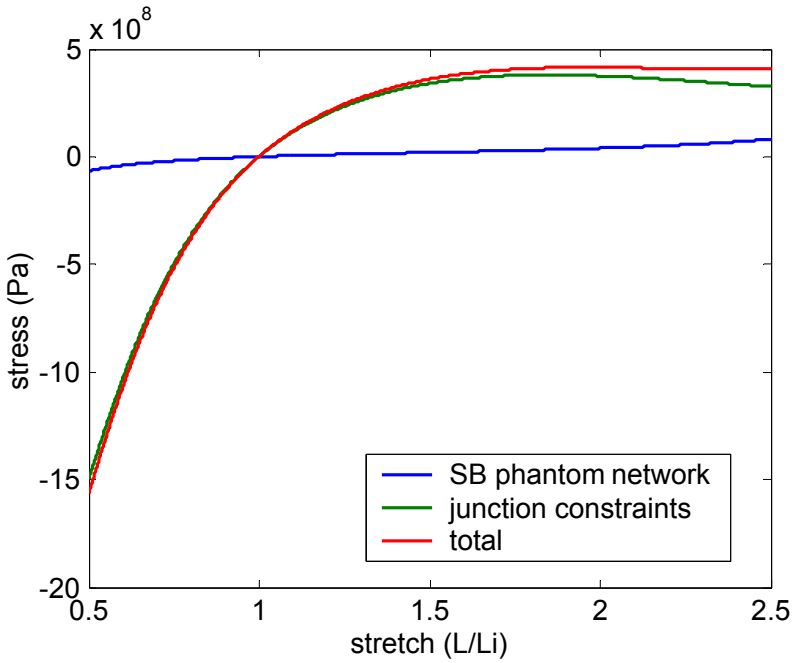

Figure B.2-3: Predicted stress contributions under shear strain for formula EAS-155-143 in the hard state using formula 115 ratio

Table B.2-1: Junction constraint theory predicted hard and soft state properties of formula EAS-155-143 under shear

	Shear Modulus SB MPa	STDEV MPa
Soft State	0.7	0.0
Hard State 93-ratio	47	7.0
Hard State 115-ratio	218	7.1

As expected, the soft state shear modulus is lower than both the predicted values for formula 93 and 115. The hard state shear modulus predicted using the formula 93 ratio is also lower than that predicted for formulas 93 and 115, however, the hard state shear modulus predicted using the formula 115 ratio is higher than the predicted shear modulus of formula 115. This again reaffirms that the three modeled formulas are not sufficiently similar enough to allow a

universally applied junction constraint correction factor. Table B.2-2 below lists all of the phantom network and junction constraint predicted tensile, biaxial, and shear moduli in the hard and soft states.

Table B.2-2: Junction constraint model Young's, biaxial, and shear modulus predictions

		Phantom Network		Junction Constraint Theory	
Strain State	Formula	Soft State	Hard State	Soft State	Hard State
Tensile	115 (MPa)	0.06	49	2.0	110
	93 (MPa)	0.08	65	5.0	850
	143 93 (MPa)	0.06	232	1.1	124
	143 115 (MPa)				318
Equi-biaxial	115 (MPa)	NA	NA	7.9	422
	93 (MPa)	NA	NA	19.8	3384
	143 93 (MPa)	NA	NA	4.4	473
	143 115 (MPa)	NA	NA		1603
Shear	115 (MPa)	NA	NA	1.2	52
	93 (MPa)	NA	NA	3.0	509
	143 93 (MPa)	NA	NA	0.7	47
	143 115 (MPa)	NA	NA		218

BIBLIOGRAPHY

[1] Z G Wei, R Sandstrom, S Miyazaki, *Review Shape-memory materials and hybrid composites for smart systems*, Journal of Materials Science, vol. 33, pp 3743-3762, 1998

[2] I. J. Rao, K. R. Rajagopal, *A study of strain-induced crystallization of polymers*, International Journal of Solids and Structures, vol. 38, pp 1149-167, 2001

[3] C. Poilane, P. Delobelle, C. Lexcellent, S. Hayashi, H. Tobushi, *Analysis of the mechanical behavior of shape memory polymer membranes by nanoindentation, bulging and point membrane deflection tests*, Thin Solid Films, vol. 379, pp 156-165, 2000

[4] M. Bonner, L. S. Saunders, I. M. Ward, G. W. Davies, M. Wang, K. E. Tanner, W. Bonfield, *Anisotropic mechanical properties of oriented HAPEX^{TM}*, Journal of Materials Science, vol. 37, pp 325-334, 2002

[5] Andreas Lendlein, Robert Langer, *Biodegradable, Elastic Shape-Memory Polymers for Potential Biomedical Applications*, Science, vol. 296, pp 1673-1676, 31 May 2002

[6] Changdeng Liu, Seung B. Chun, Patrick T. Mather, Lei Zheng, Elisabeth H. Haley, E. Bryan Coughlin, *Chemically Cross-Linked Polycyclooctene: Synthesis, Characterization, and Shape Memory Behavior*, Macromolecules, vol. 35, pp 9868-9874, 2002

[7] Rebecca B. Dupaix, Mary C. Boyce, *Constitutive modeling of the finite strain behavior of amorphous polymers in and above the glass transition*, Mechanics of Materials, vol. 39, pp 39-52, 2007

[8] D. A. Chernous, S. V. Shil'ko, Yu. M. Pleskachevskii, *Description of the Shape Memory Effect of Radiation-Modified Polymers Under Thermomechanical Action*, Journal of Engineering Physics and Thermophysics, vol. 77, no. 1, pp 6-10, 2004

[9] Ellen M. Arruda, Mary C. Boyce, Harald Quintus-Bosz, *Effects of Initial Anisotropy on the Finite Strain Deformation Behavior of Glassy Polymers*, International Journal of Plasticity, vol. 9, pp 783-811, 1993

[10] B. Yang, W. M. Huang, C. Li, L. Li, *Effects of moisture of the thermomechanical properties of a polyurethane shape memory polymer*, Polymer, vol. 47, pp 1348-1356, 2006

[11] Korey Gorss, Lisa Weiland, *Flexure Testing of Shape Memory Polymers for Morphing Aircraft Applications*, Proceedings of IMECE 2007, 11-15 Nov 2007, Seattle Washington, USA

[12] Kan Gall, Marin L. Dunn, Yiping Liu, Goran Stefanic, Davor Balzar, *Internal stress storage in shape memory polymer nanocomposites*, Applied Physics Letters, vol. 85, no. 2, pp 290-292, 12 July 2004

[13] C. Liang, C. A. Rogers, E. Malafeew, *Investigation of Shape Memory Polymers and Their Hybrid Composites*, Journal of Intelligent Material Systems and Structures, vol. 8, pp 380-386, April 1997

[14] Takeru Ohki, Qing-Qing Ni, Norihito Ohsako, Masaharu Iwamoto, *Mechanical and shape memory behavior of composites with shape memory polymer*, Composites: Part A: Applied Science and Manufacturing, vol. 35, pp 1065-1073, 2004

[15] Hisaaki Tobushi, Ryosuke Matsui, Tsuyoshi Takada, Shunichi Hayashi, *Shape Fixity and Shape Recovery of Shape Memory Polymer and Their Applications*, XXI ICTAM, 15-21 August 2004, Warsaw, Poland

[16] Andreas Lendlein, Steffen Kelch, *Shape-Memory Polymers*, Angewandte Chemie International Edition, vol. 41, pp 2034-2057, 2002

[17] Z. G. Wei, R. Sanstrom, S. Miyazaki, *Shape-memory materials and hybrid composites for smart systems, Part I Shape-memory materials*, Journal of Materials Science, vol. 33, pp 3743-3762, 1998

[18] Z. G. Wei, R. Sandstrom, S. Miyazaki, *Shape memory materials and hybrid composites for smart systems, Part II Shape-memory hybrid composites*, Journal of Materials Science, vol. 33, pp 3763-3783, 1998

[19] A. Lendlein, S. Kelch, K. Kratz, J. Schulte, *Shape Memory Polymers*, Encyclopedia of Materials: Science and Technology, ISBN 0-08-043152-6, pp 1-9, ©2005 Elsevior Ltd.

[20] Sung Ho Lee, Jin Woo Kim Byung Kyu Kim, *Shape memory polyurethanes having crosslinks in soft and hard segments*, Smart Materials and Structures, vol. 13, pp 1345-1350, 2004

[21] Sakae Aida, Shinichi Saduai, Shunji Nomura, *Strain-induced ordering of microdomain structures in polystyrene-block-polybutadiene-block-polystyrene triblock copolymers cross-linked in the disorded state*, Polymer, vol. 43, pp 2881-2887, 2002

[22] Bo Sun Lee, Byoung Chul Chun, Yong-Chain Chung, Kyung Il Sul, Jae Whan Cho, *Structure and Thermomechanical Properties of Polyurethane Block Copolymers with Shape Memory Effect*, Macromolecules, vol. 34, pp 6431-6437, 2001

[23] H. Tobushi, R. Matsui, S. Hayashi, D. Shimada, *The influence of shape-holding conditions on shape recovery of polyurethane-shape memory polymer foams*, Smart Materials and Structures, vol. 13, pp 881-887, 2004

[24] Yiping Liu, *Thermomechanical Behavior of Shape Memory Polymers*, University of Colorado, Department of Mechanical Engineering, ©2004

[25] Hisaaki Tobushi, Hisashi Hara, Etsuko Yamada, Shunichi Hayashi, *Thermomechanical properties in a thin film of shape memory polymer of polyurethane series*, Smart Materials and Structures, vol. 5, pp 483-491, 1996

[26] Ken Gall, Christopher M. Yakacki, Yiping Liu, Robin Shandas, Nick Willett, Kristi S. Anseth, *Thermomechanics of the shape memory effect in polymers for biomedical applications*, Wiley InterScience, pp 339-348, 1 April 2005

[27] Takenobu Sakai, Takayuki Tao, Satoshi Somiya, *Viscoelasticity of Shape Memory Polymer: Polyurethane series DiARY®*, Journal of Solid Mechanics and Materials Engineering, vol. 1, no. 4, pp 480-489, 2007

[28] Yoseph Bar-Cohen, *Electro-active polymers: current capabilities and challenges*, Proceedings of SPIE NDE and Smart Structures Conference, #4695-02-05, 17-19 March 2002, San Diego, CA

[29] Jason W. Paquette, Kwang J. Kim, *Ionomeric Electroactive Polymer Artificial Muscle for Naval Applications*, IEEE Journal of Oceanic Engineering, vol. 29, no. 3, pp 729-737, July 2004

[30] Y. Bar-Cohen, T. Xue, M. Shahinpoor, J. O. Simpson, J. Smith, *Low-mass muscle actuators using electroactive polymers (EAP)*, Proceedings of SPIE's 5th Annual International Symposium on Smart Structures and Materials, no. 3324-32, 1-5 March 1998, San Diego, CA

[31] Jessica L. Matthews, Emily K. Lada, Lisa M. Weiland, Ralph C. Smith, Donald J. Leo, *Monte Carlo simulation of a solvated ionic polymer with cluster morphology*, Smart Materials and Structures, vol. 15, pp 187-199, 2006

[32] H. Finkelmann, E. Nishikawa, G. G. Pereira, M. Warner, *A New Opto-Mechanical Effect in Solids*, Physical Review Letters, vol. 87, no. 1, pp 1-4, 2 July 2001

[33] Tomiki Ikeda, Makoto Nakano, Yanlei Yu, Osamu Tsutsumi, Akihiko Kanazawa, *Anisotropic Bending and Unbending Behavior of Azobenzene Liquid-Crystalline Gels by Light Exposure*, Advanced Materials, vol. 15, no. 3, pp 201-205, February 2003

[34] L. M. Racz, L. Li, B. Abedian, *Cure Kinetics of Light Activated Polymers*, Journal of Polymer Science: Part B: Polymer Physics, vol. 36, pp 2887-2894, 1998

[35] Yanlei Yu, Makoto Nakano, Tomiki Ikeda, *Direct bending of a polymer film by light*, Nature, vol. 425, pp 145, 11 September 2003

[36] Tat Tong, Emily Snyder, *Light Activated Shape Memory Co-Polymers*, World Intellectual Property Organization, WO/2007/001407, 1 April 2007

[37] Andreas Lendlein, Hongyan Jiang, Oliver Junger, Robert Langer, *Light-induced shape-memory polymers*, Nature, vol. 434, pp 879-882, 14 April 2005

[38] Min-Hui Li, Patrick Keller, Bin Li, Xiaogong Want, Monique Brunet, *Light-Driven Side-On Nematic Elastomer Actuators*, Advanced Materials, vol. 15, no. 7-8, pp 569-572, 17 April 2003

[39] Atsushi Suzuki, Toyoichi Tanaka, *Phase transition in polymer gels induced by visible light*, Nature, vol. 346, pp 345-347, 26 July 1990

[40] Taichi Ichihashi, Wasaburo Kawai, Tadashi Naraoka, Takateru Asanu, *Photosensitive high polymer, easily insolubilized when cross-linked by light, a method for preparation therof, and a composition thereof*, United States Patent, #4560640, 11 June 1984

[41] John K. Borchardt, *Shape-memory polymers see the light*, MaterialsToday, vol. 8, no. 6, June 2005

[42] Emily Snyder, Tat H. Tong, *Towards Novel Light-Activated Shape Memory Polymer: Thermomechanical Properties of Photo-responsive Polymers*, Materials Research Society Symposium Proceedings, vol. 872, pp J18.6.1-6, 2005

[43] S. B. Lin, K. S. Hwang, S. Y. Tsay, S. L. Cooper, *Segmental orientation studies of polyether polyurethane block copolymers with different segment lengths and distributions*, Colloid and Polymer Science, vol. 263, pp 128-140, 1985

[44] Yoseph Bar-Cohen, *Electroactive Polymers as Artificial Muscles – Capabilities, Potentials, and Challenges*, Handbook on Biomemetics, section 11, chapter 8, paper #134, publisher: NTS Inc., 2000

[45] Yoseph Bar-Cohen, *Electroactive Polymers as Artificial Muscles – Reality and Challenges*, American Institute of Aeronautics and Astronautics, paper #2001-1492, 2001

[46] V. A. Beloshenko, Ya. E. Beygelzimer, A. P. Borzenko, V. N. Varyukhin, *Shape memory effect in the epoxy polymer – thermoexpanded graphite system*, Composites Part A: Applied Science and Manufacturing, vol. 33, issue 7, 1 July 2002, pp 1001-1006

[47] Marc Behl, Andreas Lendlein, *Actively moving polymers*, The Royal Society of Chemistry - Soft Matter, vol. 3, pp 58-67, 2007

[48] Jinqiang Jiang, Bo Qi, Martin Lepage, Yue Zhao, *Polymer Micelles Stabilization on Demand through Reversible Photo-Cross-Linking*, Macromolecules, vol. 40, pp 790-792, 2007

[49] O. Hausler, D. Schick, Ch. Tsakmakis, *Description of plastic anisotropy effects at large deformations. Part II: the case of transverse isotropy*, International Journal of Plasticity, vol. 20, pp 199-223, 2004

[50] Hisaaki Tobushi, Kayo Okumura, Shunichi Hayashi, Norimitsu Ito, *Thermomechanical constitutive model of shape memory polymer*, Mechanics of Materials, vol. 33, pp 545-554, 2001

[51] Julie Diani, Yiping Liu, Ken Gall, *Finite Strain 3D Thermoviscoelastic Constitutive Model for Shape Memory Polymers*, Polymer Engineering and Science, pp 486-492, 2006

[52] Richard Beblo, Lisa Mauck Weiland, *Polymer Chain Alignment in Shape Memory Polymer*, ASME-IMECE 2006, #13703, 5-10 November 2006, Chicago, Illinois

[53] G. Barot, I. J. Rao, *Constitutive modeling of the mechanics associated with crystallizable shape memory polymers*, Zietschrift fur angewandte Mathematik und Physik ZAMP, vol. 57, pp 652-681, 2006

[54] Korey Gross, *Mechanical Characterization of Shape Memory Polymers to Assess Candidacy as Morphing Aircraft Skin*, University of Pittsburgh, MS Thesis, 2008

[55] Richard Beblo, Lisa Mauck Weiland, *Strain induced anisotropic properties of shape memory polymer*, Smart Materials and Structures, vol. 17, September 2008

[56] Gyaneshwar Tandon, Kenneth Goecke, Kristin Cable, Jeff Baur, *Durability Assessment of Styrene- and Epoxy-based Shape Memory Polymer Resins*, Journal of Intelligent Material Systems and Structures, 2009, under review

[57] Tiping Liu, Ken Gall, Martin L. Dunn, Patrick McCluskey, *Thermomechanics of shape memory polymer nanocomposites*, Mechanics of Materials, vol. 36, pp 929-940, 2004

[58] H. Tobushi, D. Shimada, S. Hayashi, M. Endo, *Shape fixity and shape recovery of polyurethane shape-memory polymer foams*, Proceedings Institution of Mechanical Engineers Part L: Journal of Materials: Design and Applications, vol. 217, pp 135-143, 2003

[59] W. M. Huang, B. Yang, L. An, C. Li, Y. S. Chan, *Water-driven programmable polyurethane shape memory polymer: Demonstration and mechanism*, Applied Physics Letters, vol. 86, no. 114105, 2005

[60] B. Yang, W. M. Huang, C. Li, C. M. Lee, L. Li, *On the effects of moisture in a polyurethane shape memory polymer*, Smart Materials and Structures, vol. 13, pp 191-195, 2004

[61] Jae Whan Cho, Jeong Won Kim, Yong Chae Jung, Nam Seo Goo, *Electroactive Shape-Memory Polyurethane Composites Incorporating Carbon Nanotubes*, Macromolecular Rapid Communications, vol. 26, pp 412-416, 2005

[62] Annette M. Schmidt, *Electomagnetic Activation of Shape Memory Polymer Networks Containing Magnetic Nanoparticles*, Macromolecular Rapid Communications, vol. 27, pp 1168-1172, 2006

[63] Patrick R. Buckley, Gareth H. McKinley, Thomas S. Wilson, Ward Small IV, William J. Benett, Jane P. Bearinger, Michael W. McElfresh, Duncan J. Maitland, *Inductively Heated Shape Memory Polymer for the Magnetic Actuation of Medical Devices*, IEEE Transactions on Biomedical Engineering, vol. 53, no. 10, pp 2075-2083, October 2006

[64] Shunichi Hayashi, Yoshiyuki Tasaka, Noriya Hayashi, Yasuhiro Akita, *Development of Smart Polymer Materials and its Various Applications*, Technical Review, vol. 41, no. 1, February 2004

[65] Yousefi-Koma, D. G. Zimcik, *Applications of Smart Structures to Aircraft for Performance Enhancement*, Canadian Aeronautics and Space Journal, vol. 49, no. 4, pp 163-172, 2003

[66] J. N. Kudva, *Overview of the DARPA Smart Wing Project*, Journal of Intelligent Materials Systems and Structures, vol. 15, pp 261-267, 2004

[67] H. M. Wache, D. J. Tartakowska, A. Hentrich, M. H. Wagner, *Development of a polymer stent with shape memory effect as a drug delivery system*, Journal of Materials Science: Materials in Medicine, vol. 14, pp 109-112, 2003

[68] Ward Small IV, Thomas S. Wilson, William J. Benett, Jeffery M. Loge, Duncan J. Maitland, *Laser-activated shape memory polymer intravascular thrombectomy device*, Optics Express, vol. 13, no. 20, pp 8204-8213, 3 October 2005

[69] Ward Small IV, Patrick R. Buckley, Thomas S. Wilson, William J. Benett, Jonathan Hartman, David Saloner, Duncan J. Maitland, *Shape Memory Polymer Stent With Expandable Foam: A New Concept for Endovascular Embolization of Fusiform Aneurysms*, IEEE Transactions of Biomedical Engineering, vol. 54, no. 6, pp 1157-1160, June 2007

[70] Marc Behl, Andreas Lendlein, *Shape-memory Polymers*, Materials Today, vol. 10, no. 4, pp 20-28, April 2007

[71] Ward Small IV, Melodie F. Metzger, Thomas S. Wilson, Duncan J. Maitland, *Laser-Activated Shape Memory Polymer Microactuator forThrombus Removal Following Ischemic Stroke: Preliminary In Vitro Analysis*, IEEE Journal of Selected Topics in Quantum Electronics, vol. 11, no. 4, pp 892-901, July/August 2005

[72] D. Babic, D. M. Souverain, V. T. Stannett, D. R. Squire, G. L. Hagnauer, R. E. Singler, *The Radiation Crosslinking and Scission of Some Polyphosphanes*, Int. J. Radiat. Appl. Instrum., Part C, vol. 28, no. 2, pp 169-172, 1986

[73] D. Babic, V. T. Stannett, *Theoretical Considerations of Scission and Endlinking Reactions in Irradiated Polymers*, Int. J. Radiat. Appl. Instrum. Part C, vol. 30, no. 3, pp 183-187, 1987

[74] Akira Mamada, Toyoichi Tanaka, Dawan Kungwatchakun, Masahiro Irie, *Photoinduced Phase Transitions of Gels*, Macromolecules, vol. 23, pp 1517-1519, 1990

[75] Hongyan Jiang, Steffen Kelch, Andreas Lendlein, *Polymers Move in Response to Light*, Advanced Materials, vol. 18, pp 1471-1475, 2006

[76] A L Andrady, S H Hamid, X Hu, A Torikai, *Effects of increased solar ultraviolet radiation on materials*, Journal of Photochemistry and Photobiology B: Biology, vol. 46, pp 96-103, 1998

[77] P Alexander, R M Black, A Charlesby, *Radiation Induced Changes in the Structure of Polyisobutylene*, Proceedings of the Royal Society of London. Series A, Mathematical and Physical Sciences, vol. 232, no. 1188, pp 31-48, 11 October 1955

[78] T Seguchi, K Arakawa, N Hayadawa, S Machi, *Radiation Induced Oxidative Degradation of Polymers – IV Dose Rate Effects on Chemical and Mechanical Properties*, Radiat Phys Chem, vol. 18, no. 3-4, pp 671-678, 1981

[79] H Wilski, *The Radiation Induced Degradation of Polymers*, Radiat Phys Chem, vol. 29, no. 1, pp 1-14, 1987

[80] Hartmut Figger, Dieter Meschede, Claus Zimmermann, Laser Physics at the Limits, Springer-Verlag, Berlin Germany, ©2002

[81] S. A. Akhmanov, S. Yu. Nikitin, Physical Optics, Oxford University Press Inc., New York, pp 93-100, ©1997

[82] G. Pannetier, P. Souchay, Chemical Kinetics, Elsevier Publishing Co. LTD, pp 133-137, ©1967

[83] P. J. Flory, *Foundations of Rotational Isomeric State Theory and General Methods for Generating Configurational Averages*, Macromolecules, vol. 7, no. 3, pp 381-392, May-June 1947

[84] Paul J. Flory, *Molecular Size Distribution in Three Dimensional Polymers. III. Tetrafunctional Branching Units*, Journal of the American Chemical Society, vol. 63, no. 11, pp 3096-3100, Nov 1941

[85] Paul J. Flory, *Molecular Theory of Rubber Elasticity*, Polymer Journal, vol. 17, no. 1, pp 1-12, 1985

[86] D. Y. Yoon, P. J. Flory, *Moments and distribution functions for polymer chains of finite length. II. Polymethylene chains*, The Journal of Chemical Physics, vol. 16, no. 12, pp 5366-5380, Dec 1974

[87] Paul J. Flory, *Spatial Configurations of Macromolecular Chains*, Nobel Lecture, pp 156-177, 11 Dec 1974

[88] Burak Erman, Paul J. Flory, *Relationships between Stress, Strain, and Molecular Constitution of Polymer Networks. Comparison of Theory with Experiments*, Macromolecules, vol. 15, pp 806-811, 1982

[89] Y. Abe, P. J. Flory, *Rotational Isomerization of Polymer Chains by Stretching*, The Journal of Chemical Physics, vol. 52, no. 6, pp 2814-2820, 15 March 1970

[90] Thomas G. Fox Jr., Paul J. Flory, *Second-Order Transition Temperatures and Related Properties of Polystyrene. I. Influence of Molecular Weight*, Journal of Applied Physics, vol. 21, pp 581-591, June 1950

[91] Paul J. Flory, John Rehner Jr., *Statistical Mechanics of Cross-Linked Polymer Networks*, The Journal of Chemical Physics, vol. 11, no. 11, pp 512-520, 4 October 1943

[92] P. J. Flory, *Statistical thermodynamics of random networks*, Proceedings of the Royal Society of London, Series A, Mathematical and Physics Sciences, pp 351-380, 1976

[93] Frederick T. Wall, Paul J. Flory, *Statistical Thermodynamics of Rubber Elasticity*, The Journal of Chemical Physics, vol. 19, no. 12, pp 1435-1439, Dec 1951

[94] Paul J. Flory, *The Configuration of Real Polymer Chains*, The Journal of Chemical Physics, vol. 17, no. 3, pp 303-310, March 1949

[95] Paul J. Flory, *The Elastic Free Energy of Dilation of a Network*, Macromolecules, vol. 12, no. 1, pp 119-122, 1979

[96] Paul. J. Flory, *Theory of Crystallization in Copolymers*, Transactions of the Faraday Society, vol. 51, pp 848-857, 1955

[97] Burak Erman, Paul J. Flory, *Theory of elasticity of polymer networks. II. The effect of geometric constraints on junctions*, The Journal of Chemical Physics, vol. 68, no. 12, pp 5363-5369, 15 June 1978

[98] Paul J. Flory, Burak Erman, *Theory of Elasticity of Polymer Networks. 3*, Macromolecules, vol. 15, no. 3, pp 800-806, June 1982

[99] P. J. Flory, *Theory of elasticity of polymer networks. The effect of local constraints on junctions*, The Journal of Chemical Physics, vol. 66, no. 12, pp 5720-5729, 15 June 1977

[100] P. J. Flory, *Thermodynamic Relations For High Elastic Materials*, Transactions of the Faraday Society, vol. 57, pp 829-838, 1961

[101] J. E. Mark, J. G. Curro, *A non-Gaussian theory of rubberlike elasticity based on rotational isomeric state simulations of network chain configurations. I. Polyethylene and polydimethylsiloxane short-chain unimodal networks*, Journal of Chemical Physics, vol. 79, no. 11, pp 5705-5709, 1 December 1983

[102] Lisa Mauck Weiland, Emily K. Lada, Ralph C. Smith, Donald J. Leo, *Application of Rotational Isomeric State Theory to Ionic Polymer Stiffness Predictions*, Statistical and Applied Mathematical Sciences Institute, technical report #2005-3, 22 February 2005

[103] Fei Gao, Lisa Mauck Weiland, *Improving rotational isomeric state theory for application to mechanical properties prediction*, Proceedings of SPIE, vol. 6526, 19 March 2007, San Diego, CA, USA

[104] Fei Gao, Lisa M. Weiland, *A multiscale model applied to ionic polymer stiffness prediction*, Journal of Materials Research, vol. 23, no. 3, pp 833-841, March 2008

[105] L. R. G. Treloar, H. G. Hopkins, R. S. Rivlin, J. M. Ball, *The Mechanics of Rubber Elasticity*, Proceedings of the Royal Society of London. Series A, Mathematical and Physical Sciences, vol. 351, no. 1666, pp 301-330, 19 November 1976

[106] Paul J. Flory, Statistical Mechanics of Chain Molecules, Interscience Publishers, Wiley and Sons Inc., ©1969

[107] James J. Swain, Sekhar Venkatraman, James R. Wilson, *Least-squares estimation of distribution functions in johnson's translation system*, Journal of Statistical Computation and Simulation, vol. 29, pp 271-297, 1 June 1988

[108] David J. DeBrota, Robert S. Dittus, Stephen D. Roberts, James R. Wilson, James J. Swain, Sekhar Venkatraman, *Modeling Input Processes With Johnson Distributions*, Proceedings of the 1989 Winter Simulation Conference, pp 308-318, 1989

[109] James R. Wilson, *Software for Stochastic Simulation Input Modeling*, http://www.ise.ncsu.edu/jwilson/page3.html, updated 22 July 2005, accessed 28 Oct 2009

[110] L. R. G. Treloar, The Physics of Rubber Elasticity, Third Edition, Oxford Classic Texts in the Physical Sciences, Oxford University Press, ©1975

[111] M. A. F. Wagner, J. R. Wilson, *Using univariate Bezier distributions to model simulations input processes*, IEEE Transactions, vol. 28, pp 699-711

[112] A. Avramidis, J. R. Wilson, *A Flexible Method for Estimating Inverse Distribution Functions in Simulation Experiments*, Proceedings of the 1989 Winter Simulation Conference, pp. 428-436

[113] Frank J. Massey Jr., *The Kolmogorov-Smirnov Test for Goodness of Fit*, Journal of the American Statistical Association, vol. 46, no. 253, pp 68-78, 1951

[114] Ellen M. Arruda, Mary C. Boyce, *A Three-Dimensional Constitutive Model for the Large Stretch Behavior of Rubber Elastic Materials*, Journal of the Mechanics and Physics of Solids, vol. 41, no. 2, pp 389-412, 1993

[115] S. J. Plimpton, R. Pollock, M. Stevens, *Particle-Mesh Ewald and rRESPA for Parallel Molecular Dynamics Simulations*, Proc. Of the Eighth SIAM Conference on Parallel Processing for Scientific Computing, Minneapolis, MN, March 1997

[116] LAMMPS website, http://lammps.sandia.gov/index.html, 6 June 2009

[117] A. Bhattacharyya, H. Tobushi, *Analysis of the Isothermal Mechanical Response of a Shape Memory Polymer Rheological Model*, Polymer Engineering and Science, vol. 40, no. 12, pp 2498-2510, 2000

[118] J. R. Lin, L. W. Chen, *Shape-Memorized Crosslinked Ester-Type Polyurethane and Its Mechanical Viscoelastic Model*, Journal of Applied Polymer Science, vol. 73, pp 1305-1319, 1999

[119] H. Tobushi, T. Hashimoto, S. Hayashi, E. Yamada, *Thermomechanical Constitutive Modeling in Shape Memory Polymer of Polyurethane Series*, Journal of Intelligent Material Systems and Structures, vol. 8, pp 711-718, August 1997

[120] Yiping Liu, Ken Gall, Martin L. Dunn, Alan R. Greenberg, Julie Diani, *Thermomechanics of shape memory polymers: Uniaxial experiments and constitutive modeling*, International Journal of Plasticity, vol. 22, pp 279-313, 2006

[121] M. A. Sharaf, J. E. Mark, *Monte Carlo simulations of filler-induced network chain deformations and elastomer reinforcement from oriented oblate particles*, Polymer, vol. 43, pp 643-652, 2002

[122] Mohammed A. Sharaf, James E. Mark, *Monte Carlo simulations on the effects of nanoparticles on chain deformations and reinforcement in amorphous polyethylene networks*, Polymer, vol. 45, pp 3943-3952, 2004

[123] Xiangjun Xing, Paul M. Goldbart, Leo Radzihovsky, *Thermal Fluctuations and Rubber Elasticity*, Physical Review Letters, vol. 98, 17 February 2007

[124] A. Elias-Zuniga, *A non-Gaussian network model for rubber elasticity*, Polymer, vol. 47, pp 907-914, 2006

[125] L. R. G. Treloar, G. Riding, *A Non-Gaussian Theory for Rubber in Biaxial Strain. I. Mechanical Properties*, Proceedings of the Royal Society of London. Series A, Mathematical and Physical Sciences, vol. 369, no. 1737, pp 261-280, 31 December 1979

[126] Ellen M. Arruda, Mary C. Boyce, *A Three-Dimensional Constitutive Model for the Large Stretch Behavior of Rubber Elastic Materials*, Journal of Mechanics and Physics of Solids, vol. 41, no. 2, pp 389-412, 1993

[127] Millard F. Beatty, *An Average-Stretch Full-Network Model for Rubber Elasticity*, Journal of Elasticity, vol. 70, pp 65-68, 2003

[128] P. D. Wu, E. Van Der Giessen, *On Improved Network Models for Rubber Elasticity and Their Applications to Orientation Hardening in Glassy Polymers*, Journal of Mehcanics and Physics of Solids, vol. 41, no. 3, pp 427-456, 1993

[129] G. R. Mitchell, F. J. Davis, W. Guo, *Strain-Induced Transitions in Liquid-Crystal Elastomers*, Physical Review Letters, vol. 71, no. 18, pp 2947-2950, 1 November 1993

[130] V. A. Beloshenko, V. N. Varyukhim, Yu V. Voznyak, *The shape memory effect in polymers*, Russian Chemical Reviews, vol. 73, no. 3, pp 265-283, 2005

[131] Michael Rubinstein, Sergei Panyukov, *Nonaffine Deformation and Elasticity of Polymer Networks*, Macromolecules, vol. 30, pp 8036-8044, 1997

[132] Bohumil Meissner, Libor Matejka, *A Lengevin-elasticity-theory-based constitutive equation for rubberlike networks and its comparison with biaxial stress-strain data. Part II.*, Polymer, vol. 45, pp 7247-7260, 2004

[133] Erhard Krempl, Christine M. Bordonaro, *A State Variable Model for High Strength Polymers*, Polymer Engineering and Science, vol. 35, no. 4, pp 310-316, February 1995

[134] Devdatt L. Kurdikar, Nikolaos A. Peppas, *A Kinetic Model for Diffusion-Controlled Bulk Cross-Linking Photopolymerizations*, Macromolecules, vol. 27, pp 4084-4092, 1994

[135] A. Charlesby, *Gel formation and molecular weight distribution in long-chain polymers*, Proceedings of the Royal Society of London. Series A, Mathematical and Physical Sciences, vol. 222, no. 1151, pp 542-557, 23 March 1954

[136] Claudia Sarmoria, Enrique Valles, *Model for a scission-crosslinking process with both H and Y crosslinks*, Polymer, vol. 45, pp 5661-5669, 2004

[137] A. Charlesby, *Molecular-Weight Changes in the Degradation of Long-Chain Polymers*, Proceedings of the Royal Society of London. Series A, Mathematical and Physical Sciences, vol. 224, no. 1156, pp 120-128, 9 June 1954

[138] Mandas Chanda, Advanced Polymer Chemistry, A Problem Solving Guide, Marcel Dekker Inc., ©2000

[139] Richard Beblo, Lisa Mauck Weiland, *Using Multiscale Modeling to Predict Material Response of Polymeric Materials*, SMASIS 2009, #1333, 20-24 September 2009, Oxnard, California

[140] Richard Beblo, Lisa Mauck Weiland, *Material Characterization and Multi-scale Modeling of Light Activated SMP*, SPIE-Smart Structures and Materials, 8-12 March 2009, San Diego, California

[141] Richard Beblo, Korey Gross, Lisa Mauck Weiland, *Experimentally Populated Model for Shape Memory Polymer*, under review by the Journal of Material Systems and Structures

[142] Richard Beblo, Lisa Mauck Weiland, *Light Activated Shape Memory Polymer Characterization*, Journal of Applied Mechanics, vol. 76, #11008, January 2009

[143] Richard Beblo, Lisa Mauck Weiland, *Multiscale Modeling of Light Activated Shape Memory Polymer*, SMASIS 2008, #345, 28-30 October 2008, Ellicott City, Maryland

[144] Richard Beblo, Lisa Mauck Weiland, Ernie Havens, Robert Schueler, Emily Snyder, Tat Tong, *Light Activated Shape Memory Polymer Characterization Challenges and Strategies*, SAMPE 2007, 29 October – 1 November 2007, Cincinnati, Ohio

[145] Akhtar S. Khan, Sujian Huang, Continuum Theory of Plasticity, John Wiley & Sons, Inc., ©1995

[146] P. J. Flory, Principles of Polymer Chemistry, Cornell University Press, Ithaca, NY, © 1953

[147] S. J. Plimpton, *Fast Parallel Algorithms for Short-Range Molecular Dynamics*, Journal of Computational Physics, vol. 117, 1-19, 1995

[148] Umesh Gaur, Suk-fai Lau, Brent B. Wunderlich, Bernard Wunderlich, *Heat Capacity and Other Thermodynamic Properties of Linear Macromolecules: VI Acrylic Polymers*, J. Phys. Chem. Ref. Data, vol. 11, no. 4, pp 1065-1089

[149] Doros N. Theodorou, Ulrich W. Suter, *Detailed Molecular Structure of a Vinyl Polymer Glass*, Macromolecules, vol. 18, 1985, pp 1467 – 1478

[150] Grant D. Smith, Do Y. Yoon, Richard L. Jaffe, *A Third-Order Rotational Isomeric State Model for Poly(oxyethylene) Based upon ab Initio Electronic Structure Analysis of Model Molecules*, Macromolecules, vol. 26, 1993, pp 5213 – 5218

[151] Ivet Bahar, Ignacio Zuniga, Robert Dodge, Wayne L. Mattice, *Configurational Statistics of Poly(dimethylsiloxane) 2: A New Rotational Isomeric State Approach*, Macromolecules, vol. 24, 1991, pp 2993 – 2998

NOTES

This material is based upon work supported by the Cornerstone Research Group, Inc. under contract no. W31P4Q-07-C-0282. Any opinions, findings and conclusions or recommendations expressed in this material are those of the author and do not necessarily reflect the views of the government.